MEMS-Based Purification and Sensing Technologies for Sustainable Water Management

A DISSERTATION
SUBMITTED TO THE FACULTY OF THE
UNIVERSITY OF MINNESOTA
BY

Peng Zhou

IN PARTIAL FULFILLMENT OF THE REQUIREMENTS
FOR THE DEGREE OF
DOCTOR OF PHILOSOPHY

Advisor: Tianhong Cui

June 2023

Acknowledgements

After five years of graduate study at the University of Minnesota, I would like to express my gratitude to the many people who have supported me during this journey.

First and foremost, I want to thank my advisor, Prof. Tianhong Cui, for his generous and continuous support, as well as his invaluable advice throughout my Ph.D. study. His unwavering support both academically and personally has helped me overcome the challenging times to reach this stage. Without his expertise and mentorship, I could not have completed this academic endeavor. I feel privileged to have him as my supervisor.

I would also like to express my special thanks to Prof. Terrence Simon for his continuous support over the past five years. His guidance, advice, and encouragement have been invaluable to me, and his erudition and elegance have been an inspiration to my learning.

I am deeply grateful to my colleagues from the Technology Integration & Advanced Nano/Microsystems Laboratory, including Dr. Jungyoon Kim, Dr. Tianyi Zhang, Dr. Qingyuan Liu, Dr. Guihua Xiao, Dr. Zongbo Zhang, Yingming Xu, and Jitong Duan. It has been an amazing experience working and spending cherished time together with them.

I would like to thank my friends, including Zichang Xiong, Yaling Liu, Yingying Zhang, Jing Gao, Dingbing Huang, Yuxin Wang, Zifan Kang, Ziwei Zhang, Shihao Liu, and many others, for always being there when I needed their support. Their help and encouragement have inspired me during difficult times and made the past five years much more enjoyable.

Finally, I want to express my deepest appreciation to my family members: my wife Fan Ge, my parents Qianwen Zhou and Cuiping Tao, my brother William Zhou, and my daughter who will be entering this world soon. Without their tremendous understanding and encouragement throughout my entire life, it would have been impossible for me to complete my study. Thank you for always being so supportive and helping me every step of the way.

Abstract

The management of water resources is a pressing global challenge. This research aims to address the issues of water pollution and scarcity by proposing micro-electromechanical systems (MEMS) based solutions for water purification and sensing. In particular, this research presents a new photoelectrocatalytic water purification system, an efficient valveless micropump, and a sensitive heavy metal ion sensor based on MEMS technologies, envisioning for a sensor-based closed-loop control water treatment platform.

The photocatalytic degradation of organic matter by titanium dioxide was initially used to remove pollutants from water. A uniform and durable coating of titanium dioxide was successfully applied to various surfaces. These coated surfaces demonstrated high degradation efficiency and long-term stability in degrading organic matter in water. To further improve the photocatalytic degradation efficiency of titanium dioxide, graphene was introduced to form titanium dioxide/graphene nanocomposites.

A new photoelectrocatalytic water purification system was developed by combining photocatalysis and electrochemistry. This scheme can be used to simultaneously remove both organic compounds and inorganic heavy metal ions from water. In this system, the working and counter electrodes are switched compared to traditional photoelectrocatalysis systems, with the metal or carbon electrode as the working electrode and the microchannels with photocatalyst serving as the counter electrode. A negative bias potential is applied to the working electrode to reduce the heavy metal ions, and the current flow through the circuit helps transfer the photo-excited electrons from the counter electrode (photocatalyst) to the working electrode. The inorganic heavy metal ions are thus reduced on the working electrodes while the photocatalytic degradation of organic pollutants on the counter electrode is enhanced.

Next, a micropump suitable for the water treatment and detection platforms was researched and developed. Valveless fluidic diode micropumps without moving parts are considered suitable for water sensor systems due to their simple structure and rapid mixing. In the design, topology optimization is used to design two-dimensional, fixed-geometry, fluidic diodes of high diodicity, which is the ratio of pressure drops of forward to reverse flows. One of the fluidic diodes, of the Tesla type, shows a diodicity of over five. The numerical simulation was applied to simplify the structures, and the two-dimensional geometry was converted into three-dimensional model for micropumps. Three-dimensional and unsteady numerical analyses of micropump were conducted for pumps with the two diode designs. The experiments conducted with designed diodes showed reliable repeatability and precise control of flow, indicating positive prospects for potential applications.

To achieve the envisioned closed-loop control water treatment platform, a highly sensitive low-cost sensor is essential. An electrochemical microfluidic sensor was developed for the high-sensitivity and low-cost detection of heavy metal ions in water. This sensor utilizes a glass carbon/graphene electrode synthesized through layer-by-layer self-assembly and subsequent pyrolysis. The electrode exhibited low overpotential, enabling detection of almost any heavy metal ions in aqueous solutions, and the incorporation of graphene resulted in a high sensitivity. To enhance mass transfer and sensitivity, a valveless micropump was integrated with the electrode, achieving two orders of higher sensitivity than those of measurements with a stationary solution and a detection limit as low as 20 ppt for lead and 100 ppt for cadmium. The developed sensor was employed to simultaneously detect lead and cadmium in water, investigating the mutual influence of heavy metal ions in electrochemistry. A neuron network model was adopted for data analysis.

In summary, this study presents a comprehensive approach to addressing the worldwide challenge of sustainable water resource management through the removal of pollutants and the detection of water pollutants. The closed-looped control water treatment platform, based on high-performance sensors, micropumps, and advanced photoelectrocatalysis technologies, provides an efficient and cost-effective solution to water scarcity and pollution. This platform offers promising prospects for the development of effective water management systems, which can contribute to the improvement of global water resources management and enhance the quality of life for people around the world.

Table of Contents

List of Figures

List of Abbreviations

AAS	Atomic absorption spectroscopy
AFM	Atomic force microscopy
ASV	Anodic stripping voltammetry
CFD	Computational fluid dynamics
COD	Chemical oxygen demand
FEGSEM	Field emission gun scanning electron microscope
GO	Graphene oxide
ICP-MS	Inductively coupled plasma mass spectrometry
LBL	Layer-by-layer
LOD	Limit of detection
UV	Ultraviolet
EDS	Energy-dispersive X-ray spectroscopy
MB	Methylene blue
MEMS	Microelectromechanical systems
PDDA	Poly (diallyldimethylammonium chloride)
PDMS	Polydimethylsiloxane
PEC	Photoelectrocatalysis
PEG	Polyethylene glycol
PSS	Poly (sodium styrene sulfonate)
PZT	Piezoelectric
rGO	Reduced graphene oxide
UDF	User defined function
XRF	X-ray fluorescence

List of Symbols

C	Contaminant concentrations
C_0	Contaminant concentrations at the beginning
k	Reaction rate constant
t	Time
d_1	Inner deflection
d_2	Outer deflection
a	Radius
b	Diameter
f	Frequency

Chapter 1: Introduction

1.1 Motivation and Background

Water scarcity and pollution are critical global challenges that have significant implications for sustainable development. Despite access to clean water being a fundamental human right, millions of people worldwide still lack access to safe drinking water.[1] To address these issues, the United Nations has identified them as key goals for sustainable development by 2030.[2] The impact of water scarcity is not limited to developing countries but is now also affecting developed countries, such as the United States, due to factors such as economic growth, demographic shift, and climate change. For instance, the U.S. Southwest is currently facing a megadrought, with the Colorado River named as the most endangered river in the country due to a nearly 20% decline in its water flow.[3]

The pollution of water is also a significant problem worldwide. According to a global survey by the Food and Agriculture Organization of the United Nations, over 80% of wastewater is discharged into the environment without proper treatment, leading to 800,000 deaths in 2012.[4] In the United States, about 40% of surface water, including rivers, streams, and lakes, are in poor biological conditions due to nutrient pollution, which is becoming a nationwide problem.[5] Water pollution occurs due to the discharge of various contaminants, including suspended solids, organic matter, nutrients, pathogens, metals, and inorganic dissolved matter. The main sources of these contaminants are agriculture and industry.[6] Organic pollution, measured by the Chemical Oxygen Demand (COD), has significant impacts on the economy and human health, with one study revealing that oneseventh of the rivers and streams in Africa, Asia, and Latin America are severely affected by organic pollution. Metals are another type of toxic water pollutant that threatens human health. The US Environmental Protection Agency lists nine metals to limit as contaminants in drinking water.[7] The Flint water crisis, which was mainly caused by lead leached from lead water pipes, is a recent example of lead pollution in the US. In this case, starting in 2014, the blood lead level in children younger than 5-years-old increased significantly from 2.4% to 4.9%. When this value goes above 6.6%, it causes irreversible effects on IQ, ability to pay attention and academic achievement.[8]

The high levels of organic pollutants and inorganic heavy metal ions endanger aquatic organisms and pose a threat to human health, leading to diseases such as acute and chronic gastrointestinal diseases, diarrheal diseases, typhoid fever, paratyphoid fever, and lower respiratory tract infections. Water pollution was attributed to 1.4 million deaths in 2019 and around 297,000 death of children under the age of 5-year-old each year, underscoring the importance of proper water treatment water quality monitoring technologies in addressing both the global water shortage problem and ensuring the quality of drinking water and the health of those consuming it.[9]

Conventional water purification technologies, such as adsorption, coagulation, sedimentation, chemical filtration, and membrane filtration, have high operational costs and relatively low efficiency. These methods cannot eliminate pollution, and they also generate toxic secondary pollution.[10] More advanced technologies for water treatment have been developed, such as membrane filtration and semiconductor photocatalytic processes. The membrane filtration technique is one of the methods that is widely supported because of its simple operation process that can occur at room temperature, low energy consumption, high efficiency, and low investment.[11] The size of pores in nanoporous membranes ranges from nanometers to subnanometers. This makes it possible to filter most pollutants such as metallic ions, organic molecules, salts, and microbes from wastewater.[12] However, low throughput and membrane fouling are two of the key technical problems still to be solved.

Another promising approach to water treatment is the semiconductor photocatalytic process. This technology uses semiconductor catalysts such as titanium dioxide ($\mathrm{TiO_2}$) to mineralize refractory organic compounds, water pathogens and disinfection by-products.[13] When $\mathrm{TiO_2}$ is illuminated under photo energy greater than or equal to the bandgap energy of $\mathrm{TiO_2}$, the distinct lone electron in the outer orbital is photoexcited to the empty conduction band, leaving a hole in the valence band. A series of redox reactions occur at the photo active surface that can mineralize refractory organic compounds, water pathogens and disinfection by-products.[14] The application of the photocatalytic process in water treatment has been studied for a long time since the discovery of photocatalytic effect on water splitting by Fujishima and Honda in 1972 using a $\mathrm{TiO_2}$ electrode.[15] Although the photocatalytic process has been studied for a long time, the primary barriers that prevent the practical application of this technology are low efficiency, catalyst agglomeration during operation, and the complex post-separation process.[16]

Similar to the development of water purification technology, the evolution and application of water quality detection technology also face many obstacles. Taking heavy metal ion sensors as an example. Heavy metal refers to any metallic chemical element that has a relatively high density and is toxic or poisonous at low concentrations. Arsenic (As), cadmium (Cd), chromium (Cr), copper (Cu), lead (Pb), and zinc (Zn) are a few of most commonly considered heavy metals. They come from natural sources such as weathering of metal-bearing rocks and volcanic eruptions, as well as human activity such as mining and various industrial and agricultural activities.[17] As non-biodegradable, toxic and persistent pollutants, heavy metal pollutant causes a potential health threat to their consumers including humans. Several acute and chronic toxic effects of heavy metals affect different body organs. Gastrointestinal and kidney dysfunction, nervous system disorders, birth defects, and cancer are examples of the complications of heavy metals toxic effects.[18] There are existing analytical tools that have been developed for measurement of heavy metal ions such as cold vapor atomic fluorescence, atomic absorption, chromatography, and emission spectroscopies. However, these tools require infrastructure, time, and workforce, and they can only be performed in centralized laboratory facilities.[19] Electrochemical testing has also been confirmed feasible for heavy metal ion testing, but its performance in complex environments where multiple heavy metal ions coexist is still a challenge. Its low system integration also hinders the practical application of this method.[20]

Therefore, this research aims to address the fundamental problems in water purification and water quality detection, to eliminate barriers that limit their development. Through a more integrated and comprehensive water purification platform, this study aims to contribute to the sustainable development of water resources.

1.2 Objectives of Research

The objective of this study is to provide an efficient photocatalytic degradation scheme and a highly sensitive sensor for an intelligent water treatment platform for sustainable water resources management. To accomplish the intended final research objectives, three specific aims were proposed and gradually achieved throughout the research process.

Aim 1: To establish a high-performance water treatment system based on photocatalysis and electrochemistry, which can simultaneously degrade organic pollutants and remove inorganic heavy metal ions from water. The development of this system relies on the synthesis of highly efficient photocatalysts and the coating of substrates. Through a deep investigation of photocatalysis and its combination with electrochemistry, a new structure for photocatalytic water treatment was proposed, which achieved efficient degradation of organic pollutants while simultaneously removing heavy metal ions from water.

Aim 2: To develop a fluid micropump suitable for the designed water treatment and detection system. The fluid micropump has a dual function as both an actuator and a micromixer. On the one hand, it can drive the flow of liquid to the system. On the other hand, it can accelerate the mass transfer process by utilizing its unique motion mode. Its combination with the heavy metal ion sensor further enhances its sensitivity, creating a lower detection limit.

Aim 3: To develop a highly sensitive, low-cost, and user-friendly small heavy metal ion sensor. This sensor is based on the technology of anodic stripping voltammetry in electrochemistry and integrates an innovative glassy carbon/graphene composite electrode and microfluidic system, achieving an extremely low detection limit and excellent long-term stability for the detection of almost all types of heavy metal ions.

The proposed objectives and outcomes of this research not only aim to provide clean drinking water, but also represent a significant advancement over a broad range of water treatment and sensing technologies. The achievements will offer a solution to current ineffective and costly water treatment systems employed in water treatment plants, ensuring clean drinking water. The monitoring and detection of environmental water and drinking water will also benefit from the development of heavy metal ion sensors. On a larger scale, the vision of this project is to enhance the quality of drinking water, reduce the expense of wastewater treatment, alleviate the current water pollution crisis, and ultimately address the issue of water resource scarcity.

1.3 Thesis Overview

Chapter 2 mainly introduces the synthesis and coating of a new reduced graphene oxide/titanium dioxide (rGO/TiO_2) photocatalyst and its application to the photocatalytic degradation of organic pollutants. The working principle of the graphene/titanium dioxide photocatalyst and the influence of different substrate materials on the efficiency of photocatalytic water treatment are investigated. Finally, the rGO/TiO_2 composite material is fixed on a shrinkable thermoplastic film through layer-by-layer (LBL) self-assembly to enhance the removal of pollutants in water. The photocatalytic efficiency is measured by the photodegradation of methylene blue (MB) under sunlight. A 10 mL MB solution with a concentration of 10 μM is completely degraded within 1 hour, and the photocatalytic efficiency does not decrease after 5 hours of operation.

Chapter 3 introduces the newly designed photoelectrocatalytic water treatment system. This chapter presents the basic principles of existing photoelectrocatalytic water treatment technologies and the proposed structure of the new photoelectrocatalytic system, comparing their differences. The experimental section includes the preparation of photoelectrocatalytic electrodes, a comparison of the efficiency of photoelectrocatalytic degradation of organic pollutants and inorganic heavy metal ions in two modes in bulk solution, and the integration of the designed photoelectrocatalytic water treatment system into a microchannel using MEMS technology, with a demonstration of its ability to simultaneously remove organic and inorganic pollutants in water.

In Chapter 4, the design, simulation, fabrication, and testing of a valveless micropump based on topology optimization are presented. In this section, topology optimization is used to design a fixed-geometry fluidic diode of high diodicity. Subsequently, the fluid diode is used in a valveless micropump. Computational fluid dynamics (CFD) is used to perform three-dimensional unsteady numerical analysis of fluid flow inside the micropump with optimized diodes. The performance of the nozzle-diffuser type diode in the valveless micropump is also evaluated under similar conditions for comparison. Two types of micropumps are manufactured and tested. The results indicate that the flow rate of the micropump using the designed Tesla diode can reach 33.5 mL/h, which is consistent with the simulation results and 2.2 times higher than that of the nozzle-diffuser type micropump.

In Chapter 5, the investigation of a highly sensitive heavy metal ion sensor based on a new electrode material and integrated with a microfluidic system is presented. The sensor utilizes a newly developed electrode formed by pyrolysis of photoresist and graphene to detects trace amounts of heavy metals through anodic stripping voltammetry. The sensor can detect almost all heavy metal ions in aqueous solutions due to its low overpotential. The sensor is integrated with a nozzle-diffuser valveless micropump, and the detection limits for lead and cadmium ions are 20 ppt and 100 ppt, respectively, at an average flow rate of 10 mL/h. The work focuses on the effect of mass transfer processes on electrochemical sensors and the mutual interference of various heavy metal ions during electrochemical detection. Finally, a model for the detection of multiple ions based on electrochemistry is established using neural networks.

In Chapter 6, a summary of all the work done during this research, including the development of an efficient photocatalytic degradation scheme, the design of a fluid micropump, and the development of a highly sensitive heavy metal ion sensor, was presented. In addition, an outlook for future works was also discussed.

Chapter 2: Photocatalytic Water Purification

2.1 Introduction

Photocatalytic technology based on titanium dioxide (TiO_2) has gained wide attention in the past decades as a low-cost, environmentally friendly, and sustainable water treatment technology. This technology uses semiconductor catalysts such as TiO_2 to mineralize refractory organic compounds, water pathogens and disinfection by-products.[21] When TiO_2 is illuminated under photon energy greater than or equal to the bandgap energy of TiO_2, the distinct lone electron in the outer orbital is photoexcited to the empty conduction band, leaving a hole in the valence band. A series of redox reactions occur at the photo active surface and can remove the organics in water.[22] However, low efficiency, catalyst agglomeration during operation, and the complex post-separation process are the primary barriers that prevent practical applications of this technology.

Graphene, a flat monolayer of sp^2-bonded carbon atoms, is believed to be very effective in increasing photocatalytic efficiency because of the enhanced charge transfer rate.[23] Many approaches have been applied to synthesize graphene-based TiO_2 photocatalysts. For example, Guo et al. used an ultrasonic assisted chemical reaction to synthesize rGO/ TiO_2 composite material and observed 2.57 times enhanced photocatalytic efficiency.[24] Safardoust-Hojaghan and Salavati-Niasari synthesized rGO/ TiO_2 composite material using a hydrothermal method, and it showed 2.13 times faster photodegradation rate than TiO_2.[25] All of these chemical methods require complex and expensive chemical reactants, and the final products are in powder form, which is difficult to be immobilized on the substrate.

As the slurry of TiO_2 and rGO/ TiO_2 composite material requires a post-separation process and leads to catalyst agglomeration during operation, hindering the practical application of this technology,[26] some researchers tried to deposit photocatalysts using chemical vapor deposition, atomic layer deposition and, most commonly, the sol–gel method.[27, 28, 29] However, all these methods start with a titanium precursor and require complex chemical reactions. In addition, the enhancement of photocatalytic efficiency with graphene-based TiO_2 becomes limited when the composite material is immobilized on the surface of the substrate due to a reduction of active sites involved in the reaction. For example, Padoin et al. immobilized rGO/ TiO_2 composite material on the walls of microchannels, and only 29% enhancement was observed, compared to immobilized pure TiO_2.[30]

Instead of using these chemical deposition methods, the physical LBL self-assembly is more convenient, and can produce a high-quality TiO_2 film on a substrate. The basic mechanism of LBL self-assembly is the electrostatic interaction between the polymer and particles with opposite charges.[31] Multilayered TiO_2 or rGO/ TiO_2 films can be deposited onto an electrically charged substrate by dipping the substrate into successive solutions of opposite charges. This deposition routine can be repeated many times to fabricate multilayer photocatalyst thin films. TiO_2/Polymer nanocomposite films have been successfully fabricated since 1997, when Liu et al. fabricated as many as 120 layers of films on silicon, metal and plastic substrates.[32] Yao et al. fabricated a graphene-based TiO_2 photocatalysts on glass substrate in a sequence of GO/PDDA/TiO_2 while Manga et al. fabricated the material in a sequence of PEI/TiO_2/PEI/GO.[33, 34] Manga's group also used femtosecond transient absorption spectroscopy to demonstrate the ultrafast photocatalytic electron transfer between TiO_2 and graphene. Different substrate materials were used to increase the surface area of the photocatalyst to increase the photocatalytic efficiency. For example, TiO_2 was deposited on glass spheres with a diameter of 5 mm, and then put in a lab scale compound parabolic collector to photodegrade methylene blue (MB).[35] Wang et al. successfully fabricated carbon nanotubes and TiO_2 composite films on cotton fabrics to achieve high photocatalytic efficiency.[36] They learned that their irregular shapes and material properties make them hard to use when fabricating microfluidic systems or flexible structures.

In the present work, a shrink thermoplastic film was used as a substrate material as it can shrink more than 80% of its original size after heating. It has been successfully used in microsensors to enhance sensitivity and reduce the limit of detection,[37] but it has never been used in photocatalytic water treatment. TiO_2 films and rGO/ TiO_2 composite films were LBL self-assembled on shrink polymer films. The photocatalytic efficiency was measured and compared with TiO_2 films on a glass substrate, and the morphological properties were measured to explain the difference.

2.2 Body of Knowledge

The semiconductor TiO_2 has been widely studied and utilized as a photocatalyst for water purification, water splitting and other photocatalytic applications. The working mechanism of TiO_2 is shown in Figure 2.1a. The photon energy can excite the electron in the valence band to the conduction band and leave a hole in the valence band. A series of chain oxidizing-reductive reactions can then oxidize organics directly or indirectly by producing active radicals. There are three different crystal structures of TiO_2 including rutile, anatase and brookite. The energy band gap differs for different crystal structures (3.2 eV for anatase and 3.0 eV for rutile). The rutile has a broader photoactive range while anatase has higher photocatalytic activity due to its higher conduct band energy and more lattice defects.[38] Defects and dislocations in the anatase phase lattice can generate more oxygen vacancies to capture electrons, making photogenerated electrons and holes easier to separate.

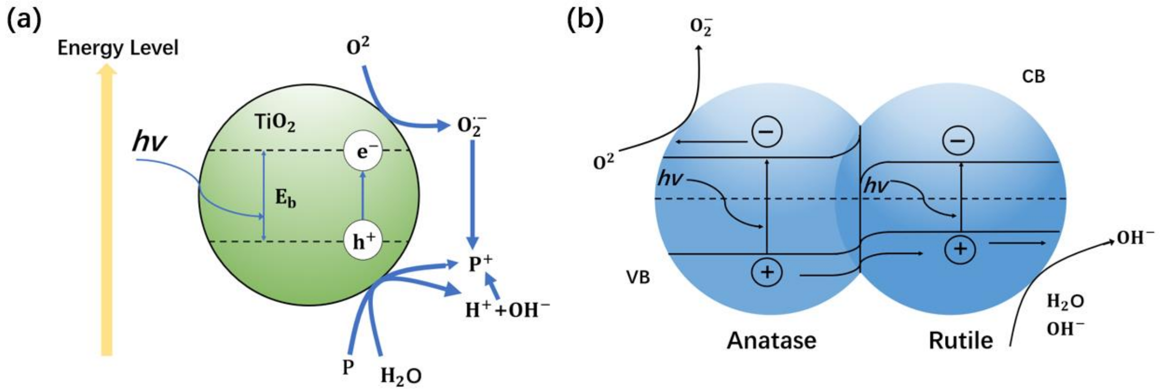

Figure 2.1 (a) Working mechanism of TiO_2; (b) Synergistic effect between anatase and rutile.

The commercial product Aeroxide® P25 is reported to have the highest photocatalytic activity higher than pure TiO_2. Its high photocatalytic activity originates from the synergistic effect.[39] The P25 contains anatase and rutile phases in a ratio of about 3:1, and the bending of the energy band can be generated when these two phases come together. Figure 2.1b shows the energy band structure of anatase and rutile after bending. The holes in the valence band can transfer from anatase to rutile, but the electrons in the conduction band cannot travel between two phases. Thus, the electrons and holes are separated, and recombination is inhibited. The P25 is regarded as a standard material in the field of photocatalytic reactions and is used in this project.

2.3 Layer-by-Layer Self-Assembly

As the pre-processing for LBL self-assembly, dispersion of TiO_2 powder in water is a technical problem that must be solved. The van der Waals force indicates that although the nanoparticles intend to aggregate, electrostatic repulsion due to a double layer hinders this process.[40] Based on the DLVO theory, pH value, solvent, concentration of ions and the functional groups at the surface of nanoparticles all impact the zeta potential of nanoparticles and hence affect the process of agglomeration. [41]

The effect of pH was tested, and the particle sizes were measured in different conditions. Based on the DLVO theory, when the pH is lower than the isoelectric point pH, which is about 5 for the P25, the surface of the particle is positively charged. When the pH is higher than the isoelectric point pH, a negatively charged surface and zeta potential can be expected.

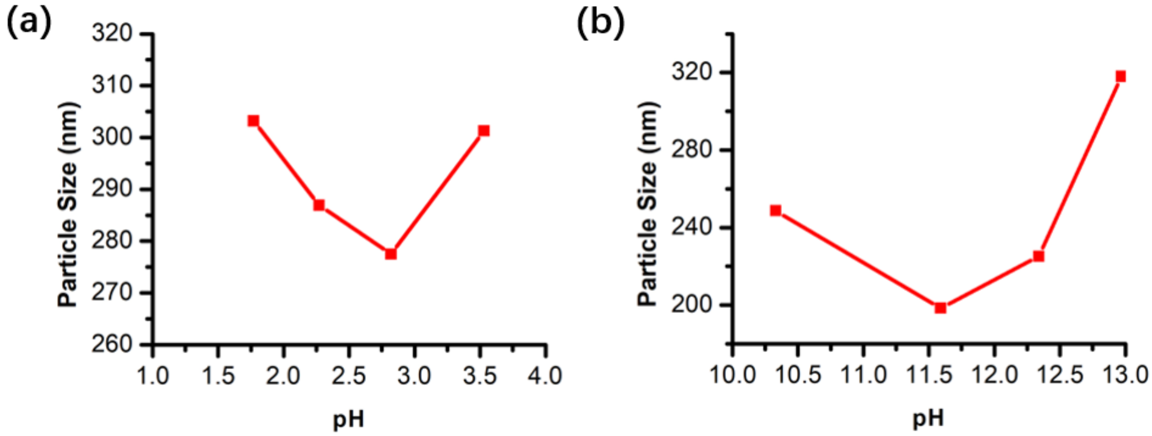

Figure 2.2 pH effect on TiO_2 particle size in water dispersion (a) low pH (b) high pH.

Figure 2.2 shows the experiment results for measured particle size under various pH values. The polyethylene glycol (PEG) with a 400 molecular weight is used as the dispersant to cause steric repulsion between particles and help prevent agglomeration. Ultrasonic treatment was applied to reduce the particle size. The results show that the smallest particle size can be expected when the pH value is around 3 in an acidic condition and 12 in an alkaline condition. Further reduced or increased pH values enhances agglomeration because of the increased ion strength. Thus, a 1 wt% TiO_2 water dispersion can be prepared with pHs of 3 or 12. Since the graphene is negatively charged, only positively charged TiO_2 was used in the following experiments.

The basic mechanism of LBL self-assembly is the electrostatic interaction between polymer or particles with opposite charges.[42] Multilayered films can be deposited onto an electrically charged substrate by dipping the substrate into alternating solutions of opposite charges. This deposition routine can be repeated many times, accompanied by washing out of non-bound molecules after each layer is deposited. Figure 2.3 shows the procedure of the LBL self-assembly method.

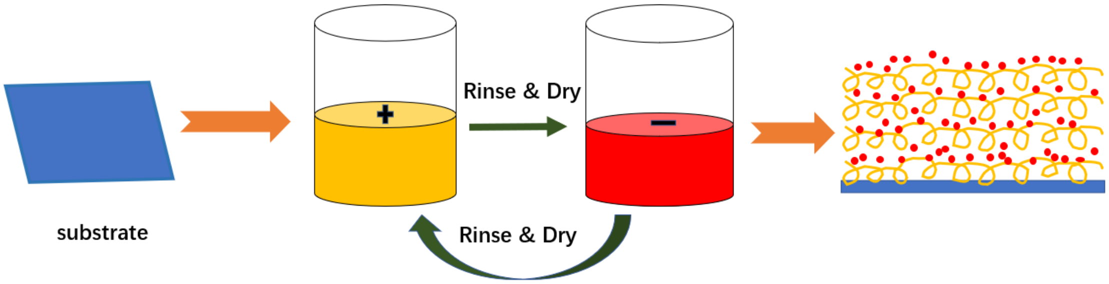

Figure 2.3 Process flow of the LBL self-assembly method.

The LBL self-assembly method can be used to fabricate $\mathrm{TiO_2}$ thin films as well as graphene/ $\mathrm{TiO_2}$ composite films.[43] The surface charge of $\mathrm{TiO_2}$ can be controlled by changing the pH value based on DLVO theory. Either positively charged polyelectrolyte PDDA (poly(diallyldimethylammonium chloride)) or negatively charged PSS (poly(sodium styrene sulfonate)) can be used as polymers of opposite charges. For example, when the positively charged $\mathrm{TiO_2}$ is used, the negatively charged PSS can be used for PSS/ $\mathrm{TiO_2}$ bilayers. A $\mathrm{TiO_2}$ thin film with 5 PSS/ $\mathrm{TiO_2}$ bilayers can be produced by dipping the negatively charged substrate into a solution following the sequence of $\mathrm{PDDA} + \mathrm{PSS} + \mathrm{PDDA} + (PSS + \mathrm{TiO_2})_5$. The first few layers of PDDA and PSS are used to make sure the substrate is uniformly charged.

The reduced graphene has a negative charge at its defect points, so it can also be used in the LBL self-assembly. As a result, the LBL self-assembly method can synthesize graphene/$\mathrm{TiO_2}$ composite films in a sequence of $\mathrm{PDDA} + \mathrm{PSS} + \mathrm{PDDA} + (\mathrm{Graphene} + \mathrm{TiO_2})_5$ by using graphene and positively charged $\mathrm{TiO_2}$. As the negative charges on graphene are not enough in quantity or uniformity, graphene oxide (GO) might be a useful alternative material. GO has more functional groups on it, so it can attract more $\mathrm{TiO_2}$ nanoparticles. The GO/ $\mathrm{TiO_2}$ composite material can be fabricated using the same sequence as graphene/ $\mathrm{TiO_2}$ composite material. Then the GO can be reduced into graphene by $\mathrm{TiO_2}$ under UV illumination, and the graphene/ $\mathrm{TiO_2}$ composite material can be obtained.

2.4 Fabrication and Characterization

A 1 wt% TiO_2 cationic solution was prepared by adding 1 g TiO_2 and 1 mL HCl (1 M) into 100 mL deionized water, followed by more than 24 h of continuous stirring until a stable colloid solution was formed. The GO solution was diluted to 1 mg/mL with deionized water, followed by slight sonication to prevent agglomeration and obtain a higher percentage of monolayer flakes. A shrink thermoplastic film was cut into 4.5 cm squares, and the 1.8 cm square glass was also used for comparison.

The substrates were first cleaned by deionized water and dried in air. Then the substrates were alternately immersed into cationic PDDA and anionic PSS solutions in a sequence of [PDDA+PSS+PDDA]. The long-chain polymers with charged branches helped to form a uniformly film on the substrates. Next, the PSS/ TiO_2 bilayers or GO/ TiO_2 bilayers were deposited on top of the substrates. Different numbers of composite photocatalyst bilayers were prepared. Deposition time for each process was 10 min, accompanied by the washing out of non-bound molecules after each layer was deposited.

The coated shrink thermoplastic films were heated in the oven under 150 °C. The film size after shrinking was 1.8 cm by 1.8 cm, the same as the cover glass. Then the ultraviolet light illumination was applied to reduce GO into rGO.[44]

The surface morphologies and elemental mapping of samples were observed by a Field Emission Gun Scanning Electron Microscope (FEGSEM) (Hitachi SU8230). A thickness of 2.5 nm Iridium was deposited on each sample to increase the conductivity. The three-dimensional surface topography was measured by Atomic Force Microscopy (AFM) (MFP-3D Origin AFM, Asylum Research).

The morphology of immobilized photocatalysts was observed by SEM. Figure 2.4 shows the SEM images of 4 PSS/TiO_2 bilayers on both a glass substrate and a shrink thermoplastic film and 4 rGO/TiO_2 bilayers on the shrink thermoplastic film. It can be found that the PSS/TiO_2 bilayers on glass substrate were relatively flat, and the porous structure between photocatalysts was in nanoscale. The ultra-high-resolution image of glass sample clearly shows the TiO_2 nanoparticles. The size of TiO_2 nanoparticles were about 20-25 nm which matches the particle size of P25. Comparing the photocatalysts on the glass substrate with the shrink thermoplastic films, Figure c and e show many folds produced by shrinking, which means a higher surface area can be expected on shrink thermoplastic films. It also leads to the microscale porous structures on the substrate. The amount of folds was similar between PSS/TiO_2 and rGO/TiO_2 composite films on shrink thermoplastic films, but Figure c, d show the surface of the folds was rougher than Figure e, f. This is because there is more TiO_2 immobilized on PSS than rGO as the negatively charged functional groups on GO is much less than PSS.

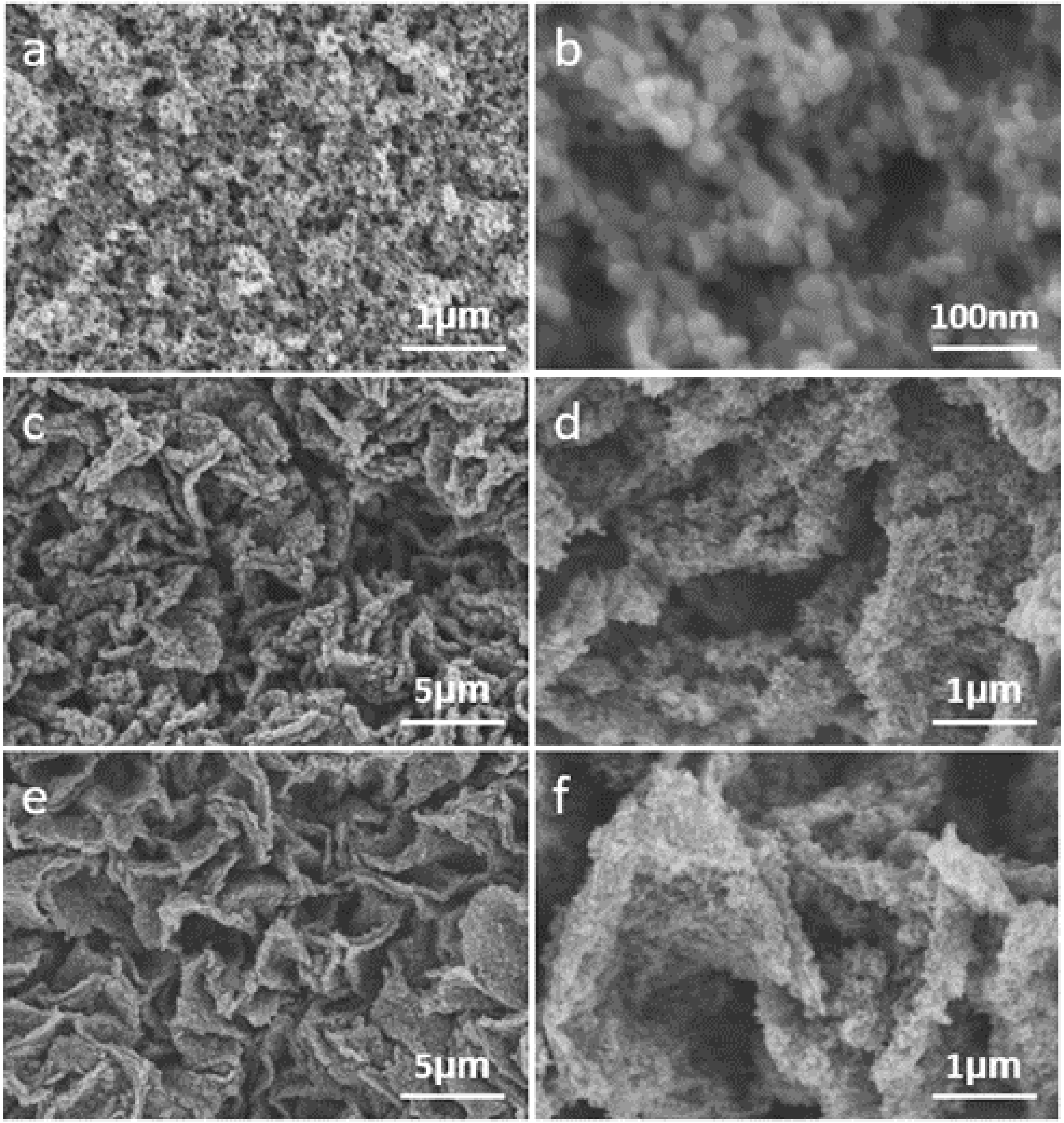

Figure 2.4 SEM images of different photocatalyst in different substrate (a) 4 PSS/TiO_2 bilayers on glass substrate, high resolution; (b) 4 PSS/TiO_2 bilayers on glass substrate, ultra-high resolution; (c) 4 PSS/TiO_2 bilayers on shrink polymer, low resolution; (d) 4 PSS/TiO_2 bilayers on shrink polymer, high resolution; (e) 4 GO/TiO_2 bilayers on shrink polymer, low resolution; (f) 4 GO/TiO_2 bilayers on shrink polymer, high resolution.

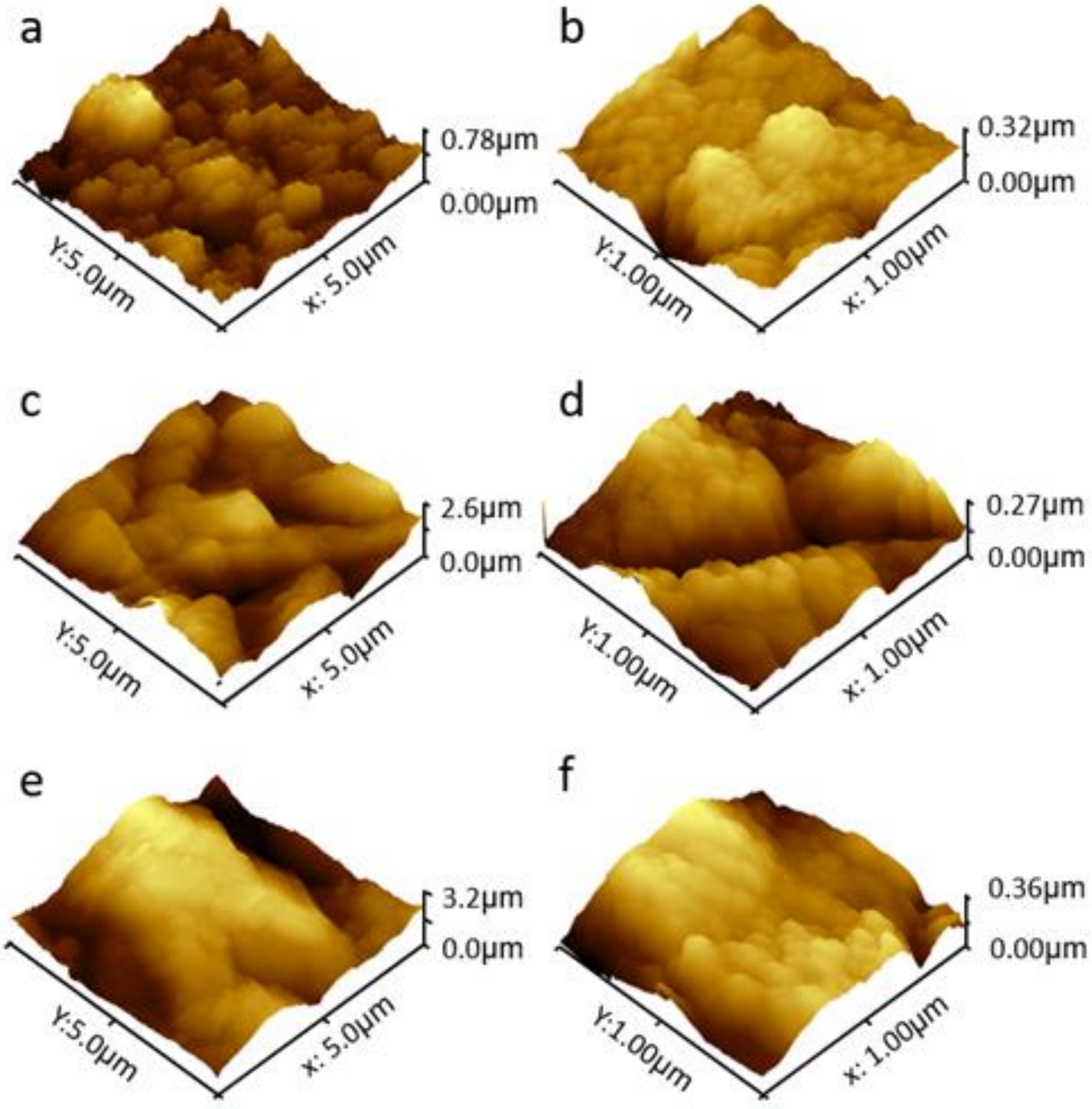

Figure 2.5 AFM images of different photocatalyst in different substrate (a) 4 PSS/TiO_2 bilayers on glass substrate, low resolution; (b) 4 PSS/TiO_2 bilayers on glass substrate, high resolution; (c) 4 PSS/TiO_2 bilayers on shrink polymer, low resolution; (d) 4 PSS/TiO_2 bilayers on shrink polymer, high resolution; (e) 4 GO/TiO_2 bilayers on shrink polymer, low resolution; (f) 4 GO/TiO_2 bilayers on shrink polymer, high resolution.

Figure 2.5 shows the AFM images of different photocatalysts on different substrates. Similar to the SEM images, the photocatalysts on a glass substrate were smoother than that on a shrink polymer substrate. In a square with a side of 5 μm, the height difference of photocatalysts on the glass substrate was 783 nm, while the value on the shrink polymer substrate with different photocatalysts were 2.644 μm and 3.315 μm, respectively. The microscale folds on the shrink polymer are visible in AFM images. The particle size shown in high resolution images are in a range from 20 nm to 25 nm, which matches the SEM results.

2.5 Photocatalytic Tests and Efficiency

The photocatalytic efficiency was evaluated by photodegradation of MB solutions. Different numbers of PSS/$\mathrm{TiO_2}$ bilayers on shrink polymer films were first tested and compared. As shown in Figure 2.6a, concentration of MB kept decreasing with increasing illumination time. The concentration changes of MB slowed down when its concentration was lower, thus the kinetics of MB photodegradation can be described by the first order kinetics equation:

$$\ln \ln \left(\mathrm{C}/\mathrm{C_0}\right) = -\mathrm{kt}$$

where C and $\mathrm{C_0}$ are the contaminant concentrations at the beginning and during light illumination, respectively, k is the reaction rate constant, and t is time.[45] The photocatalytic efficiency can be represented by reaction rate constant, k, which is also the slope in Figure 2.6b. When the number of PSS/$\mathrm{TiO_2}$ bilayers is higher, k is also higher, and the value of k gets saturated when the number of bilayers is 4. This means several PSS/$\mathrm{TiO_2}$ bilayers greater than 4 will not significantly change the photodegradation efficiency. This is because the bottom photocatalyst was covered by the upper photocatalyst, and only the upper photocatalyst could receive light illumination and photodegrade MB. When the number of PSS/$\mathrm{TiO_2}$ is 4, $\mathrm{k} = 0.0173/\mathrm{min}$.

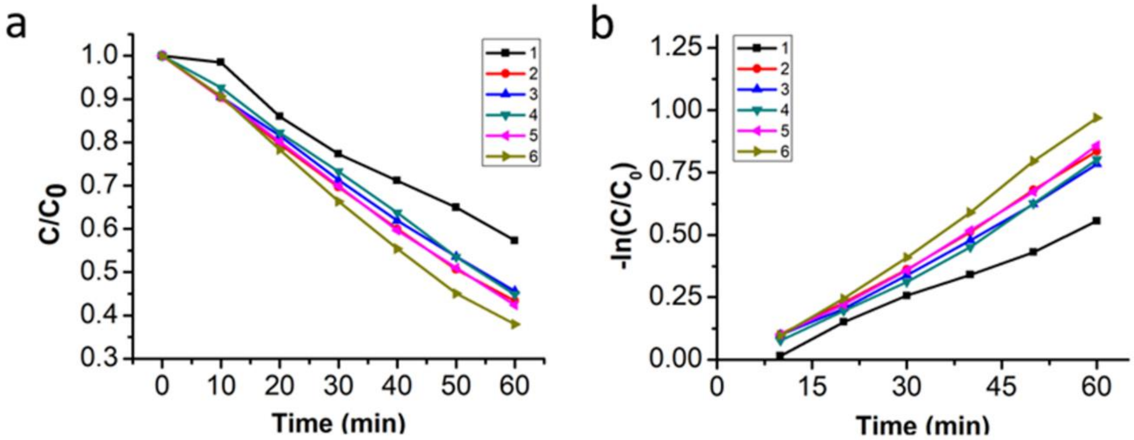

Figure 2.6 (a) Relative MB concentration versus irradiation time with different numbers of PSS/ TiO_2 bilayers; (b) MB degradation kinetics for different numbers of PSS/ TiO_2 bilayers.

The same tests were done in different numbers of PSS/TiO_2 bilayers on a glass substrate and rGO/TiO_2 bilayers on a shrink polymer substrate. The results are shown in Figure 2.7.

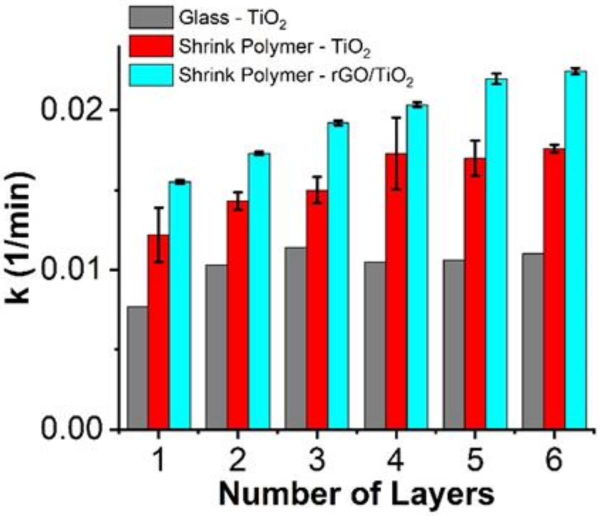

Figure 2.7 Pseudo first order kinetic constant for different numbers of PSS/TiO_2 and graphene/ TiO_2 bilayers on different substrates.

Figure 2.7 shows that the PSS/TiO_2 bilayers on a glass substrate always have the lowest photocatalytic efficiency, and the highest photocatalytic efficiency observed was

$k = 0.0106$ /min. The highest photocatalytic efficiency was obtained in shrink polymer with 6 rGO/TiO_2 bilayers. The highest reaction rate constant was $k = 0.0222$ /min, 2.1 times higher than PSS/TiO_2 bilayers on glass substrate and 1.28 times higher than PSS/TiO_2 bilayers on a shrink polymer substrate.

The high photocatalytic efficiency for rGO/TiO_2 bilayers on a shrink polymer can be attributed primarily to two reasons: the high surface area induced by shrink and enhanced electron transfer due to graphene material. As the original size of shrink polymer is 6.25 times higher than the size after shrinking and covering the glass, the amount of immobilized photocatalyst is also higher than cover glass. The enhancement of photocatalytic efficiency by introducing graphene material has been verified by many publications. Even though the amount of TiO_2 in rGO/TiO_2 bilayers is less than PSS/TiO_2 bilayers, the enhanced electron transfer prevents photoexcited electron-hole recombination and improves the photocatalytic efficiency even beyond that of PSS/TiO_2 bilayers.

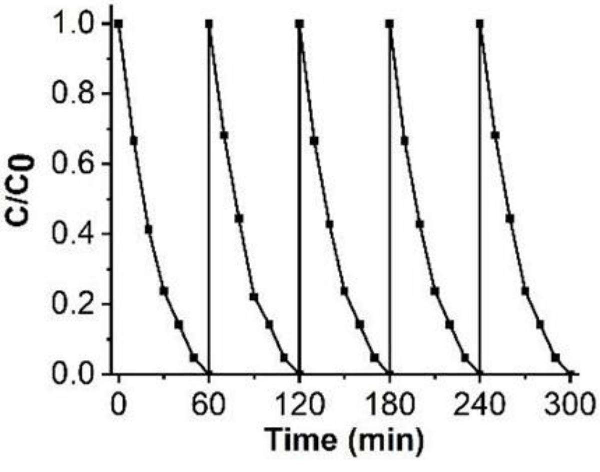

Figure 2.8 Relative MB concentration versus irradiation time in cycling test.

The cycling tests were also performed to show the long-term stability of LBL self-assembled rGO/TiO_2 bilayers on shrink polymer. A sample with 4 rGO/TiO_2 bilayers on shrink polymer was used for this test. 10 mL MB solution with 10 μM concentration was fully degraded within 1 h. The process was repeated 5 times, and the result was shown in Figure 2.8. It can be inferred from the figure that no decrease of photocatalytic efficiency was observed, which means that the bonding between photocatalyst and substrate is firm and the result is repeatable.

2.6 Conclusion

This study shows that the photocatalyst can be firmly immobilized on glass substrates and on shrink thermoplastic films using LBL self-assembly. The folds' structure induced by shrinking helps increase photocatalytic efficiency by 63%, and the introduction of graphene material further enhances the photocatalytic efficiency to 2.1 times higher than pure TiO_2 immobilized on a glass substrate. Overall, more than 70% of 100 μM MB was removed in 1 hour using rGO/TiO_2 bilayers immobilized on a shrink thermoplastic film, and the 10 μM MB can be fully removed within 1 hour.

Chapter 3: A New Photoelectrocatalysis Water Purification Configuration for Simultaneous Removal of Organic Pollutant and Heavy Metal Ions in Water

3.1 Introduction

Photocatalytic water treatment based on photocatalysts is a promising low-cost and sustainable water treatment technology. This technology uses electron-hole pairs generated by photocatalysts under light illumination to produce active radicals that degrade organic pollutants in water.[46] However, its efficiency is limited by the recombination of photoexcited electrons and holes, which reduces the lifetime of photogenerated holes.[47,48]

Numerous methods have been developed to prevent the recombination of electrons and holes in photocatalysts. For example, heterostructured photocatalysts prevent electron-hole recombination by transferring photoexcited electrons from a semiconductor with a higher conduct band minimum to one with a lower conduct band minimum.[49,50] The TiO_2/CdS system was the first heterostructured photocatalyst designed by Spanhel et al. in 1987.[51] A significant amount of research has attempted to improve photocatalytic efficiency by doping metals,[52, 53] metal oxides,[54] non-metals,[55] or graphene[56, 57, 58] onto photocatalysts to transfer photogenerated electrons. However, these methods involve transferring electrons to a lower energy level, leading to the release of a portion of the potential energy of the transferred electrons and a reduced redox potential, which limits the scope of application of photocatalysis.

Photoelectrocatalysis (PEC) is considered an effective method for addressing the recombination of electron-hole pairs in photocatalysts. PEC involves applying a bias potential to a photocatalyst to induce electron migration from the photocatalyst to another electrode, thereby achieving the separation of electron-hole pairs and enhancing the efficiency of photocatalysis. Studies have reported that applying a bias potential as low as 0.1 V can achieve 2.59 times higher photodegradation efficiency.[59] Another significant benefit of PEC is the removal of heavy metal ions at the cathode due to the reducing ability of electrons in the counter electrode.[60, 61, 62] However, the heavy metal ions that can be reduced at the cathode are limited.[63] For example, in titanium dioxide (TiO_2) base PEC system, although published works have shown that heavy metal ions with high redox potential, such as copper and lead, can be reduced by photogenerated electrons. The potential of these electrons is generally considered insufficient to reduce heavy metal ions with lower redox potential, such as cadmium.[64]

Therefore, this study presents a novel configuration of a three-electrode system-based PEC water purification system that is distinct from the existing setups, achieving the reduction of all heavy metal ions and the efficiency enhancement of photocatalytic organic degradation.

3.2 Body of Knowledge

Figure 3.1 illustrates the working principle of photoelectrocatalytic water treatment. As shown in the figure, a bias potential is applied between the TiO_2 electrode and counter electrode to allow electron transfer.

The bias potential applied on photocatalyst migrate electrons from photocatalyst to another electrode which transfers the photocatalysis into photoelectrocatalysis, and the

PEC is more efficient on degradation of pollutants compared to electrolysis and photocatalysis under similar experimental conditions.[65]

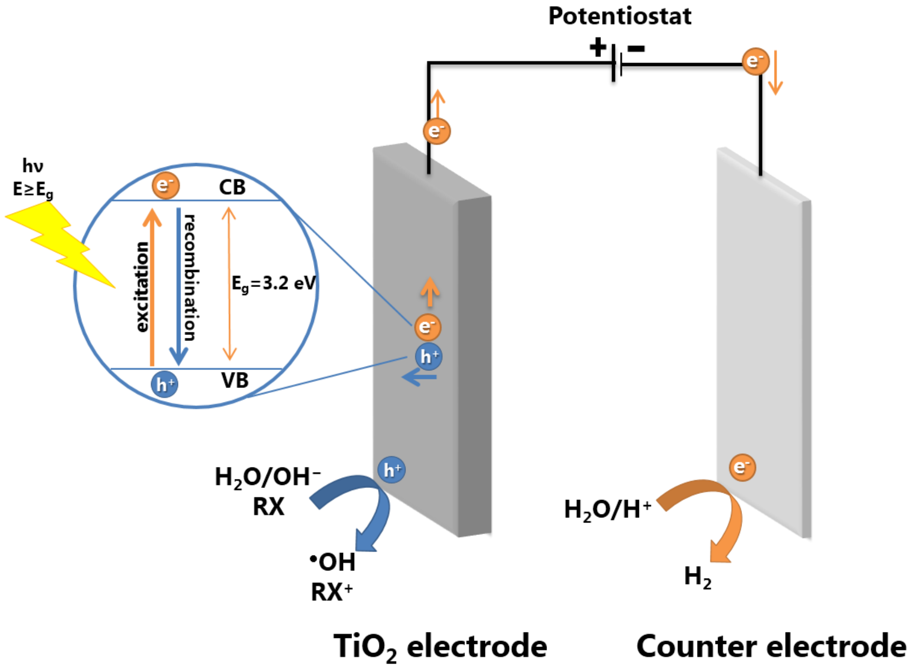

Figure 3.1 Mechanism of photoelectrocatalytic water purification.

The PEC can be divided into three processes.[66] The semiconductor is first illuminated by UV light to generate excited electrons in the conduct band and leave holes in the valence band. Then the bias potential applied between the graphene/ TiO_2 electrode and counter electrode leads to the electron transfer from the graphene/ TiO_2 electrode to counter electrode, and the electron-hole pairs are effectively separated. Finally, holes are left in the graphene/ TiO_2 electrode to generate active radicals and oxidize pollutants in the water, while the electrons are left in the counter electrode, leading to a reduction reaction.

Photocatalytic efficiency increases due to the efficient electron-hole separation. There are another two important benefits of the photoelectrocatalytic water degradation. First, it avoids the dependence of the photocatalytic process on dissolved oxygen in water.

The excited electrons react with the dissolved oxygen to form $O_2^{\cdot -}$ radicals to oxidize organic materials in water. With the consumption of dissolved oxygen, the electrons are accumulated, and the electron-hole recombination is enhanced, so the traditional photocatalytic efficiency is highly dependent on dissolved oxygen in the water. However, with the existence of bias potential, the electrons are transferred to the counter electrode, leading to a reduction reaction on the counter electrode. The dissolved oxygen does not participate in the photocatalysis reaction, nor does it affect photocatalytic efficiency. [67] Another significant benefit of photoelectrocatalytic water degradation is that heavy metal ions can be removed at the cathode of a reactor, which is the counter electrode, by photoelectrocatalytic reduction.[68] This is because of the reducing ability of electrons in the counter electrode.

3.3 Device Fabrication and Characterization

Two different devices were designed and fabricated for different experiments. One of them used layer-by-layer (LBL) self-assembly to deposit TiO_2 on a 2 cm×2 cm FTO glass as the photocatalyst electrode. As described in Chapter 2, 1 g of TiO_2 was dissolved in 100 mL of HCl solution with pH=3 to form a stable suspension. Then the cleaned FTO glass was immersed in a solution containing positively charged conductive polymer PDDA to change its surface charge. The FTO glass with a positively charged surface was then alternately immersed in PSS and TiO_2 solutions for 10 minutes each, followed by rinsing with deionized water to remove unbound molecules after each deposition. Photocatalyst electrodes with a different number of PSS/TiO_2 bilayers were prepared by controlling the number of LBL self-assembly cycles. The electrode with the deposited photocatalyst was then placed in a furnace (MTI OTF-1200X-5L) and annealed at different temperatures. The heating rate was 2 °C/min, and the final annealing temperature was maintained for 5 hours.

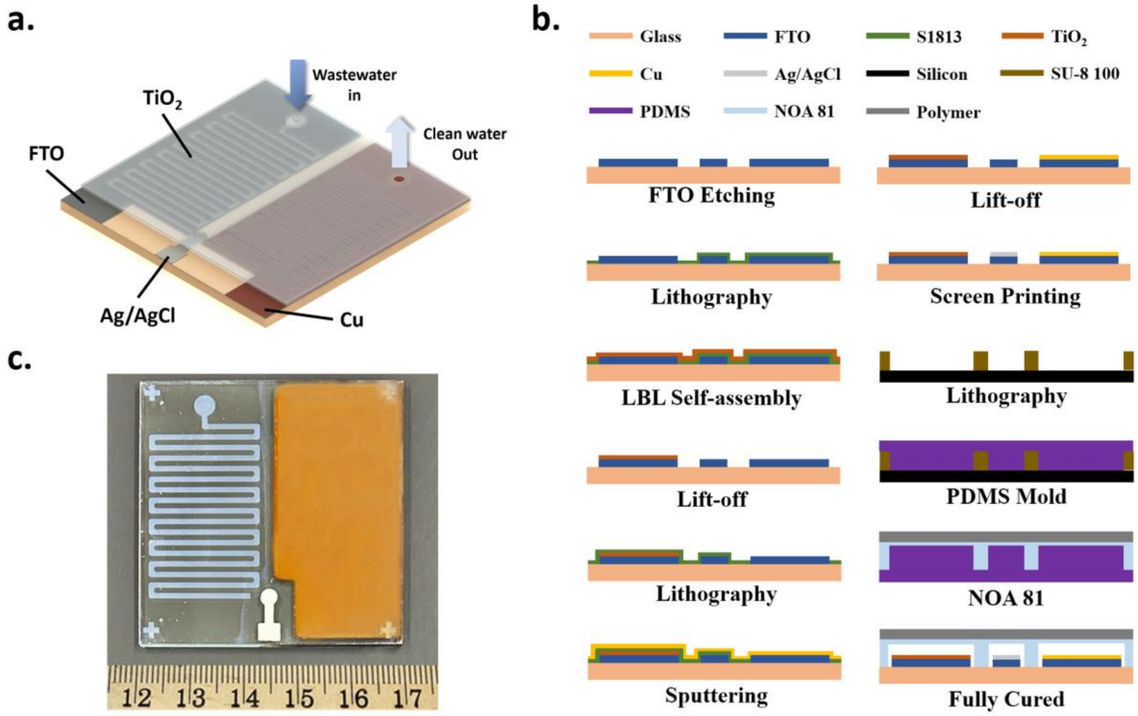

Figure 3.2 (a) Sketch of a microfluidic PEC water purification system heavy; (b) schematic diagram of the fabrication process; (c) Picture of the fabricated chip PEC system without microchannel.

The integrated microfluidic-based PEC system was fabricated on a 5 cm×5 cm FTO glass. The design and fabrication process of the proposed PEC system are illustrated in Figures 3.2a and 3.2b, respectively. Firstly, the FTO glass was etched into the desired shape of the three electrodes using zinc and HCl.[69] The photocatalyst with a microchannel shape was deposited on the photocatalyst electrode using a lift-off method. Initially, a positive photoresist was used to pattern the microchannel shapes on the FTO glass, and TiO_2 was deposited using the LBL self-assembly method as described earlier. The photoresist was then removed by immersing the FTO glass in acetone, followed by annealing in the furnace. The heavy metal ion reduction electrode was deposited with a 100 nm thick copper film by sputtering to enhance the binding strength with the reduced heavy metal. A silver/silver chloride reference electrode was fabricated by screen printing of silver/silver chloride paste on the designed area. Figure 3.2c shows a picture of the fabricated electrodes on FTO glass.

The microchannel was fabricated based on PDMS soft-lithography.[70] The microchannel structure was first patterned on a silicon wafer using negative photoresist SU-8 100 via photolithography with a thickness of 100 µm. Next, a mold made of polydimethylsiloxane (PDMS) was created by pouring PDMS onto the silicon-based mold and curing it. The resulting PDMS mold with mating structures was then used to apply UV-curing glue (NOA81) on top, which was covered with a UV-transparent polystyrene polymer film. After partially curing the glue under UV illumination, the PDMS mold was replaced with the FTO glass, and more UV illumination was applied to fully cure the glue.

The surface morphology of the photocatalyst electrode was observed using a field emission gun scanning electron microscope (FEGSEM) (Hitachi SU8230). A 2.5 nm layer of iridium was deposited on each sample to increase conductivity. The morphology of the deposited TiO_2 was mainly compared before and after annealing. Figures 3.3a and 3.3b show the SEM images of 8 PSS/TiO2 bilayers on a FET glass before annealing with different resolution, while Figures 3.3c and 3.3d show the SEM images of the same sample after 500 ºC annealing. The TiO_2 nanoparticles can be clearly see in the high-resolution image, and the size of the nanoparticles were measured to be about 25 nm. By comparing the SEM images before and after annealing, it can be clearly seen that the pores in the porous structure formed by TiO_2 nanoparticles are reduced after annealing, indicating that the particles become closer to each other. This is due to the decomposition of PDDA and PSS layers and the reorganization of the arrangement of TiO_2 nanoparticles at high temperatures. The benefit of this change is that the binding between TiO_2 and the substrate becomes tighter, and the electron transfer between titanium dioxide nanoparticles and the substrate becomes more pronounced. Therefore, higher photocurrent and more efficient electron transfer can be expected in PEC.

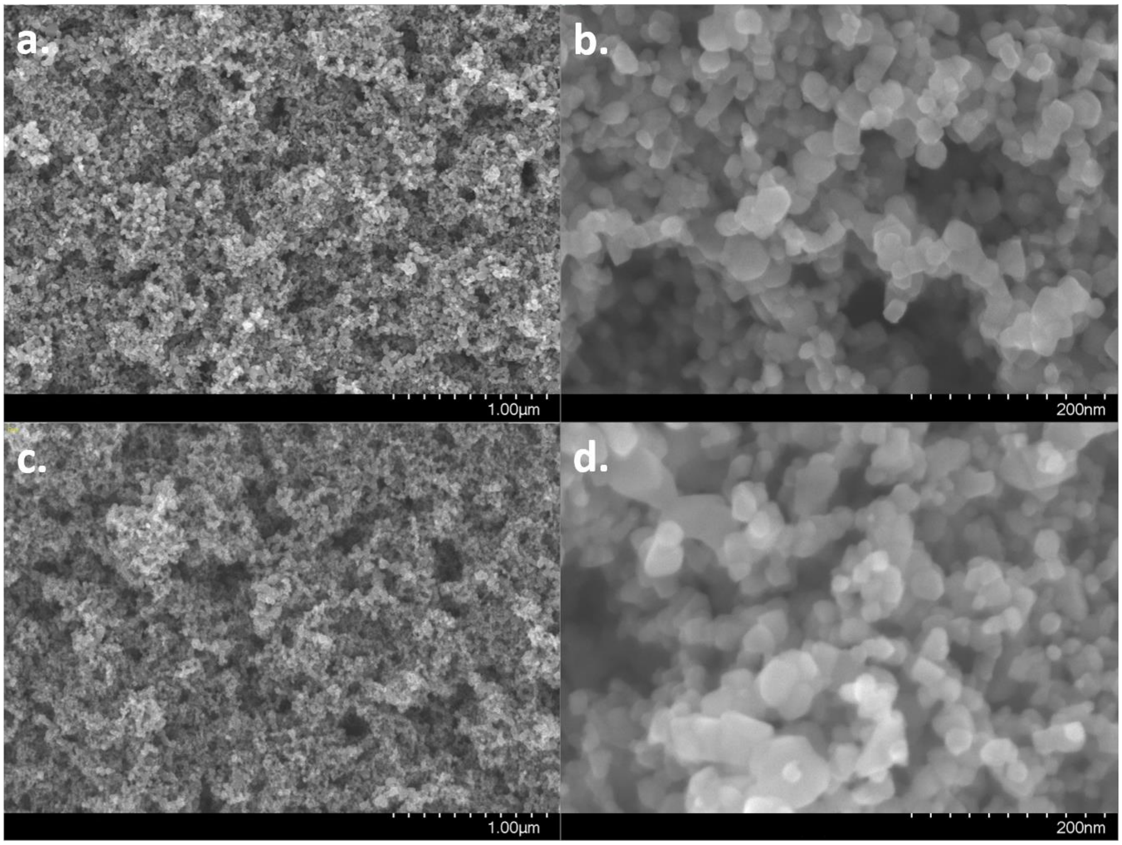

Figure 3.3 SEM images of photocatalyst before and after 500 °C annealing (a) 8 PSS/TiO_2 bilayers on glass substrate before annealing, low resolution; (b) 8 PSS/TiO_2 bilayers on glass substrate before annealing, high resolution; (c) 8 PSS/TiO_2 bilayers on glass substrate after annealing, low resolution; (d) 8 PSS/TiO_2 bilayers on glass substrate after annealing, high resolution.

This consumption can be confirmed by measuring the photocurrent in photoelectrochemistry. Figure 3.4a illustrates the photoelectrochemical response of the photocatalyst electrodes prepared at different annealing temperatures. All the photocatalyst electrodes were coated with 8 PSS/TiO_2 bilayers via LBL self-assembly prior to annealing. The potential difference between the photocatalytic electrode and the reference electrode was maintained at 0 V. The photocatalytic electrodes were first stabilized in the dark for 20 s, then, upon opening the solar light simulator, all the electrodes exhibited photocurrent, which rapidly dropped to the background current upon turning off the light. A comparison shown in figure 3.4b reveals that the photocurrent density increases with increasing annealing temperature. Specifically, the electrode annealed at 500 °C for 5 hours exhibited a photocurrent 82 times higher than that of the non-annealed electrode, reaching 65.7 $\mu A/cm^2$. This improvement can be attributed to the decomposition of PDDA and PSS and the rearrangement of TiO_2 nanoparticles at high temperatures.

The optimization of the number of PSS/ TiO_2 bilayers coated on the photocatalyst electrode via LBL self-assembly was evaluated through photoelectrochemical testing, and the results are presented in Figure 3.4c. As shown in the figure, the photocurrent density increases as the number of PSS/ TiO_2 bilayers increases from 2 to 8. This is attributed to the larger coverage of TiO_2 on the electrode surface, resulting in the generation of more photoexcited electrons. However, when the number of PSS/ TiO_2 bilayers exceeds 8, the photocurrent density tends to saturate and even exhibit a decrease. This phenomenon can be explained by the results shown in Figure 3.4d, which demonstrates the transparency of the prepared photocatalytic electrodes under 365 nm ultraviolet light. It can be observed that a higher number of PSS/ TiO_2 bilayers leads to lower transparency, indicating a significant reduction in the light intensity received by the underlying layers of the photocatalyst. Additionally, the electrons generated by the surface-layer photocatalyst require a longer pathway to reach the FTO surface. Therefore, a decrease in photocurrent density is observed when the number of PSS/ TiO_2 bilayers exceeds 8. Ultimately, 8 PSS/ TiO_2 bilayers were selected as the optimized configuration for the photocatalyst electrode.

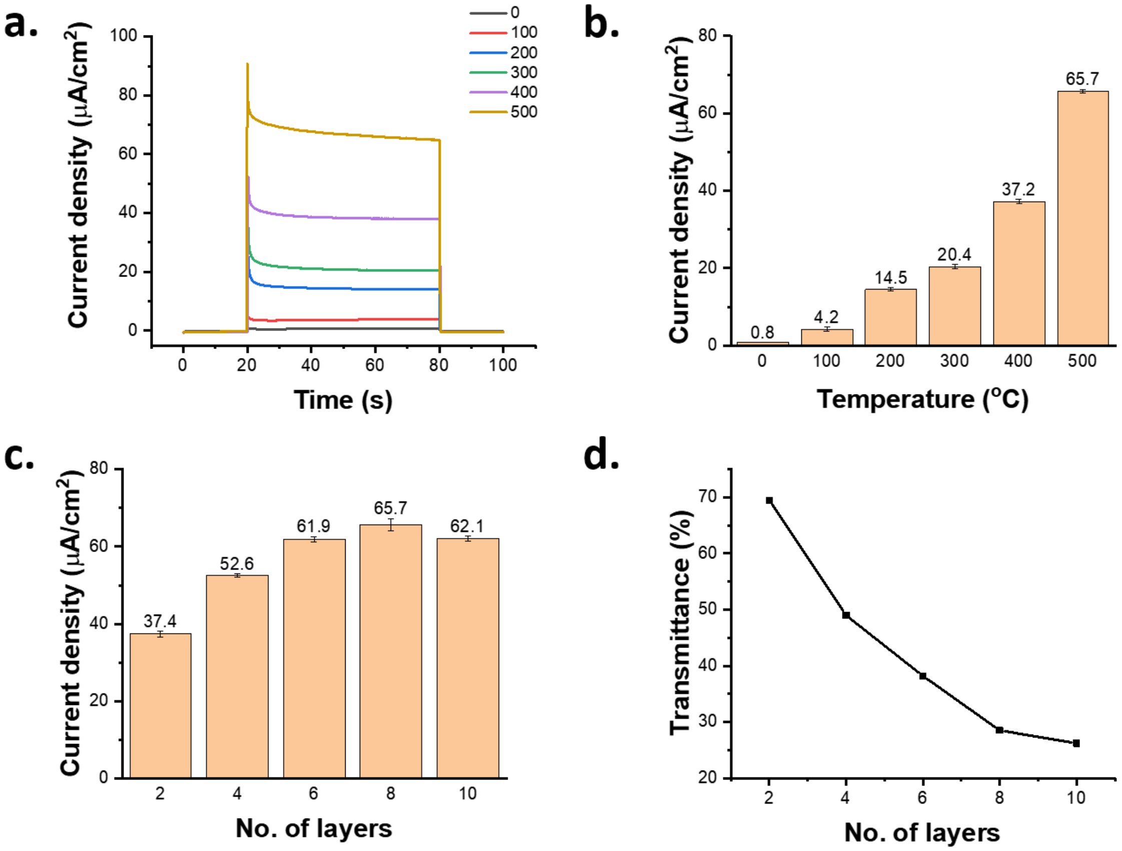

Figure 3.4 (a) Comparison of the photoelectrochemical response of photocatalyst electrodes with different annealing temperatures; (b) Comparison of the photocurrent generated by photocatalyst electrodes with different annealing temperatures; (c) Comparison of the photocurrent generated by photocatalyst electrodes with different number of PSS/TiO_2 bilayers; (d) the transmittance of 365 nm ultraviolet light through photocatalyst electrodes with different amounts of PSS/TiO_2 bilayers.

3.4 PEC Water Purification System with New Configuration

In traditional PEC water treatment systems, the photocatalyst electrode is typically used as the anode to degrade organic pollutants by utilizing photo-generated holes. Other materials electrode serves as the cathode, where the transferred photo-generated electrons are utilized to reduce heavy metal ions. [71, 72] The ultimate purpose of PEC is to separate the photo-generated electron-hole pairs. Therefore, when combining the photocatalyst electrode with the electrochemical three-electrode system, two different configurations emerge. One commonly used configuration, as mentioned earlier in the photoelectrochemical testing, involves using the photocatalyst electrode as the working electrode, where oxidation reactions occur to remove organic pollutants from water. The other electrode (in this work, a graphite rod) is used as the counter electrode, where photo-generated electrons are transferred to undergo reduction reactions, recovering heavy metal ions from the water. The roles of the photocatalyst electrode and carbon rod are reversed in the second configuration, with the graphite rod electrode serving as the working electrode and a negative potential applied between the working electrode and the reference electrode to reduce heavy metal ions. The photocatalyst electrode functions as the counter electrode, still generating oxidation reactions through photo-generated holes. Both configurations enable the transfer of photo-generated electrons from the photocatalyst electrode to the graphite rod electrode. The following experiments compare the differences between the two configurations in terms of organic pollutant degradation and heavy metal ion reduction.

The efficiency of photoelectrocatalytic organic degradation and heavy metal ion reduction in the two PEC systems was evaluated by degrading methylene blue and reducing different types of heavy metal ions. The experimental setup is shown in Figure 3.5. The two sides of an H-type electrochemical cell contained 50 mL of 0.1 M sodium sulfate solutions with 10 μM methylene blue (MB) and 1 ppm of different heavy metal ions, respectively. The two reaction chambers were separated by a proton exchange membrane (Nafion™ 117, Dupont). The 2 cm × 2 cm photocatalyst electrode and an Ag/AgCl reference electrode were placed in the methylene blue solution, while a carbon rod was placed in the heavy metal ion solution. Every 30 minutes, 100 μL of solution was taken out from the tube and the concentration of MB was measured with 664 nm illumination using a UV/visible spectrophotometer (model SP-UV1100, DLAB Scientific Co., Ltd). The concentration of heavy metal ions was measured by Inductively coupled plasma mass spectrometry (ICP-MS).

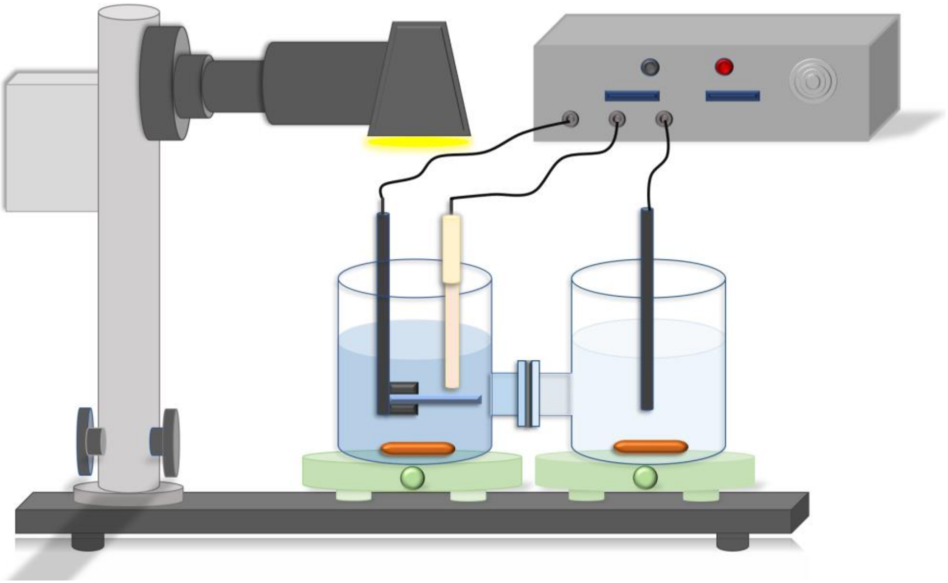

Figure 3.5 Setup of the photoelectrocatalytic water purification tests.

The efficiency of the PEC system for degradation of organic compounds was evaluated through the degradation of MB solution. The MB degradation was tested under different electrode potentials in two configurations. The concentration change is shown in Figures 3.6a and 3.6d. The concentration of MB continuously decreased with increasing illumination time. The lower the concentration of MB, the slower the rate of concentration change, and the photodegradation kinetics of MB can be described by a first-order kinetic equation, and the reaction rate constant k can be used to represent the photodegradation efficiency. Therefore, the slopes in figures 3.6b and 3.6e indicate the photodegradation efficiency corresponding to the two configurations.

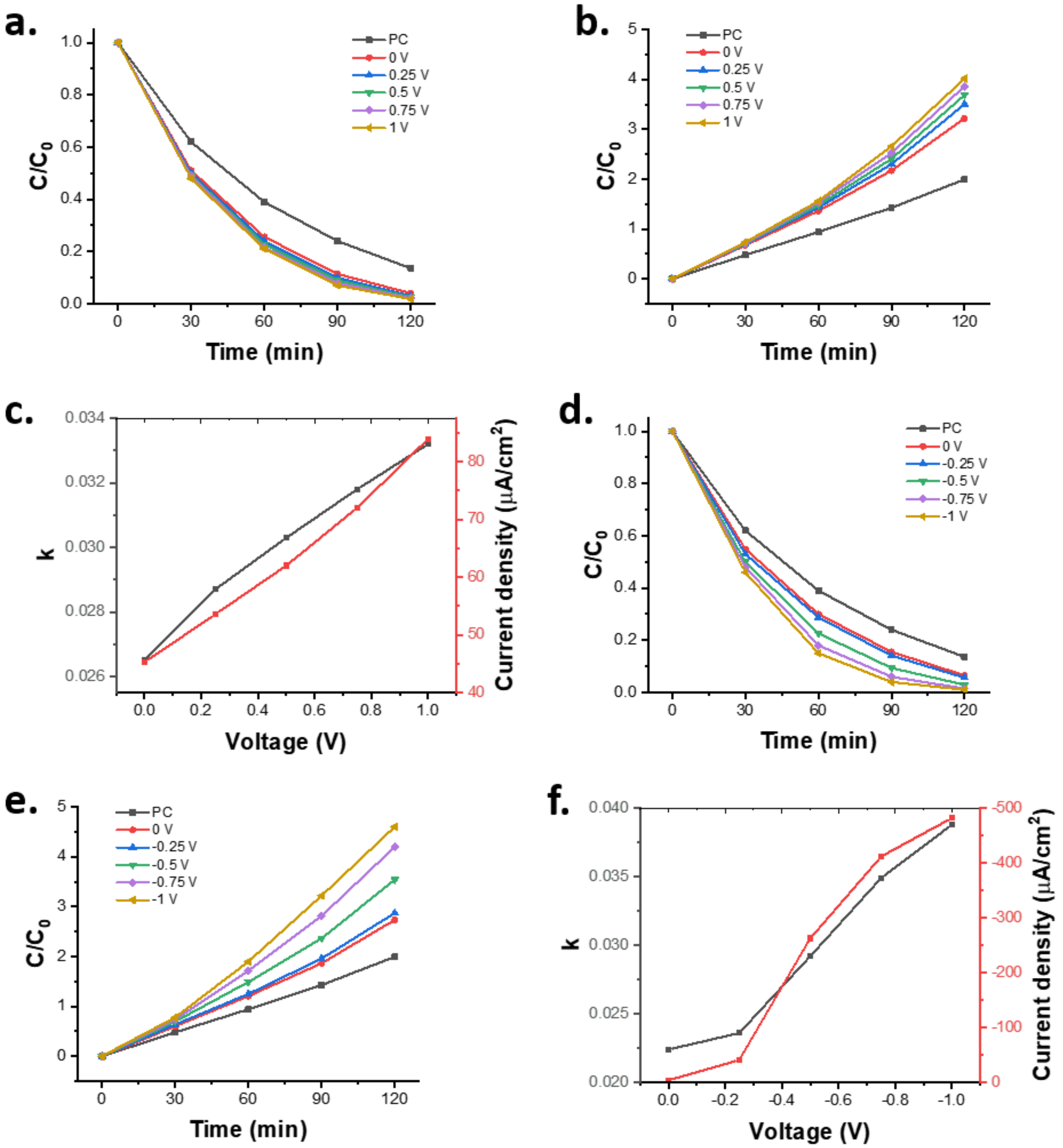

Figure 3.6 (a) Relative MB concentration versus irradiation time with different bias potential in a traditional PEC configuration; (b) MB degradation kinetics for different bias potentials in a traditional PEC configuration; (c) the relationship between the photodegradation constant k, current between electrodes, and bias potential in the conventional configuration of the PEC system; (d) Relative MB concentration versus irradiation time with different bias potential in new PEC configuration; (e) MB degradation kinetics for different bias potential in the new PEC configuration; (f) the relationship between photodegradation constant k, current between electrodes, and bias potential in the new configuration of the PEC system.

Pure photocatalysis without the introduction of the PEC system was used for comparison to demonstrate the enhancement of photodegradation efficiency for organic compound by the two different PEC systems. It can be observed that when the photocatalyst electrode served as the working electrode (Figures 3.6a and 3.6b), the PEC system displayed a twofold increase in photodegradation efficiency compared to pure photocatalysis at a working electrode potential of 1.0 V. When the graphite rod served as the working electrode (Figures 3.6c and 3.6d), the PEC system exhibited a maximum photodegradation efficiency that was 2.3 times that of the pure photocatalysis. It is also noticed that when the photocatalyst electrode served as the working electrode, a significant improvement in photocatalytic degradation efficiency could be achieved even at a relatively low voltage, whereas in the other configuration, the enhancement of photocatalytic efficiency was clearly dependent on the working electrode potential. This is due to the different variations in current magnitude with respect to the working electrode potential in different configurations as shown in Figures 3.6c and 3.6f. When the photocatalyst electrode serves as the working electrode, the current in the system originates from the photocurrent and the redox current at the working electrode. Since the photocurrent is much larger than the redox current and is not affected by the electrode potential, significant current can be generated at low electrode potentials, enabling the efficient separation of photogenerated electron-hole pairs, and leading to a notable improvement in photocatalytic degradation efficiency. On the other hand, when the graphite rod serves as the working electrode, the current in the PEC system is determined solely by the heavy metal ions reduction current of on the graphite rod electrode. This current magnitude is dependent on the electrode potential. When the electrode potential becomes more negative (larger in absolute value), the reduction reaction on the electrode becomes more vigorous, resulting in a larger current. When the consumption rate of electrons on the working electrode is lower than the rate of photogenerated electron production on the photocatalyst electrode, only a partial separation of photogenerated electron-hole pairs occurs, leading to a smaller improvement in photocatalytic degradation efficiency. However, when the potential on the working electrode becomes negative enough to generate an electron consumption rate exceeding the number of photogenerated electrons, the counter electrode potential rapidly increases to facilitate additional electrochemical degradation of organic compounds, generating sufficient electrons. Therefore, a higher enhancement in photocatalytic degradation rate can be observed compared to the previous configuration.

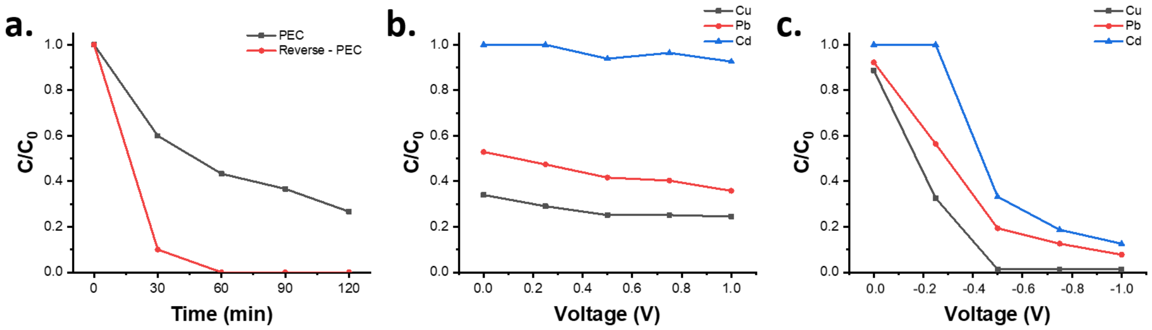

Figure 3.7 (a) Relative Cu^{2+} concentration versus irradiation time with different PEC configurations; (b) relative heavy metal ions (Cu^{2+}, Pb^{2+}, Cd^{2+}) concentrations after 2 hours deduction in PEC with the traditional configuration under different applied voltages; (c) relative heavy metal ions (Cu^{2+}, Pb^{2+}, Cd^{2+}) concentrations after 2 hours deduction in PEC with the new configuration under different applied voltages.

The two different configurations of the PEC system exhibit more significant differences in the reduction of heavy metal ions. Figure 3.7a records the reduction of copper ions (Cu^{2+}) in the two PEC system configurations when the absolute value of the working electrode potential is 1.0 V. It can be observed that in the new PEC system with the graphite rod as the working electrode, the concentration of Cu^{2+} rapidly decreases and is completely recovered within one hour. In contrast, when the photocatalyst electrode serves as the working electrode, only 72% of Cu^{2+} is recovered within 2 hours. This phenomenon can also be explained by the current changes in Figures 3.6c and 3.6f. When the absolute value of the working electrode potential is 1.0 V, the current density in the new PEC system with the graphite rod as the working electrode is much higher than the current density when the photocatalyst electrode serves as the working electrode, and a higher current density implies a faster reduction of heavy metal ions.

The reduction effects of different heavy metal ions were compared in two different configurations of the PEC system. In addition to Cu^{2+}, the reduction of lead (Pb^{2+}) and cadmium (Cd^{2+}) ions were tested. Figures 3.7b and 3.7c show the concentrations of heavy metal ions in the solution after 2 hours of operation of the PEC systems. It can be observed that the traditional configuration of the PEC system cannot reduce Cd^{2+}, and its reduction efficiency for Cu^{2+} and Pb^{2+} is also low, with no significant changes observed with increasing electrode potential. This is because the number of photo-generated electrons is limited, and the absolute value of the photo-generated electron potential is much lower than the redox potential of Cd^{2+}. In the new configured PEC system, reduction of all three heavy metal ions can be observed, and the efficiency of heavy metal ion reduction increases with more negative electrode potential. More importantly, reduction of Cd^{2+} can be observed when the working electrode potential is lower than the redox potential of Cd^{2+}, which cannot be achieved with the traditional configuration of the PEC system.

3.5 PEC Microfluidic Water Purification System

Finally, the proposed PEC configuration was integrated with a microfluidic system to form a miniaturized, on-chip, efficient PEC water treatment system. The proposed new PEC configuration was implemented during testing, where the photocatalyst electrode served as the counter electrode and the Cu electrode served as the working electrode. A mixed solution containing the organic compound MB and inorganic heavy metal ions was passed through the microchannel at flow rates of 5 mL/h, 7.5 mL/h, and 10 mL/h, respectively. The concentrations of MB and heavy metal ions at the outlet were collected and measured. To prevent the reduction reaction of MB during its passage through the working electrode from affecting the assessment of photocatalytic degradation efficiency, the obtained solution was stirred overnight under magnetic stirring, allowing the reduced MB to be oxidized by oxygen in the air and regenerating MB.

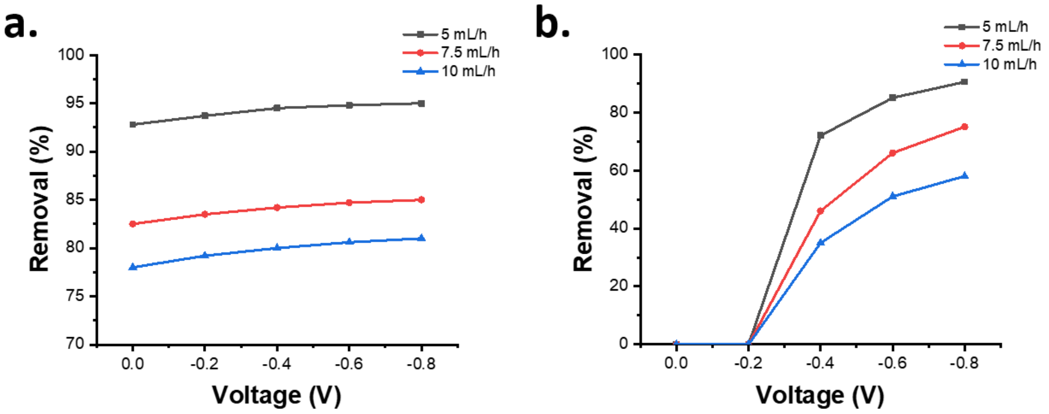

Figure 3.8 The performance of microfluidic PEC system with different mass flow rates under different applied potentials on (a) MB removal and (b) heavy metal ion removal (Cd^{2+}).

Figure 3.8a illustrates the efficiency of the microfluidic photoelectrochemical (PEC) system in degrading the organic compound MB at different flow rates when the potential of the working electrode decreases from 0 V to -0.8 V. The results indicate an inverse relationship between the removal rate of MB and flow rate. This phenomenon can be attributed to the shorter residence time of the solution in the microchannel at higher flow rates, leading to a shorter duration of the degradation reaction. Additionally, it is noticed that as the potential of the working electrode decreases, the removal rate of the organic compound increases. This can be explained by the acceleration of the reduction reaction on the working electrode at lower potentials, which enhances the electron transfer rate and facilitates efficient charge separation of photogenerated electrons and holes. Similarly, Figure 3.8b demonstrates the efficiency of the microfluidic PEC system in recovering heavy metal ions. The effect of the flow rate on the reduction efficiency is similar to that of organic compound degradation. However, it is noticed that working electrode potential has a more significant influence on the efficiency of heavy metal ion recovery. Potentials higher than -0.2 V are insufficient for the reduction of Cd^{2+}, whereas a decrease in potential below -0.4 V leads to a rapid increase in recovery efficiency. In summary, when the potential of the working electrode is set at -0.8 V, the system achieves over 95% degradation of 10 μM MB solution and over 90% degradation of a Cd^{2+} ion solution with a concentration of 1 ppm at a flow rate of 5 mL/h.

3.6 Conclusion

This study presents a comprehensive investigation into the enhancement of water treatment efficiency through photoelectrocatalysis (PEC) compared to photocatalysis. In addition to the existing PEC water treatment configurations, new PEC system configurations are proposed, enabling the simultaneous removal of organic compounds and most heavy metal ions. By comparing the efficiency of the two PEC system configurations in terms of organic compound degradation and heavy metal ion recovery, both configurations demonstrate improvements in photocatalytic degradation rates. Notably, the proposed new configuration achieves a 2.3 -fold enhancement in the degradation rate of organic compounds at a voltage of -1.0 V. Both configurations exhibit the recovery of Cu^{2+} and Pb^{2+} ions, but the proposed new configuration exhibits significantly higher recovery efficiency and is the only one capable of recovering Cd^{2+} ions. Finally, a demonstration using a small-scale microfluidic PEC water treatment system prototype achieves 95% organic compound degradation and over 90% heavy metal ions recovery, providing a theoretical analysis and model validation for the development of large-scale array-based high-efficiency PEC water treatment platforms.

Chapter 4: Microluidic Diode and Application to Valveless Micropumps

4.1 Introduction

Micropumps are microelectromechanical system (MEMS) devices that pump small quantities (nanoliters or microliters) of liquid. They have been widely used in thermal control of electronics, measurement of volumes in the micro-scale, mixing of microfluidic streams, and medical applications. [73, 74, 75] For example, the piezoelectric actuation based valveless micropump has proved to be useful for drug delivery,[76] and its application as an actuator for dynamic cultures on ‘organs on a chip’ has gained recent attention.[77, 78] Passive fluid diodes with no mechanical moving parts are used in valveless micropumps. They have attracted great interest due to their simple structures, compact sizes, lack of electromagnetic interferences, and easy integration.[79] The working mechanism of the valveless micropump is based on the difference of flow resistances between forward flow and back flow through internal channels.[80]

Two commonly used valveless micropumps are based on either nozzle-diffuser channels or Tesla-type diodes. The nozzle-diffuser valveless micropump uses V-shaped channels that behave like nozzles when the flow is in one direction and like diffusers when the flow is in the opposite direction.[81, 82, 83] Chandrasekaran and Packirisamy studied the flow behavior of a nozzle-diffuser type valveless micropump with geometrical tuning using finite element modeling.[84] They proposed a method to design the best diffuser geometries using different diffuser angles. Yang and his group considered increasing the micropump flow rate by adding two-fin, or obstacle, structures into the nozzle-diffuser design.[85] However, the increased flow resistance offset the potential improvement. The Tesla-type valveless micropump gained interest after 1999 because of its high diodicity. Researchers considered different structures of the Tesla valve flow-directing element.[86, 87, 88] The diodes are complex channels (to be introduced below) that offer different flow losses for the two flow directions. Derakhshan et al. simulated flow behavior of the Tesla-type valveless micropump and optimized the dimensions of the diode to achieve higher diodicity and flow rate.[89] Kolahdouz suggested that the two-stage Tesla valve is the optimized design for a piezoelectric-driven micropump.[90] Most of the published work is focused on dimension or shape optimization of existing flow-directing elements.[91, 92] Since the fundamental structures are not changed, performance improvement was limited.

Topology optimization is a systematic approach to optimize the layout of valve internal elements using a computational procedure for a given set of boundary conditions and constraints.[93] It has been successfully used to solve fluid-based problems, especially in the design of fluidic diodes with high diodicity[94]. Lin et al. used this method to optimize the Tesla-type valve and obtained fluidic diodes with a diodicity of up to 8.87.[95] Sato and his group proposed a bi-objective topology optimization method and designed a fluidic diode with lower pressure drop for the forward flow and higher pressure drop for the backward flow.[96] The published fluidic diodes were mainly used as fluidic resistance valves, and their application to valveless pumps was barely discussed.[97] Moreover, the scales of these published fluidic diodes were large relative to MEMS devices, further preventing application to micropumps.[98]

This work seeks to investigate a microscale fluidic diode of high diodicity that can be used in valveless micropumps to achieve higher mass flow rate by using topology optimization and computational fluid dynamic (CFD) methods. MEMS technology is used to fabricate the fluidic diode-based valveless micropumps.

4.2 Body of Knowledge

There are three types of microvalve structures in common use: micropumps, including active valve,[99] passive check valves,[100] and valveless structures.[101] Active valves with actuators feature easier flow controllability over a wide range of operating conditions, while always having larger sizes and additional power consumption. The passive check valves do not need additional supply power, but the controllability is also reduced. In addition, both active and passive valves in clog, wear and fatigue which prevents their usage in water purification systems.[102]

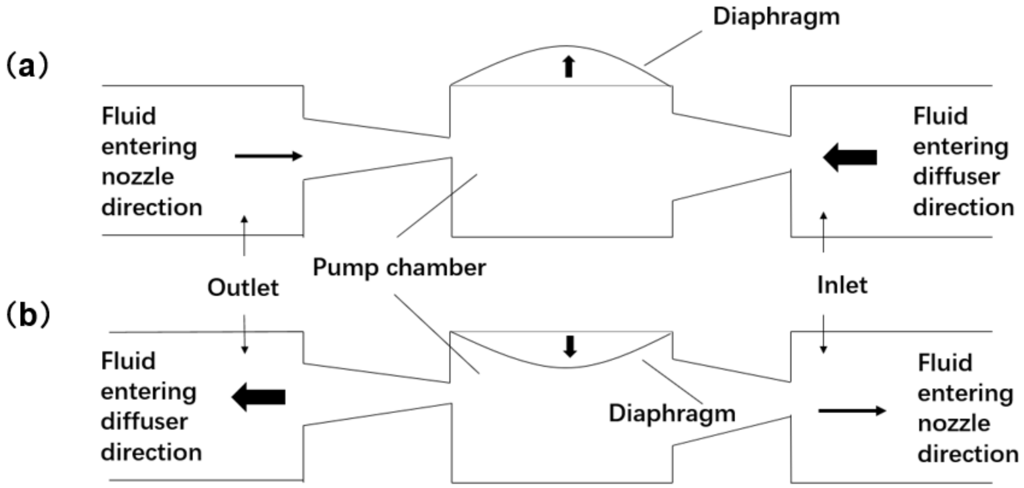

Figure 4.1 Working mechanism of the valveless pump in (a) supply mode and (b) pump mode.

As shown in Figure 4.1, the valveless pump consists of two diffuser elements connected to a pump chamber having an oscillating diaphragm which is fabricated of piezoelectric ceramics in this design. The nozzle/diffuser structures are used as flow directing elements. The working mechanism of the valveless pump is shown in Figure 4.1.

As there are no moving parts encountered with the nozzle/diffuser elements, the risk of clogging is drastically reduced. The mass flow rate of the pump can be controlled easily by changing the amplitude or frequency of the actuated electric field.

Besides the advantages mentioned above for micropumps, a valveless pump may also be helpful to enhance mass transfer in the reaction chamber because of the special oscillatory flow movement mode. As shown in Figure 4.1, the solution enters or leaves the reaction chamber in a manner that flows forward and backward. This reciprocating motion may lead to extra movement between the reaction chamber and bulk fluid, and thereby the mass transfer might be enhanced by additional convection.

4.3 Topology Optimization

The two-dimensional fluidic diode was first obtained using topology optimization based on the Density Model with Darcy interpolation. In short, the Navier-Stokes equations for forward and backward flows were solved. The ratio of pressure drop between the inlet and outlet for backward flow and forward flow was calculated as diodicity. To achieve high diodicity, the ratio of energy dissipation between backward and forward flow was set as the objective function for topological optimization.[103] A relatively low Reynold number of 100 was used for the calculation. The scale of a fluidic diode is primarily defined by the width of the inlet chamber to the diffuser. The different widths of the outlet and sizes of the computational domains were used to obtain fluidic diodes of different geometries. The diodicity of each fluidic diode was calculated to evaluate its performance.

Commercial software COMSOL Multiphysics was used to solve the topology optimization for 2D structures, and CFD simulation was conducted for 2D and 3D structures by ANSYS Fluent.

Figures 4.2a and 4.2b show the computational domain before and after topology optimization. The size of the inlet and outlet, and the length and width of the rectangular computational domain were optimized for high diodicity. The resulting geometry with the highest diodicity is shown in Figure 4.2b using the Tesla type diode as an example. The through-flow velocity contours for forward and backward flows through the fluidic diode are shown in Figures 4.2c and 4.2d. The backward flow is divided into several tributaries which then interact with one another at their confluence, leading to more resistance in the backward flow than in the forward flow. The diodicity of the fluidic diode is calculated by the ratio of backward flow pressure drop to forward flow pressure drop, resulting in a diodicity of 5.31 in this work.

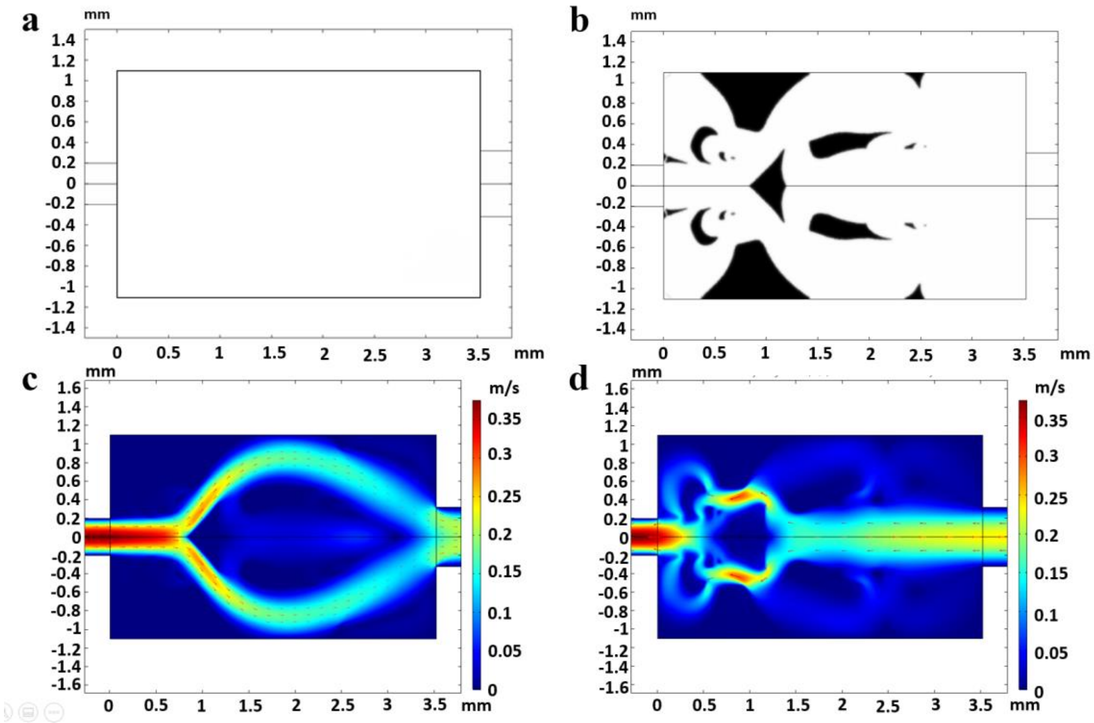

Figure 4.2 (a) Computational domain for topology optimization; (b) fluidic diode geometry after topology optimization; (c) velocity contours of forward flow through the fluidic diode; (d) velocity contours of backward flow through the fluidic diode.

Figure 4.3a shows the optimized diodicity of fluidic diodes of different inlet sizes. The highest diodicity appears with an inlet size of 400 µm. The diodicity of smaller fluidic diodes is limited by the feature sizes, which is limited by device fabrication, while the diodicity of larger fluidic diodes is limited by the degrees of freedom during the optimization calculation. Too many elements lead to excessive degrees of freedoms and failure of convergence. Figure 4.3b shows the corresponding forward pressure difference of fluidic diodes of different channel inlet sizes. The smaller pressure difference means smaller flow resistance and lower power needed to drive the pump. As the size of fluidic diode increases, the pressure difference first decreases, then tends to level off. The fluidic diode with an inlet chamber size of 400 µm was selected for further simulation.

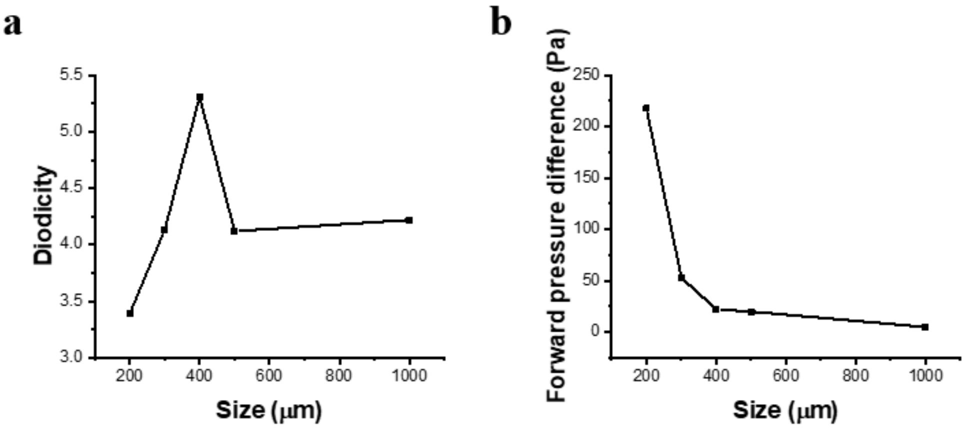

Figure 4.3 (a) Diodicity of Tesla-type fluidic diodes of different sizes; (b) pressure differences of fluidic diodes of different sizes.

Topology optimization was performed on a two-dimensional (infinite depth) geometry, which allows viscous forces on the side walls to be neglected. However, the height of the actual microchannel is limited and is always comparable to the other two dimensions. Thus, it is important to consider the effect of thickness on the performance of the designed fluidic diode. To address this, a three-dimensional analysis was performed by CFD simulation. When converting the simulation of the fluidic diode from two-dimensions to three, the mass flow rate of 0.1 g/s was used for calculation and depths ranging from 100 µm to 500 µm were studied. Figure 4.4 shows the velocities, Reynolds numbers, pressure differences, and diodicities of fluidic diodes of various thicknesses. The results show that larger thickness leads to smaller velocities and Reynolds numbers due to the fixed mass flow rate. The diodicity is reduced with thickness because of the smaller associated inertial forces. On the other hand, the effects of viscous forces are more significant when the thickness is less, leading to higher pressure differences, but lower diodicities. The simulation was conducted for a valveless micropump using a microchannel 200 µm deep.

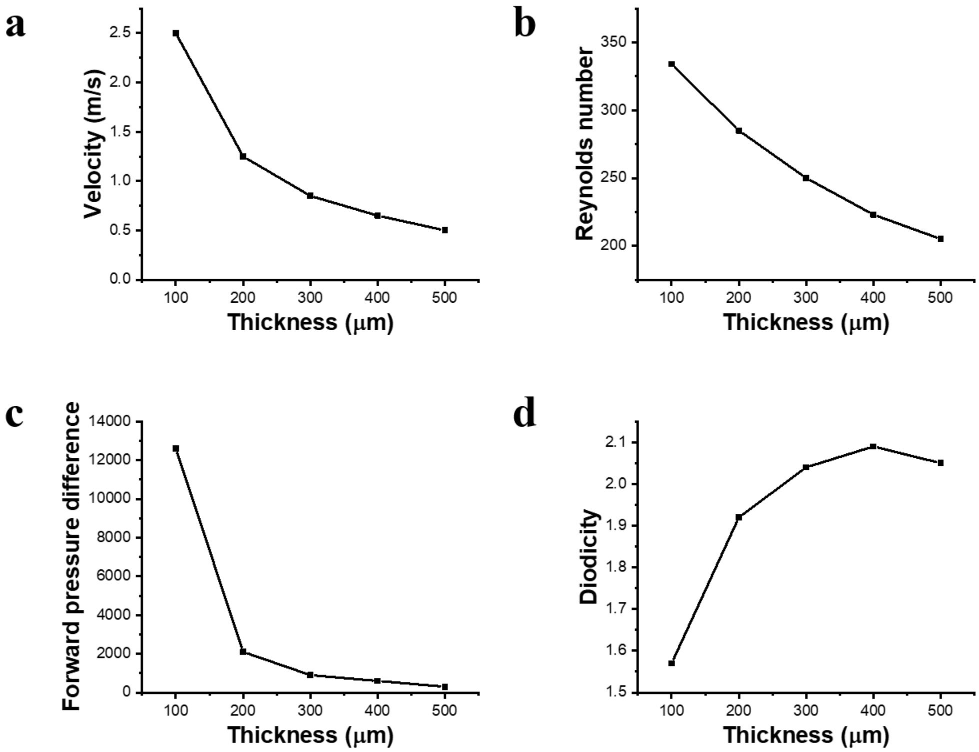

Figure 4.4 The effects of thickness on (a) velocity, (b) Reynolds number, (c) pressure difference, and (d) diodicity of the Tesla-type designed fluidic diode.

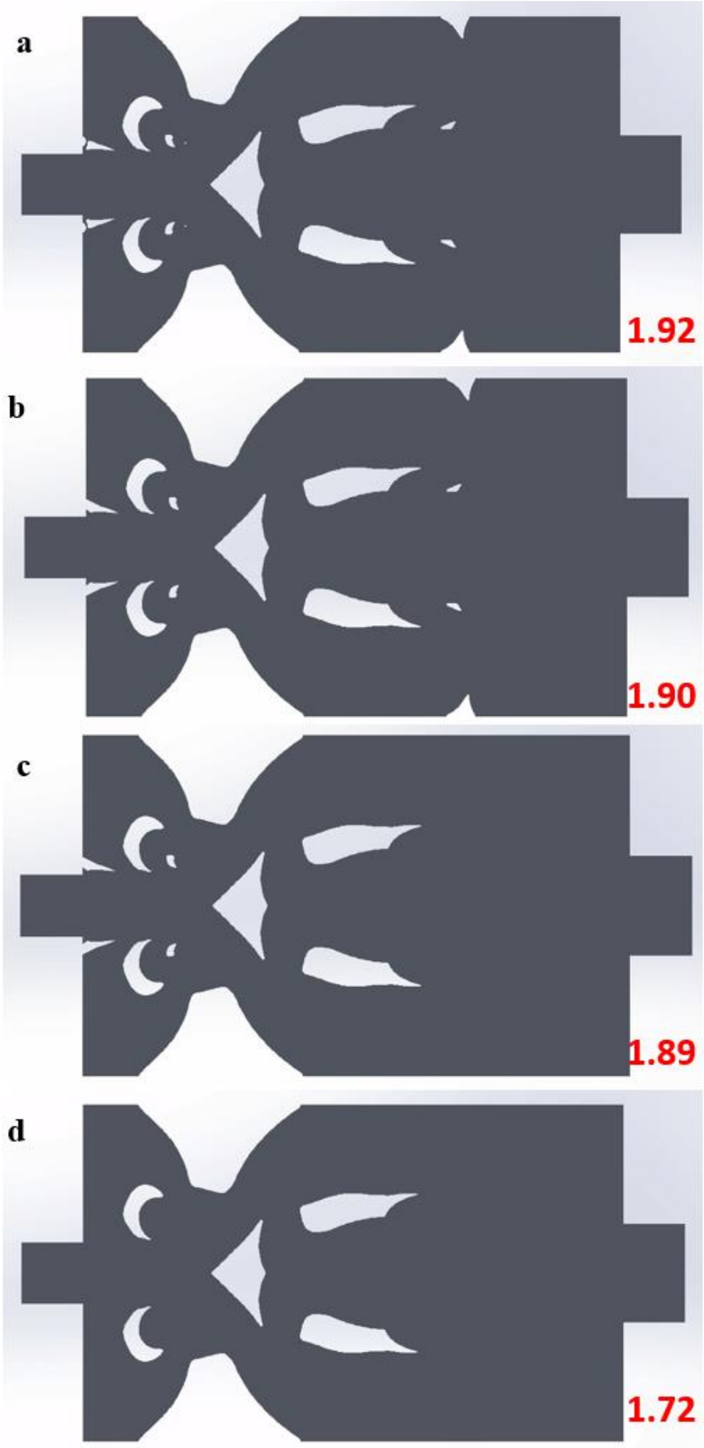

Figure 4.5 Structure and diodicity of (a) original Tesla-type fluidic diode; (b) fluidic diode with small structure removed; (c) fluidic diode with unnecessary structure removed; (d) fluidic diode with critical structure removed.

Before the simulation of the Tesla-type valveless micropump with the chosen fluidic diode, the structure of the fluidic diode was simplified for lower complexity and easier fabrication. Figure 4.5a shows the structure and diodicity of the original design. As shown in Figure 4.5b, all structures smaller than 20 μm were removed to avoid fabrication of high-aspect-ratio features, and the diodicity was reduced from 1.92 to 1.90. Small structures with little effect on diodicity were also removed, resulting in a diodicity of 1.89 (Figure 4.5c). Any further simplification (as in Figure 4.5d) lead to significant reductions of diodicity. Therefore, the structure in Figure 4.5c was employed in the valveless micropump with Tesla-type fluid diodes.

Simulation of valveless micropumps was conducted by CFD. The geometry used for simulation is shown in Figure 4.6a. The two fluidic diodes are connected by an actuator chamber attached to a PZT actuator and the other ends are connected to the inlet and outlet chambers. The thickness of fluidic diode and actuator chamber was set as 200 μm. The fluid parameters were set according to water at room temperature. The transient laminar flow model with the SIMPLE pressure treatment algorithm and second-order upwind interpolation was used for the simulation.

The diameter of the chamber having the attached PZT actuator was 10 mm. The amplitude of oscillation of the center of the actuator was set as 5 μm, matching optimum experimental results. The changes in displacement over time follows a sinusoidal wave function. The deflection profile of the PZT actuator can be divided into two sections: the inner section, with piezoelectric ceramics, and the outer section, with brass (see Figure 4.6a). When a sinusoidal excitation voltage is applied to the PZT disc, the piezoelectric ceramic section vibrates. The brass section also vibrates. The deflection of these two sections can be described by the following equations:[104]

$$d_1(r) = d_{max}[1+(b^2r^2 - a^2r^2)/(2a^2b^2 ln(a/b))]sin(2\pi ft),$$

$$(0 \leq r \leq a)$$

$$d_2(r) = d_{max}[(b^2+2b^2 ln(r/b)-r^2)/(2b^2 ln(a/b))]sin(2\pi ft),$$

$$(a \leq r \leq b)$$

where the d_1 and d_2 are the deflections of the inner and outer sections, respectively; d_{max} is the amplitude of the membrane center, which is set as 5 µm; a is the radius of the inner section, which is 3.75 mm; b is the diameter of outer section, which is 5 mm; f is the excitation frequency, which is 200 Hz.

Dynamic meshing with a User Defined Function (UDF) was applied to describe the movement of the piezoelectric actuator. The pressures of the inlet and outlet surfaces were set to zero and the mass flow rates at the inlet and outlet surfaces were monitored. A mesh sensitivity study was performed first to verify that the results were independent of mesh quantity, and a mesh with 4.2 million nodes was chosen for the simulations. Each cycle was divided into 100 time-steps, leading to a time step size of 50 µs.

The mass flow rate through the micropump with the fluidic diodes in the inlet and outlet passages was calculated, as shown in Figure 4.6b. The positive mass flow means water flow into the micropump, while the negative mass flow means the water flow out of the micropump. It can be found from the figure that when the water is pumping out, the outlet has a higher mass flow rate, and the inlet has a higher mass flow rate when the water is pumping in. The mass flow rate difference between inlet and outlet, integrated over time, leads to the net mass flow rate of the micropump. The net mass flow rate of 31.3 mL/h was calculated as the cycle average.

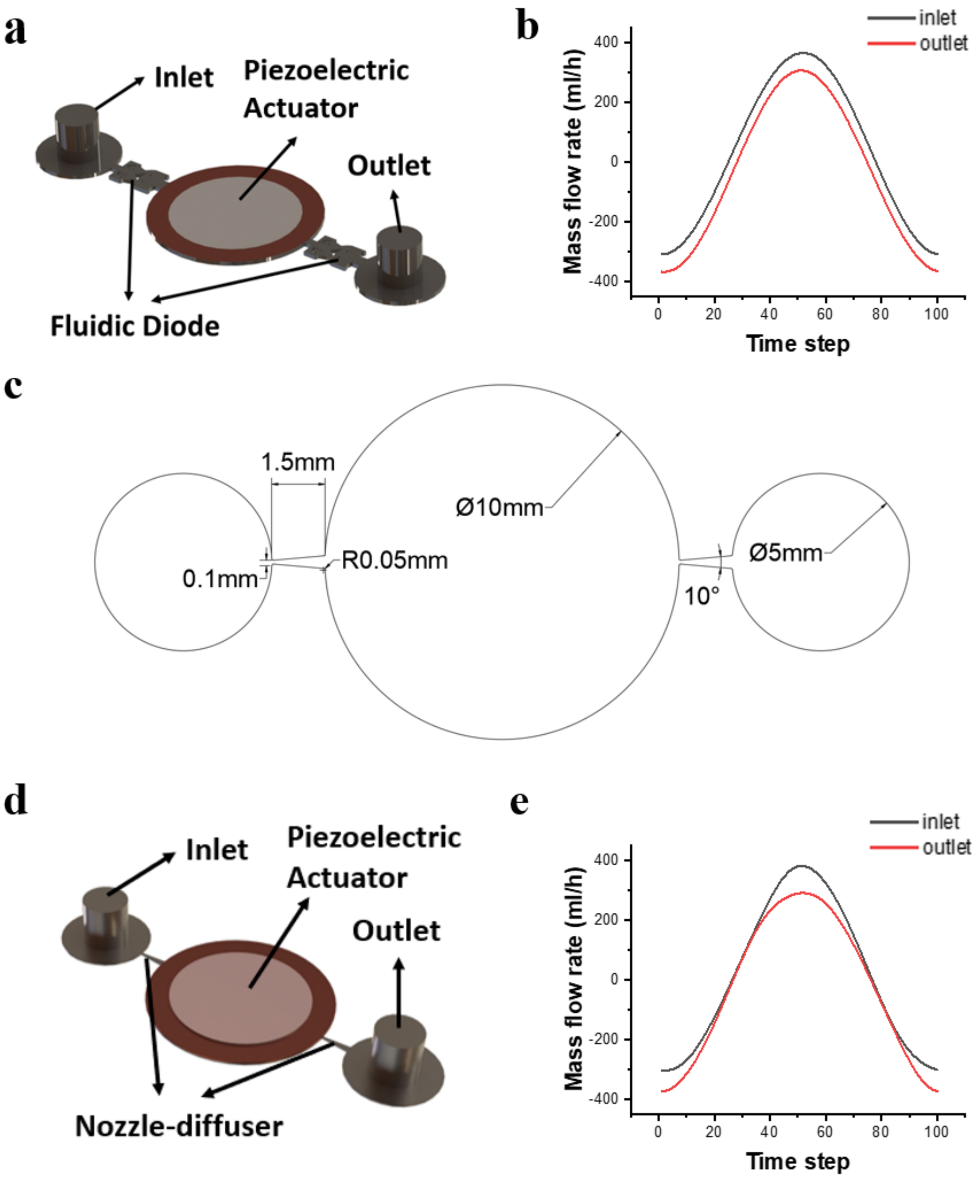

Figure 4.6 (a) A schematic of the Tesla-type valveless micropump; (b) a plot of the mass flow rate for the Tesla-type valveless micropump ; (c) critical parameters for the nozzle-diffuser type valveless micropump; (d) a schematic of the nozzle-diffuser type valveless micropump; (e) a plot of the mass flow rate for the nozzle-diffuser valveless micropump.

The same simulation as that for the Tesla type valveless micropump was performed on the nozzle-diffuser type valveless micropump. The critical parameters of the nozzle-diffuser are shown in Figure 4.6c, obtained from work done by He et al.[105] The other parameters are the same as those of the Tesla-type fluidic diode-based valveless micropump. Figure 6d shows the structure of the micropumps used for the simulation.

The mass flow rate of the nozzle-diffuser type valveless micropump was calculated based on the inlet and outlet mass flow rate difference, as shown in Fig. 6e. The simulated mass flow rate was 20.6 mL/h, 34.2% lower than with the Tesla-type fluidic diode-based valveless micropump. Comparing Figure 4.6b and 4.6e shows that both micropumps have high diodicity at high flow velocity while the Tesla-type fluidic diode-based valveless micropump has better performance at lower flow rates. This is consistent with the high diodicity of the Tesla-type fluidic diode under low Reynolds number conditions.

4.4 Fabrication and Evaluation

MEMS technology was used to fabricate the valveless micropump with the topologically optimized Tesla-type fluidic diodes and with the conventional nozzle-diffuser diode to fabricate valveless micropumps for comparison. To capitalize upon repeated use of molds and low-cost processing technology, micropumps with a sandwich structure of two polymer films and an intermediate structural layer were designed and fabricated.[106]

The fabrication process is shown in Figure 4.7a. Lithography with negative photoresist SU8-100 was first performed on a silicon wafer. The thickness of the photoresist ranged from 150 µm to 250 µm, depending on the rotational speed of the spin coating process. Polydimethylsiloxane (PDMS) was then poured on a silicon-based mold and cured to obtain a soft mold with mating structures. Then UV-curing glue, NOA61, was applied on the PDMS mold and covered with a UV-transparent polymer film. The NOA61 was partially cured under UV illumination, followed by replacement of the PDMS mold with another polymer sheet. More UV illumination was then applied to fully cure the NOA61. Finally, a piezoelectric (PZT) disc was attached to a polymer film to serve as the actuator. Figure 4.7b shows details of the critical structures of the fabricated fluidic diode based valveless micropump based on the Tesla diode.

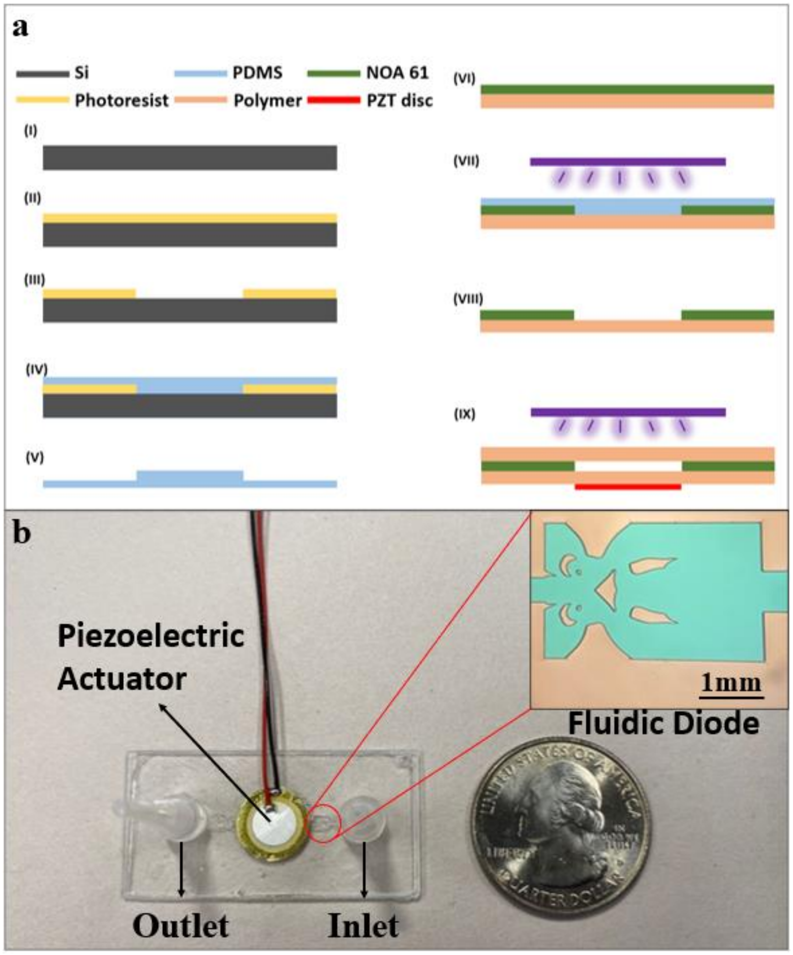

Figure 4.7 (a) Schematic diagram of the fabrication process; (b) picture of the valveless micropump with the designed Tesla-type fluidic diode and a microscope image of the detailed structure.

Characterization mainly includes measuring the amplitude of the PZT actuator (Figure 4.7b), the flow rate of the micropump, and the pressure difference under operation. A function generator and a linear piezoelectric amplifier was used as the excitation source of the PZT actuator. A voltage of up to 100 V was applied to the PZT disc. The amplitude of the PZT actuator movement was measured by a laser vibrometer. The inlet and outlet of the micropump were connected to tubes of known diameters. The mass flow rate was calculated by placing the inlet and outlet tubes horizontally at the same level and measuring the displacement of the liquid meniscus in the tube within a specific period. In the pressure difference test, the inlet and outlet tubes were placed vertically, and the pressure difference was determined by measuring the liquid level difference.

Figure 4.8a shows the measured mass flow rates of the Tesla-type diode micropump operating under different excitation voltages. As discussed previously, there is no inlet-to-outlet pressure difference for this flow measurement. As shown, the mass flow rates increase as the excitation voltage increases. The reason can be found in Figure 4.8b, showing the maximum displacement of the center of the PZT actuator under different excitation voltages. Higher excitation voltages lead to larger displacements of the PZT actuator, resulting in increased mass flow rates. This micropump of 200 µm thickness has a higher mass flow rate than those of 150 µm and 250 µm thicknesses. This suggests that the inertial and viscous forces reach a balance under an optimum thickness of 200 µm, producing the highest diodicity and mass flow rate. The different flow rates when the inlet-to-outlet pressure difference is zero, different maximum displacement of the PZT actuator, and different pressure differences when flow rate is zero are shown in Figures 4.8a, 4.8b, and 4.8c, respectively, each for three different valve thicknesses. The highest mass flow rate achieved is 33.5 mL/h. The difference between simulation results and experimental data is about 7%, lending credibility to the results from the CFD simulation.

Three nozzle-diffuser type valveless micropumps with different thicknesses were fabricated for comparison. The mass flow rates of the nozzle-diffuser type valveless micropumps of different thickness were also measured, as shown in Figure 4.8c. As with the Tesla-type fluidic diode-based micropumps, the mass flow rate increases with excitation voltage and the micropump the 200 μm thick has the highest mass flow rate, compared to the pumps of other thicknesses. The highest mass flow rate achieved by the nozzle-diffuser type valveless micropumps is 14.9 mL/h, 44% of the valveless micropump with the Tesla-type designed fluidic diodes. A comparison of the experimental results with the simulation results shown in Figure 4.6e indicates that the computational calculation is a 38% overestimation. The gap between measurements and computation is mainly due to the lower displacement of the actuator in real testing. The vibration amplitude of the actuator for the nozzle-diffuser and Tesla type fluidic diode valveless pumps was set to be the same in the CFD simulations. However, the nozzle-diffuser has a higher forward pressure difference than the Tesla type fluidic diode, therefore the PZT actuator cannot achieve the same amplitude of vibration as that of diode-based micropumps when the same voltage is applied.

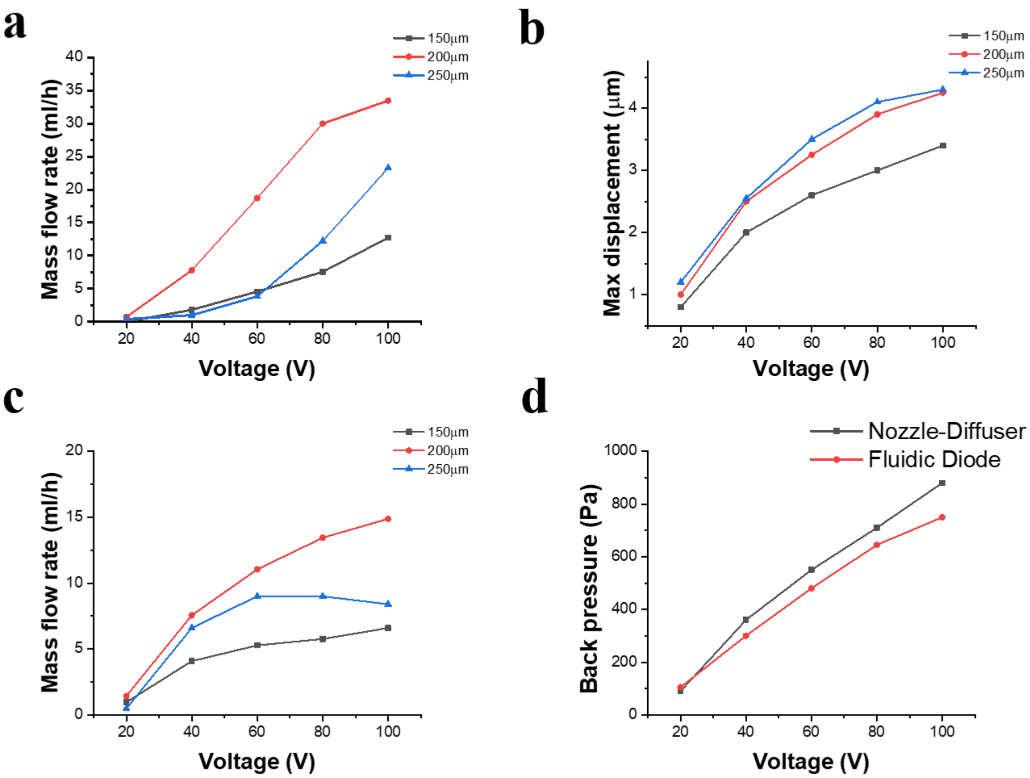

Figure 4.8 (a) Mass flow rate of the fluidic diode-based valveless micropump for various thicknesses; (b) the maximum displacements of the center of the PZT actuator for the fluidic diode-based valveless micropump of various thickness; (c) the mass flow rate of the nozzle-diffuser type valveless micropump in various thicknesses; (d) back pressure of the two different types of valveless micropumps with 200 µm thick.

The pressure differences of the two different types of valveless micropumps, both 200 µm thick, were measured and compared. Recall that this measurement was taken without flow. As shown in Figure 4.8d, the nozzle-diffuser type micropump has a higher pressure difference than the Tesla-type fluidic diode-based micropump. This is as expected because the designed Tesla-type fluidic diode has a small pressure difference, as shown in Figure 4.4c. Although the designed Tesla-type fluidic diode has high diodicity, its pressure differences are relatively low. However, the mismatch of pressure differences between the two valveless micropumps is only around 10%. Relative to the 2.2 times enhancement of the mass flow rate for the Tesla-type diode micropump, this small difference of pressure drop is justified.

4.5 Conclusion

This work provides an efficient design process for developing a high-performance fluidic diode-based valveless micropump. A two-dimensional fluidic diode was first obtained by topology optimization. The diodicity reached 5.31 with a Reynolds number of 100. Then the thickness and layout of the Tesla-type designed fluidic diode were optimized and deployed in the valveless micropump. The performance of the proposed valveless micropump was evaluated by both CFD simulation and experiments. The result shows that the high diodicity of the Tesla-type designed fluidic diode leads to better performance at low Reynolds numbers among the two valveless micropumps. It was proven that the valveless micropump 200 μm thick with the designed Tesla-type fluidic diode can achieve 2.2 times the mass flow rate of the traditional nozzle-diffuser type valveless micropump. Many applications will benefit from the high flow rate of the designed valveless micropump. For example, more efficient mixing caused by stronger convection can be expected when the valveless micropump is used for mixing of microfluidic streams. Also, higher throughput for drug delivery and stronger actuation for ‘organs on a chip’ can be expected.

Chapter 5: Valveless Micropump Microfluidic Sensor Based on a Pyrolytic Glassy Carbon and Graphene Composite Electrode for Heavy Metal Detection

5.1 Introduction

Heavy metal ions are defined as the ionic form of metallic elements with a relative density greater than 5 g/cm³, including lead, mercury, cadmium, chromium, thallium, and others.[106] Natural processes like weathering and volcanic activity, as well as anthropogenic sources like mining, smelting, and industrial wastewater discharge, can introduce these ions into the environment.[107] These ions pose significant risks to the environment and human health due to their persistence in nature and harmful effects on the ecosystem, human health and the economy. Soil and water contamination by heavy metal ions can lead to significant losses of biodiversity in plants and animals.[108, 109] Human exposure to these ions can result in severe health problems, including damage to the nervous system, kidneys, and liver, and even an increased risk of cancer.[110, 111] Lead (Pb) and cadmium (Cd) are among the most common heavy metal pollutants, with exposure to these metals associated with cancer, kidney damage, and developmental disorders.[112] Lead exposure is responsible for 0.6% of the global burden of disease and an estimated 143,000 deaths per year, while Cd has been classified as a human carcinogen by the International Agency for Research on Cancer (IARC) and the World Health Organization (WHO).[113, 114, 115] The EPA has set an action level of 15 parts per billion (ppb) for Pb in drinking water and a non-enforceable health advisory level of 5 ppb for Cd. [116] Therefore, effective detection of heavy metal ions in ambient water, especially drinking water, is crucial for protecting public health and the environment.

There are several current analytical technologies for detecting heavy metals in water. Commonly used methods include atomic absorption spectroscopy (AAS), inductively coupled plasma mass spectrometry (ICP-MS), and X-ray fluorescence (XRF) spectroscopy, which exhibit high sensitivity and selectivity.[117, 118, 119] However, these methods often require expensive equipment, skilled personnel, and complicated procedures. Hence, the development of low-cost and accurate sensors for on-site heavy metal detection has gained significant attention. Among them, anodic stripping voltammetry (ASV) stands out as a promising technology due to its high sensitivity, accuracy, and precision at a relatively low cost.[120] The method involves deposition of the metal ions onto an electrode surface which is called accumulation, followed by a stripping step where the metal ions are oxidized and released from the electrode surface. The ion current resulting from this oxidation is measured. It is proportional to the concentration of the metal ions in solution.[121] Application of ASV has been verified for the detection of multiple heavy metal ions with high sensitivity and selectivity. [122, 123, 124] However, there are still some barriers that hinder further development of ASV, and electrode materials and mass transfer are two of the most important barriers that limit its sensitivity and its limit of detection (LOD).

The electrode material for ASV must have a faster electron transfer rate to generate a higher stripping peak, a lower overpotential to prevent hydrogen gas formation during the accumulation process, and stable physical and chemical properties to ensure long-term stability. Metallic materials, including mercury (Hg), silver (Ag), gold (Au), and bismuth (Bi), were initially utilized for ASV measurements of heavy metals.[125, 126, 127] However, because of their low activation energy overpotential, chemical inertness, and good long-term stability, glassy carbon materials obtained by pyrolyzing polymers has gained recent attention.[128] Subsequently, extensive work has been focused on surface modification of glassy carbon electrodes with metals, metal oxides, polymers, and other carbon-based materials to enhance their electrochemical performance.[129, 130, 131] One is graphene as a single layer or a few layers of graphite with sp2 carbon atoms arranged in a honeycomb crystal lattice. It has been widely used in electrochemical sensing due to its large theoretical surface area, high electrical conductivity, and fast electron transfer rate.[132] Graphene modification on glassy carbon electrodes is typically achieved through drop-casting, electroreduction, or solution transfer, which often produce unstable and poorly reproducible results. [133, 134, 135] Therefore, a stable and highly reproducible method is desired for synthesizing glassy carbon/graphene composite materials for ASV measurements.

The sensitivity of ASV measurement is also limited by the amount of heavy metal ions that are reduced in the accumulation process, and microfluidics technology is considered an effective approach to increase the sensitivity due to its enhanced mass transfer and, thus, faster chemical reaction.[136] Zou et al. used a simple microfluidic device with a pair of inlets, an outlet, and a reaction chamber, along with a bismuth electrode, to measure Pb and Cd in water, achieving detection limits of 8 ppb and 9.3 ppb, respectively.[137] Hong et al. used a 3D printed microfluidic device with similar structure and achieved lower detection of 0.2 ppb and 0.5 ppb for Pb and Cd, respectively.[138] After that, the electrochemical paper based analytical devices (ePADs) for ASV measurement gain more attention due to their low-cost, high selectivity and sensitivity. The Shen group achieved detection limits of 1.8 ppb and 1.2 ppb for Pb and Cd, respectively, by embedding working and counter electrodes into a microfluidic paper channel.[139] These published microfluidic-based ASV sensors mostly utilize simple one-way microchannels, and the mass transfer efficiency is mainly determined by the flow rate.[140] Moreover, a large volume of samples and precise and expensive syringe pumps are required for the measurement.

In this work, a new simple, repeatable, and low-cost glassy carbon/graphene composite material that can be used for ASV measurement of heavy metal ions is presented. A valveless micropump with unique flow characteristics is then integrated with the electrodes to achieve extremely low detection limits by further enhancing mass transfer efficiency through its rapid reciprocating motion while driving fluid movement.

5.2 Body of Knowledge

Anodic Stripping Voltammetry (ASV) is an extensively utilized electrochemical technique for the sensitive and selective measurement of heavy metal ions in diverse sample matrices. It offers high sensitivity, selectivity, and quantitative measurement of trace levels of heavy metal ions.

The ASV measurement involves two key steps: preconcentration and stripping. As shown in Figure 5.1, in the preconcentration step, a negative potential is applied to the working electrode, causing the deposition of heavy metal ions from the solution onto the electrode surface. Subsequently, a potential sweep from negative to positive values is performed, leading to the oxidation and sequential stripping of the accumulated heavy metals. The resulting changes in current are recorded, enabling the identification and quantification of heavy metal ions based on the location and height of the stripping peaks.

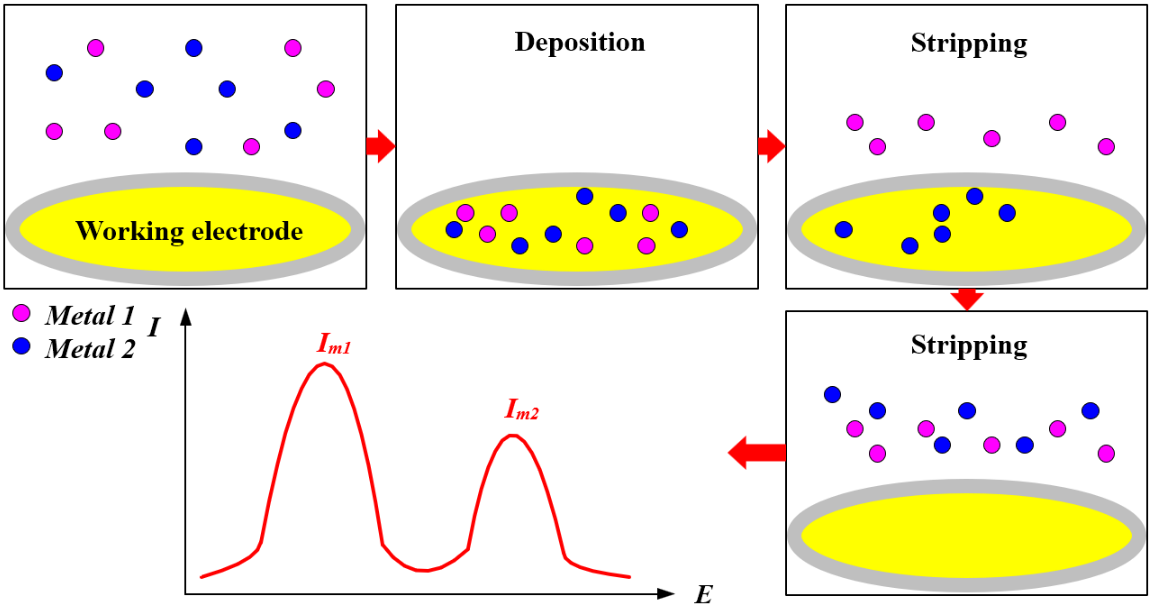

Figure 5.1 Working mechanism of Anodic Stripping Voltammetry (ASV) for heavy metal ions detection.

Anodic Stripping Voltammetry (ASV) offers notable advantages in heavy metal ion measurement. The preconcentration step allows for the accumulation of heavy metals on the electrode surface, leading to enhanced sensitivity and detectability, particularly for trace levels of heavy metal ions. The technique exhibits excellent selectivity, enabling the simultaneous detection of multiple heavy metal ions in a single analysis. Furthermore, ASV is characterized by its efficiency and time-saving capabilities.

Overall, ASV is a valuable tool for accurate and reliable determination of heavy metal ions in various sample types. Its high sensitivity, selectivity, and ability to detect multiple analytes simultaneously make it a preferred choice in environmental monitoring, industrial process control, and analytical chemistry applications.

5.3 Fabrication and Characterization

Micro-electromechanical systems (MEMS) based techniques were used to fabricate pyrolyzed glassy carbon/graphene electrodes in a microfluidic system. The structure and fabrication process of the device are illustrated in Figures 4.2a and 4.2b, respectively. The device is comprised of a three-electrode system for electrochemical sensing and a microfluidic system featuring a nozzle/diffuser type valveless micropump.[141]

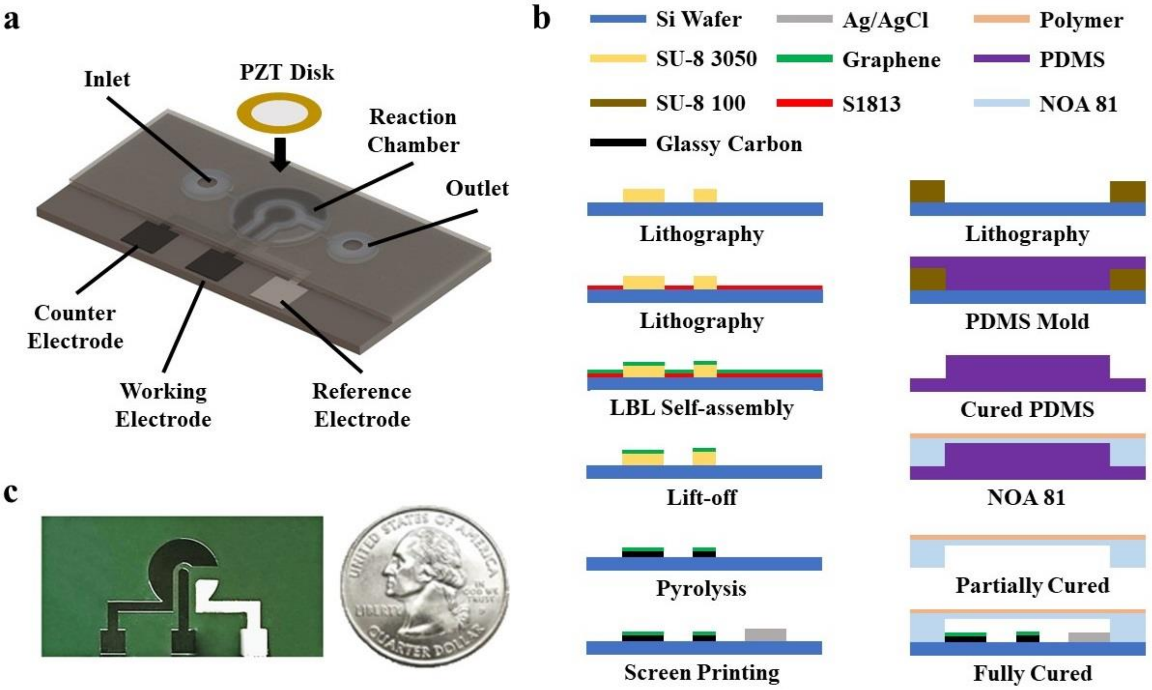

Figure 5.2 (a) Sketch of a microfluidic heavy metal sensor with a valveless micropump; (b) schematic diagram of the fabrication process; (c) Picture of the fabricated three electrode system.

The working and counter electrodes were made of pyrolyzed glassy carbon/graphene composite material. The material synthesis started by spin-coating the negative photoresist SU-8 3050 on a silicon wafer at 4000 rpm, which resulted in a thickness of 45 µm. The photoresist was patterned using photolithography to form the desired electrode structure. The graphene was deposited onto the photoresist using a layer-by-layer (LBL) self-assembly technique.[142] This involved immersing the wafer with electrode-shaped photoresist in a positively charged poly(diallyldimethylammonium chloride) (PDDA) solution and then in a solution with negatively charged graphene. Each immersion lasted 10 minutes, and the wafer was rinsed with deionized water between immersions to remove unbound materials. This process was repeated multiple times to assemble different numbers of PDDA/graphene bilayers. The wafer with photoresist and assembled graphene was then pyrolyzed at 1100 ºC for 5 hours with a continuous flow of a mixture of 5% hydrogen and 95% argon gas.

A silver/silver chloride reference electrode was fabricated by screen printing of silver/silver chloride paste. Figure 5.2c shows the picture of the fabricated three electrodes system on a silicon wafer.

The microfluidic system consists of a reaction chamber and two nozzle/diffuser fluid diode structures, which are connected to the inlet and outlet chambers. The parameters of the nozzle/diffuser structures were described in Chapter 4.[143] Fabrication of the valveless micropump began with the patterning of the structure on a silicon wafer through photolithography of negative photoresist SU-8 100, resulting in a photoresist thickness of 200 µm. Subsequently, a polydimethylsiloxane (PDMS) mold was created by pouring PDMS on the silicon-based mold and curing it. The PDMS mold with mating structures was then used to apply UV-curing glue (NOA81) on top and covered with a UV-transparent polystyrene polymer film. The glue was partially cured under UV illumination for 1 minute, after which the PDMS mold was replaced with the silicon wafer with glassy carbon/graphene electrodes. More UV illumination was applied to fully cure the glue. Finally, a piezoelectric (PZT) disc with a diameter of 10 mm was attached to the polymer film as the actuator.

The conductivity of the synthesized glassy carbon was evaluated using a Four Point Probe (Veeco FPP5000), while Energy-Dispersive X-Ray Spectroscopy (EDS) (JEOL 6500 Field Emission Gun) was employed to determine the elemental composition of the photoresist and graphene composite before and after pyrolysis. Raman spectroscopy was used to characterize the molecular structure of the pyrolyzed products, which was conducted using a Confocal Raman Microscope.

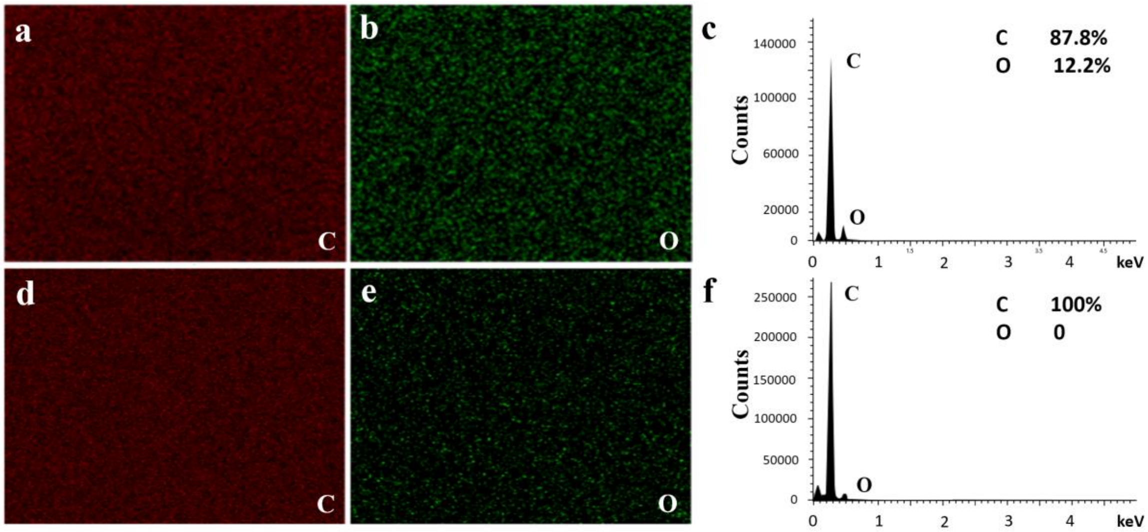

Figure 5.3 EDS elemental maps of SU-8/PDDA/Graphene composite material before pyrolysis (a) carbon (b) oxygen; (c) Histogram of elements for SU-8/PDDA/Graphene composite material before pyrolysis, the peaks shown are carbon (left) and oxygen (right); EDS elemental maps of SU-8/PDDA/Graphene composite material after pyrolysis (d) carbon (e) oxygen; (f) Histogram of elements for glassy carbon/graphene composite after pyrolysis.

The element composition of SU-8 3050 with coated graphene before and after the pyrolysis was analyzed by EDS. The result is shown in Figure 5.3. Both photoresist and PDDA are organic compounds primarily composed of carbon and oxygen, while graphene is a carbon-based material with a small amount of oxygen. Therefore, Figure 5.3a shows a uniform and abundant distribution of carbon and oxygen elements. The histogram in Figure 5.3b confirms that carbon is the most abundant element, accounting for 87.5%, followed by oxygen at 12.5%. After high-temperature pyrolysis in a hydrogen atmosphere, the oxygen in the material reacts with hydrogen and is removed, leading to a significant decrease in the proportion of oxygen, as shown in Figures 5.3a and 5.3b. The proportion of oxygen decreases from 12.5% to 1.2%. As a result, the non-conductive organic photoresist transforms into conductive glassy carbon, with a conductivity of 4600 S/m measured by the Four Point Probe.

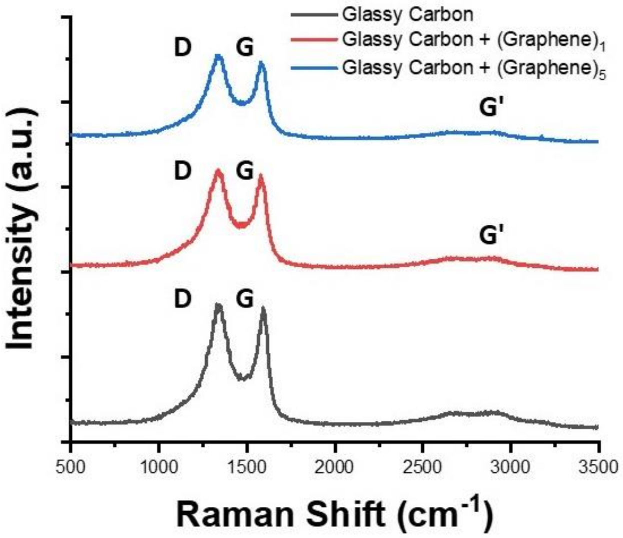

Figure 5.4 Raman spectra of bare glassy carbon and glassy carbon with different layers of LBL self-assembled graphene.

Figure 5.4 shows the Raman spectra of pyrolytic glassy carbon without graphene and glassy carbon containing different number of PDDA/graphene bilayers. In all three spectra, a prominent D peak at 1358 cm^{-1} and a G peak around 1580 cm^{-1} can be observed. The ratio of the two peak heights is related to the degree of microstructural disorder, consistent with previous reports in the literature.[144] Because the self-assembled graphene layer is thin, and because of the similarity of its characteristic peaks to those of glassy carbon, it is difficult to distinguish graphene in the Raman spectra. Furthermore, a broad 2D peak at 2700 cm^{-1} was observed in both graphene-containing samples, indicating that the coated graphene is multilayer graphene even with only one cycle of LBL self-assembly.

5.4 Optimization of Experimental Conditions

The electrochemical performance of glassy carbon/graphene electrodes was assessed through ASV measurement of Pb in a fixed concentration bulk solution. Glassy carbon/graphene electrodes with varying numbers of PDDA/graphene bilayers on SU-8 3050 applied before pyrolysis were first tested and compared. To improve the visibility of the stripping peaks at low concentrations, electrodes with a much larger surface area, 25 times greater than the one used in the microfluidic system, were employed. The results are depicted in Figure 5.5.

The number of PDDA/graphene bilayers was varied from 0 to 6. In the presence of graphene, a distinct Pb stripping peak was observed at around -0.63 V. However, when the number of bilayers was 0, indicating the absence of graphene on the glassy carbon surface, the Pb stripping peak was not observed. Additionally, the height of the Pb stripping peak increased initially and then decreased as the number of PDDA/graphene bilayers increased.

This trend because a single LBL self-assembly cycle of PDDA/graphene is insufficient to ensure uniform and complete coverage of the surface by graphene, whereas an excessive number of graphene layers results in a lower electron transfer rate due to slow electron mobility between the graphene layers. Therefore, for the current application, the optimal number of PDDA/graphene bilayers prepared by LBL self-assembly before pyrolysis is two.

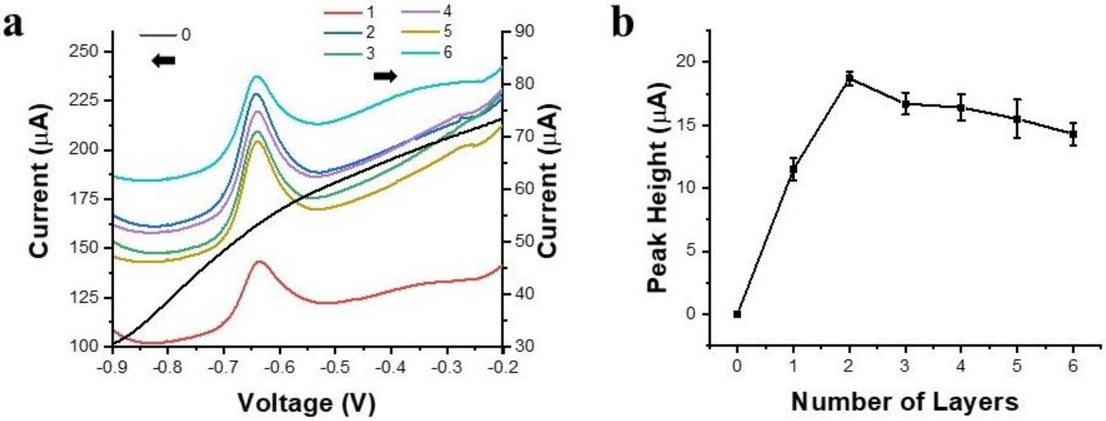

Figure 5.5 (a) Stripping voltammograms for glassy carbon with different numbers of layers of LBL self-assembled graphene, Pb: 20 ppb; (b) Pb peak height for glassy carbon with different numbers of layers of LBL self-assembled graphene, Pb: 20 ppb.

Then the influence of bismuth (Bi) concentration on the detection of heavy metals was investigated. Bismuth, known for its low toxicity and eco-friendliness, was utilized as a replacement for toxic Hg to achieve an undistorted stripping response and a broad linear dynamic range. The formation of multi-component Bi alloys with detected heavy metals is responsible for generating a higher stripping peak and a narrower peak width.[145]

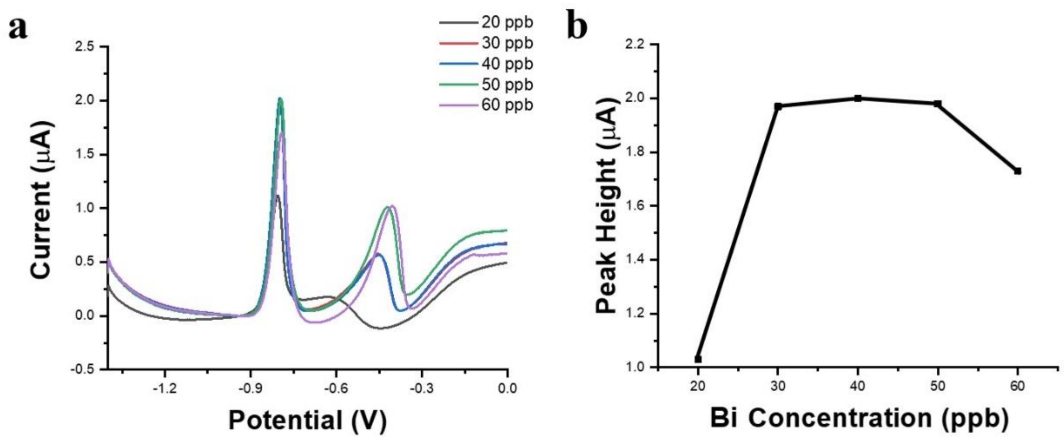

Figure 5.6 (a) Stripping voltammograms for increasing levels of Bi from 20 ppb to 60 ppb, Pb: 10 ppb, valveless micropump, mass flow rate: 10 mL/h; (b) Pb peak height for increasing Bi concentration, Pb: 10 ppb, valveless micropump, mass flow rate: 10 mL/h.

The microfluidic system was employed for the experiments with a mass flow rate of 10 mL/h. Diluted Bi with concentrations ranging from 20 ppb to 60 ppb was added to acetic acid buffer with Pb, where the Pb concentration was maintained at a constant 10 ppb. The stripping current peak of both Pb and Bi was presented in Figure 5.6a, and the effect of Bi concentration on Pb peak height was depicted in Figure 5.6b. The results indicate that the Pb peak height initially increased and then decreased with the increase of Bi concentration. This phenomenon is because Bi can facilitate the formation of Bi-Pb alloy at low concentrations, which is more easily stripped and leads to a higher peak height. Nevertheless, an excessive amount of Bi ions can compete with Pb ions during the accumulation process, resulting in a decreased amount of reduced and stripped Pb ions. Consequently, a Bi concentration of 40 ppb was recommended to achieve a higher Pb stripping peak.

5.5 Single Heavy Metal Ion Measurement

Following the determination of the optimal Bi concentration, the measurement of Pb was carried out under different conditions in this study. Specifically, the differences between two distinct methods of driving fluid in the microfluidic system were compared with the measurement taken in the absence of fluid flow.

Figures 5.7a and 5.7b display the stripping current of Pb with Bi concentration fixed at 40 ppb and Pb concentration ranging from 1 ppb to 25 ppb, where fluidic flow was driven by a syringe pump (Figure 5.7a) and a valveless micropump (Figure 5.7b), respectively, with the same mass flow rate of 10 mL/h. The results indicate that the Pb peak height increases with an increase in Pb concentration, and the peak height being significantly larger when the valveless micropump is used as an actuator.

The valveless micropump comprises two nozzles/diffuser-shaped flow-directing elements that are connected to a chamber with an oscillating diaphragm of piezoelectric ceramic. The piezoelectric ceramics vibration alters the chamber's volume, causing the solution to rapidly flow in and out of the chamber. The unique flow directing elements achieve the net flow of the solution in one direction by utilizing different flow resistances in different flow directions. Figure 5.8 shows a Computational Fluid Dynamic (CFD) simulation of this process, indicating that the instantaneous flow velocity in the chamber can reach up to 1 m/s, which is much faster than the flow velocity in one direction driven by a syringe pump. This unique fast reciprocating motion enables rapid mixing and high mass transfer rate in the chamber, resulting in much higher sensitivity with the same net flow rate.

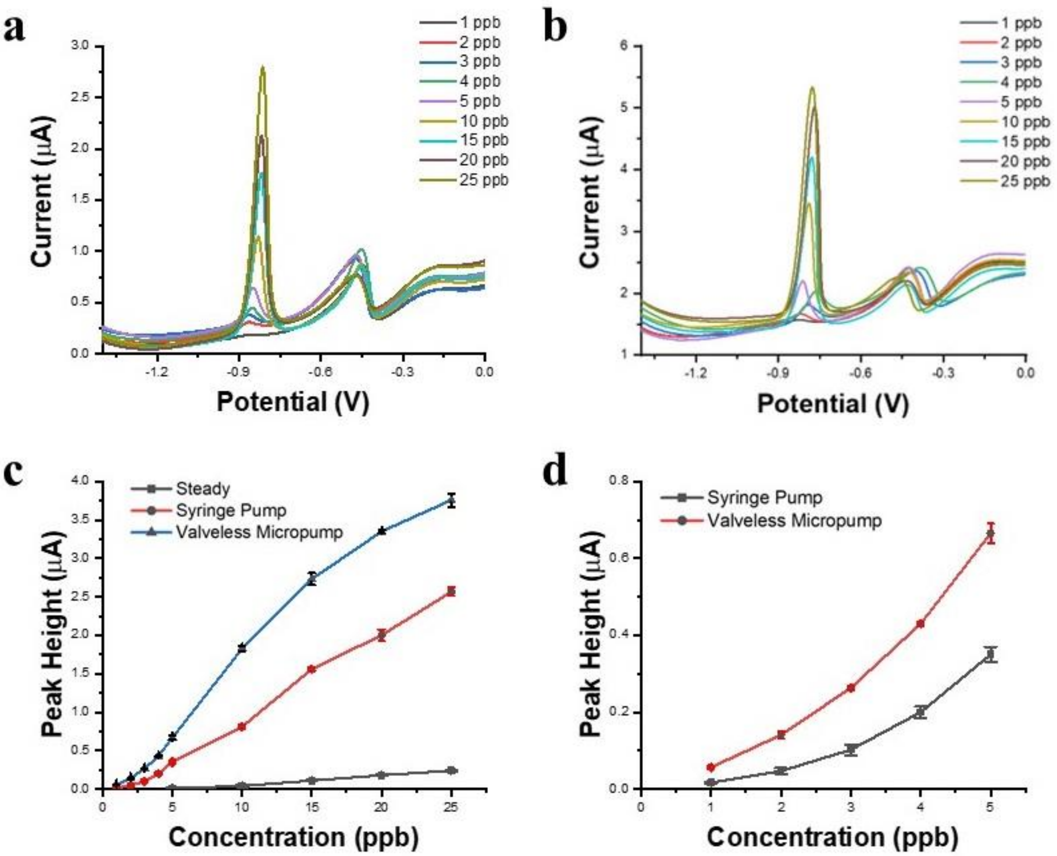

Figure 5.7 (a) Stripping voltammograms for increasing Pb concentrations from 1 ppb to 25 ppb, Bi: 40 ppb, syringe pump, mass flow rate: 10 mL/h; (b) Stripping voltammograms for increasing Pb concentrations from 1 ppb to 25 ppb, Bi: 40 ppb, valveless micropump, mean mass flow rate: 10 mL/h; (c) Calibration plot of Pb under different conditions, Bi: 40 ppb, mean mass flow rate: 10 mL/h; (d) Calibration plot of Pb at low concentrations, Bi: 40 ppb, mean mass flow rate: 10 mL/h.

The peak height of Pb under different conditions were calculated and plotted in Figure 5.7c, where the steady case (no flow) refers to turning off both pumps, and no fluid motion occurs. The figure reveals that when the Pb concentration is above 5 ppb, the stripping peaks generated under no fluid movement and the fluid movement propelled by the syringe pump conditions show a linear correlation between concentration and peak height. However, the measurements with the valveless micropump show reduced sensitivity at high concentrations, which may be due to the reduced Pb on the electrode surface when saturation is approached. Nevertheless, measurements with the valveless micropump exhibit sensitivity 50% higher than that of the syringe pump under the same net flow rate, and its sensitivity is two orders of magnitude higher than that of measurements with no pumping of solution.

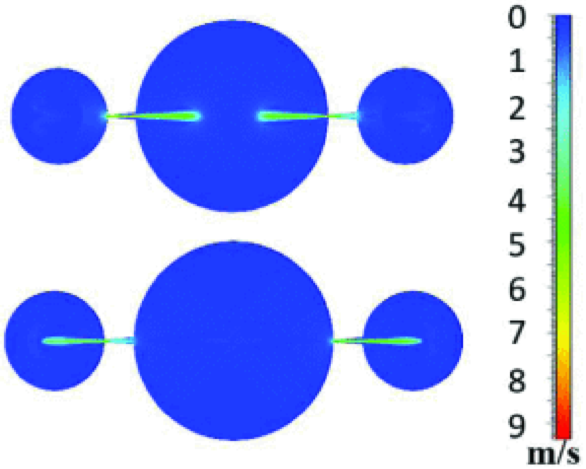

Figure 5.8 Velocity contours of, the valveless micropump in the supply mode (upper) and the pump mode (lower).

Figure 5.7d provides a zoom-in result of Figure 5.7c at low concentrations, indicating that when the Pb concentration is below 5 ppb, no visible stripping peaks can be generated in the detection with stationary solution. Both detections with fluid flow driven by the two pumps show reduced sensitivity with decreasing concentration. This may be due to the difficulty of nucleation of reduced heavy metal ions on the electrode surface with low concentrations, and the small size of the nucleus reduces the contact area with the solution, resulting in a decrease of reduced heavy metal ions during accumulation.

The limit of detection (LOD) of Pb detection was calculated based on the noise level and sensitivity at the lowest concentration. When there was no flow, the LOD was 4 ppb. When the solution was driven by a syringe pump, the LOD was 80 ppt. However, when the solution was driven by a valveless micropump, an LOD of 20 ppt was achieved.

The measurement was also conducted for Cd detection, while only the valveless micropump was used to achieve higher sensitivity and a lower LOD. Figures 5.9a and 5.9b show the stripping current under different Cd concentrations and the calibration curve, and the LOD for Cd detection is 100 ppt.

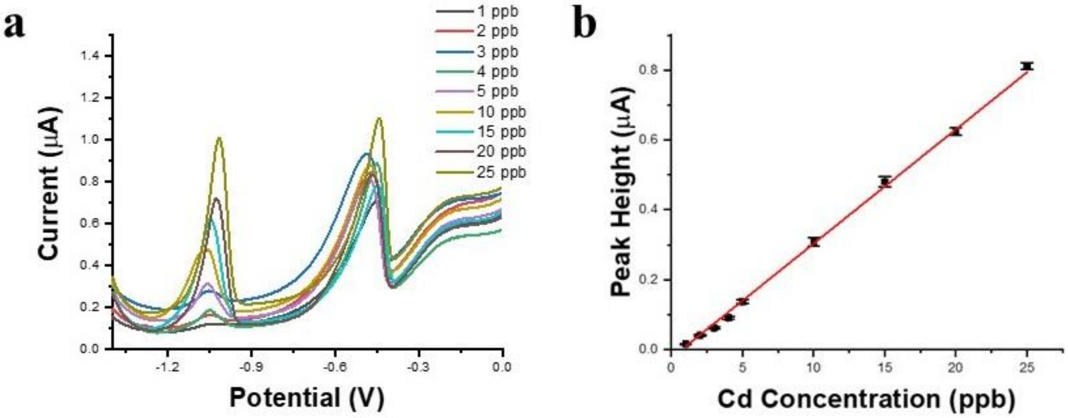

Figure 5.9 (a) Stripping voltammograms for increasing Cd concentrations from 1 ppb to 25 ppb, Bi: 40 ppb, valveless micropump, mass flow rate: 10 mL/h; (b) Calibration plot of Cd, Bi: 40 ppb, valveless micropump, mass flow rate: 10 mL/h.

5.6 Pb, Cd Mixture Measurement

Although the ASV sensor can distinguish different heavy metal ions based on the position of the stripping peaks according to their different redox potentials, it is also noted that there are mutual interferences among various heavy metal ions.[146] In this section, the coexistence of Pb and Cd is taken as an example to explore the ion interference in the ASV process and provide a general solution.

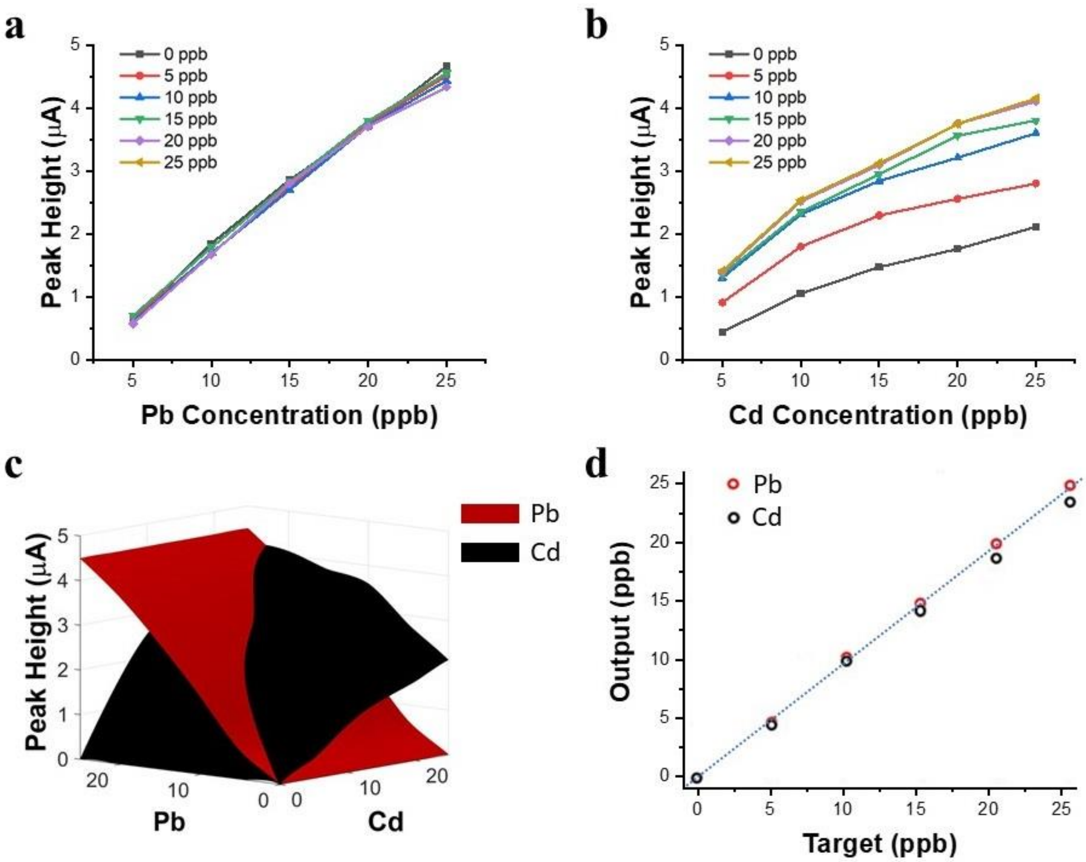

Figure 5.10 (a) Calibration plot of Pd with existence of different concentrations of Cd from 0 ppb to 25 ppb, Bi: 40 ppb, valveless micropump, mean mass flow rate: 10 mL/h; (b) Calibration plot of Cd with existence of different concentrations of Pb from 0 ppb to 25 ppb, Bi: 40 ppb, valveless micropump, mass flow rate: 10 mL/h; (c) Three-dimensional calibration curves for Pb (red) and Cd (black); (d) Testing the goodness of the fit of the target (known concentration) and output (neural network result).

First, the effect of the existence of lead and cadmium on each other's stripping peaks was studied. Figure 5.10a shows the calibration curves of Pb in the presence of different concentrations of Cd. The stripping peaks of Pb at the same concentration do not differ significantly as Cd concentration changes, indicating a negligible effect of Cd on the stripping peak of Pb. However, in the calibration curves of Cd in the presence of different concentrations of Pb, shown in Figure 5.10b, the concentration variation of Pb has a significant effect on the stripping peak of Cd. Specifically, the presence of Pb makes the stripping peak of Cd more significant, and this enhancement tends to saturate when the concentration of Pb reaches 20 ppb.

Interestingly, this phenomenon differs from the results obtained with other electrode materials in bulk solution reported in the literature.[147, 148, 149] In those works, only a small, negligible effect of Cd on the Pb stripping peak was observed, which is consistent with the results obtained in the present study. Moreover, in the present study, the competition of Cd with Pb deposition was less significant due to the accelerated mass transfer, which further minimized the effect of Cd on the Pb stripping peak. However, in these tests, it is generally believed that Pb has little effect on the stripping peak of Cd or that the presence of Pb reduces the stripping peak of Cd, which is opposite to the results of this experiment. A commonly accepted explanation for these experimental results is that Pb preferentially deposits during the accumulation stage of ASV, followed by the relatively uniform deposition of Cd on the electrode surface and the pre-existing Pb nanoparticles through mass transfer control. Cadmium deposited on Pb is believed to be mostly in a monolayer, so it is not stripped with more negative Cd stripping potentials and is stripped together with Pb.[150] However, in the present study, the faster mass transfer efficiency and more negative enrichment potential may have caused significant Cd deposition, breaking the assumption that Cd deposited on Pb is mostly in a monolayer. Therefore, Cd deposited on Pb was stripped together with Pb at the Cd stripping potential, and the presence of the Bi-Pb-Cd alloy may result in an even more distinct stripping peak.

A three-dimensional calibration curve for simultaneous detection of Cd and Pb was then established as shown in Figure 5.10c. In this plot, the red surface represents the peak height of the Pb stripping peak under the coexistence of Pb and Cd, while the black surface represents the peak height of the Cd stripping peak under the same conditions. Since the effect of Cd on the Pb stripping peak was found to be negligible as shown in Figure 5.10a, the average calibration curve from Figure 5.10a was used to approximate the calibration curve of Pb. Once the peak heights of both Pb and Cd in a single stripping were obtained, a plane perpendicular to the Z-axis was first determined through the height of Pb stripping peak, which would intersect with the red Pb calibration plane to form a line of intersection. Then, another plane perpendicular to the Z-axis was determined through the height of the Cd stripping peak, which would intersect with the black Cd calibration plane to form another line of intersection. The point of intersection between the two lines corresponds to the concentrations of Pb and Cd in the sample solution.

Finally, a simple multilayer feedforward neural network model was used to learn the relationship between the shape of the stripping peak and the concentrations of the two heavy metal ions. This approach simplifies the process of data processing and analysis and allows for more accurate determination of ion concentrations based on the shape of the stripping peak rather than relying solely on peak height as a single data point. More importantly, when the sensor is used for mixed detection of multiple ions, the stripping peaks may overlap, making it difficult to the determine peak height. The use of neural networks to analyze the shape of the stripping peak avoids this problem.[151, 152] All 140 ASV test curves under different Pb and Cd concentration combinations were used as the dataset. Among them, 90% were used as a training set and the rest as a test set. As the number of hidden neurons increased from 5 to 16, the mean squared error (MSE) of the network's validation decreased significantly from 3.91 to 0.18. Subsequently, increasing the number of hidden neurons did not significantly improve the performance of the network. Therefore, 16 hidden neurons were used as the final model for analysis. Figure 5.10d shows the linear fit between the test targets (known concentrations) and the outputs (neural network results), where the red color represents the results for Pb and the black color represents the results for Cd. The test results show a linear relationship with the real concentration and indicate an underestimation of Cd concentration, which may be due to the insufficient estimation of the increase in Cd peak height due to the presence of Pb, caused by the relatively small sample size.

5.7 Conclusion

In this work, a glassy carbon/graphene electrode was fabricated by LBL self-assembly of graphene on photoresist and subsequent high temperature pyrolysis and was employed for electrochemical heavy metal sensor. The sensitivity of the sensor was further enhanced, and the detection limit was lowered by integrating it with a valveless micropump system. The LBL self-assembly of PDDA/graphene bilayer was optimized to two layers, and the concentration of Bi ion in test solution was optimized to 40 ppb. Two different actuators were utilized to drive fluidic motion, and the sensor system with valveless micropump achieved a lower detection limit of 20 ppt for Pb and 100 ppt for Cd, which is one order of magnitude lower than existing work with similar approaches. The sensitivity was two orders of magnitude higher than that without fluid flow, and 1.5 times higher than that of the sensor driven by a syringe pump at the same flow rate. The sensor response in the coexistence of both Pb and Cd was investigated, revealing an interaction between Pb and Cd that differed from previously published results, and for the first time, a positive influence of Pb on the ASV measurement of Cd was noticed. Finally, three-dimensional data analysis and neural network were both employed to provide data fitting for simultaneous detection of Pb and Cd. In summary, this work achieved low-cost, rapid, and accurate simultaneous detection of multiple heavy metals using a sensitive glassy carbon/graphene electrode and a valveless microfluidic system.

Chapter 6: Conclusions and Outlook for Future Work

6.1 Conclusions

This dissertation explores the application of Micro-Electro-Mechanical Systems (MEMS) technology to sustainable water management. It introduces the concept of a closed-loop control water treatment system and advances the development of an intelligent platform through research in three key areas: water purification, pumping system, and water sensing. The objective of this research is to provide new perspectives in addressing the challenges of water pollution and water scarcity by applying these technologies to water management.

Firstly, an in-depth investigation was conducted on the principles of photocatalysis and photoelectrocatalysis, as well as their applications to water treatment. The proposed new configuration of photoelectrocatalysis facilitates simultaneous removal of organic pollutants and heavy metal ions. This technology has been validated in both bulk systems and microfluidic systems. This demonstrates that this approach can be applied to large-scale water purification, such as wastewater treatment in factories, water purification in water plants, and water purification in rivers or lakes. The application of this technology to microfluidic systems enables the development of compact and portable water treatment devices. Potential application scenarios include household water treatment platforms, outdoor drinking water treatment, and possible military applications.

Secondly, a high performance micropump for miniaturized water purification systems was investigated. Inspired by Tesla valves, a new valveless micropump with higher pumping efficiency was developed. The developed valveless micropump has a small size, allowing for seamless integration with MEMS technology and microfluidic systems. The initial purpose of this development was to provide propulsion for liquid flow in portable water treatment platforms. However, its rapid liquid pumping capability gives it potential applications to medical and chemical fields. The unique characteristics of high-speed and high-frequency reciprocating liquid flow have inspired its applications to sensors because of enhanced mass transfer.

Finally, a highly sensitive electrochemical and microfluidic sensor for heavy metal ion detection was developed. This sensor leverages the microfluidic characteristics of new composite materials and valveless micropumps to achieve detection of trace concentrations of heavy metal ions. It provides the hardware foundation for water quality data collection in the intelligent water treatment platform. Moreover, the synthesized glassy carbon/graphene composite materials and the valveless micropump microfluidic platform can be combined with various detection methods, enabling the detection of numerous physical, chemical, and biological signals beyond heavy metal ions.

In summary, this dissertation serves as a pivotal exploration of the application of MEMS to the sustainable management of water resources. It establishes three distinct yet interconnected systems: water treatment, a microfluidic pump, and a microsensor. Their integration provides a technological foundation for intelligent water treatment systems. Each of these systems has its own independent significance while also holding broad prospects for application to other fields.

6.2 Outlook for Future Work

This dissertation lays a solid foundation for future continued work on intelligent water purification system which is proposed below:

The proposed intelligent close-loop control water purification system consists of valveless micropumps, electrochemical microsensor array, an integrated PEC system, and a microprocessor. Figure 6.1 shows the basic control strategy of the system. The photocatalytic water treatment starts when water flows through the reaction chamber and the UV light is turned on. The pollution concentration of the inlet water is monitored by electrochemical microsensors and the result is transferred to the microprocessor. The microprocessor evaluates the pollution value transmitted by the sensor and generate appropriate mass flow rate that can remove pollutants with less residual time.

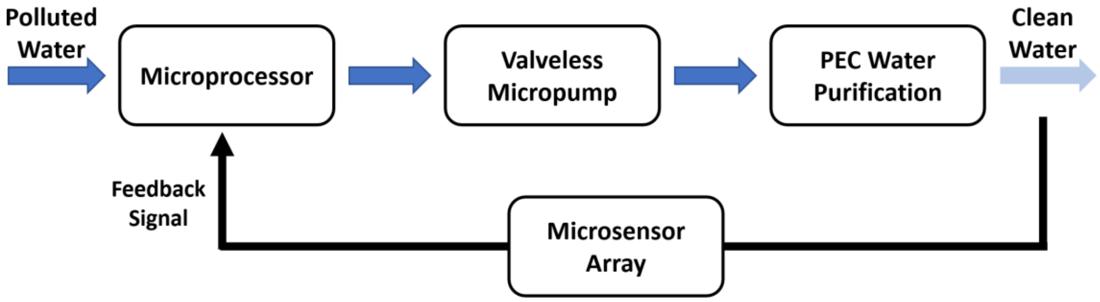

Figure 6.1 A schematic of the proposed intelligent closed loop control water purification system.

Furthermore, the system can be augmented with a sensor network and machine learning models, enabling real-time adjustments to the water flow rate or addition of chemicals based on the predictions of the machine learning models and the results of inverse modeling. This integration allows for dynamic management of water quality in the purification system, facilitating rapid responses to changes in water quality and proactive measures to prevent issues before they arise. The incorporation of machine learning algorithms enhances the system's adaptive capabilities, optimizing water treatment processes and ensuring efficient and sustainable water purification.

Bibliography

1 W. H. Organization, Progress on household drinking water, sanitation and hygiene 2000-2020: five years into the SDGs. 2021.

2 “Transforming Our World: The 2030 Agenda for Sustainable Development,” doi: 10.1891/9780826190123.ap02.

3 L. Comte, J. D. Olden, S. Lischka, and B. G. Dickson, “Multi-scale threat assessment of riverine ecosystems in the Colorado River Basin,” Ecological Indicators, vol. 138, p. 108840, 2022, doi: 10.1016/j.ecolind.2022.108840.

4 UNESCO, The United Nations World Water Development Report 2020. 2020.

5 J. B. Wathen, J. M. Lazorchak, A. R. Olsen, and A. Batt, “A national statistical survey assessment of mercury concentrations in fillets of fish collected in the U.S. EPA national rivers and streams assessment of the continental USA,” Chemosphere, vol. 122, pp. 52–61, 2015, doi: 10.1016/j.chemosphere.2014.11.005.

6 K. L. Wasewar, S. Singh, and S. K. Kansal, “Process intensification of treatment of inorganic water pollutants,” pp. 245–271, 2020, doi: 10.1016/b978-0-12-818965-8.00013-5.

7 S. N. Zulkifli, H. A. Rahim, and W.-J. Lau, “Detection of contaminants in water supply: A review on state-of-the-art monitoring technologies and their applications,” Sensors and Actuators B: Chemical, vol. 255, pp. 2657–2689, 2018, doi: 10.1016/j.snb.2017.09.078.

8 M. Hanna-Attisha, J. LaChance, R. C. Sadler, and A. Champney Schnepp, “Elevated Blood Lead Levels in Children Associated With the Flint Drinking Water Crisis: A Spatial Analysis of Risk and Public Health Response,” Am J Public Health, vol. 106, no. 2, pp. 283–290, 2016, doi: 10.2105/ajph.2015.303003.

9 A. Prüss-Ustün et al., “Burden of disease from inadequate water, sanitation and hygiene for selected adverse health outcomes: An updated analysis with a focus on low- and middle-income countries,” International Journal of Hygiene and Environmental Health, vol. 222, no. 5, pp. 765–777, 2019, doi: 10.1016/j.ijheh.2019.05.004.

10 M. N. Chong, B. Jin, C. W. K. Chow, and C. Saint, “Recent developments in photocatalytic water treatment technology: A review,” Water Research, vol. 44, no. 10, pp. 2997–3027, 2010, doi: 10.1016/j.watres.2010.02.039.

11 Z. Wang, A. Wu, L. Colombi Ciacchi, and G. Wei, “Recent Advances in Nanoporous Membranes for Water Purification,” Nanomaterials, vol. 8, no. 2, p. 65, 2018, doi: 10.3390/nano8020065.

12 Z. Karim, A. P. Mathew, M. Grahn, J. Mouzon, and K. Oksman, “Nanoporous membranes with cellulose nanocrystals as functional entity in chitosan: Removal of dyes from water,” Carbohydrate Polymers, vol. 112, pp. 668–676, 2014, doi: 10.1016/j.carbpol.2014.06.048.

13 M. Pera-Titus, V. García-Molina, M. A. Baños, J. Giménez, and S. Esplugas, “Degradation of chlorophenols by means of advanced oxidation processes: a

general review," Applied Catalysis B: Environmental, vol. 47, no. 4, pp. 219–256, 2004, doi: 10.1016/j.apcatb.2003.09.010.
14 A. FUJISHIMA, X. ZHANG, and D. TRYK, "TiO2 photocatalysis and related surface phenomena," Surface Science Reports, vol. 63, no. 12, pp. 515–582, 2008, doi: 10.1016/j.surfrep.2008.10.001.
15 A. FUJISHIMA and K. HONDA, "Electrochemical Photolysis of Water at a Semiconductor Electrode," Nature, vol. 238, no. 5358, pp. 37–38, 1972, doi: 10.1038/238037a0.
16 K. M. Lee, C. W. Lai, K. S. Ngai, and J. C. Juan, "Recent developments of zinc oxide based photocatalyst in water treatment technology: A review," Water Research, vol. 88, pp. 428–448, 2016, doi: 10.1016/j.watres.2015.09.045.
17 H. Ali, E. Khan, and I. Ilahi, "Environmental Chemistry and Ecotoxicology of Hazardous Heavy Metals: Environmental Persistence, Toxicity, and Bioaccumulation," Journal of Chemistry, vol. 2019, pp. 1–14, 2019, doi: 10.1155/2019/6730305.
18 M. Balali-Mood, K. Naseri, Z. Tahergorabi, M. R. Khazdair, and M. Sadeghi, "Toxic Mechanisms of Five Heavy Metals: Mercury, Lead, Chromium, Cadmium, and Arsenic," Front. Pharmacol., vol. 12, 2021, doi: 10.3389/fphar.2021.643972.
19 R. Ding, Y. H. Cheong, A. Ahamed, and G. Lisak, "Heavy Metals Detection with Paper-Based Electrochemical Sensors," Anal. Chem., vol. 93, no. 4, pp. 1880–1888, 2021, doi: 10.1021/acs.analchem.0c04247.
20 A. J. Borrill, N. E. Reily, and J. V. Macpherson, "Addressing the practicalities of anodic stripping voltammetry for heavy metal detection: a tutorial review," Analyst, vol. 144, no. 23, pp. 6834–6849, 2019, doi: 10.1039/c9an01437c.
21 M. Pera-Titus, V. García-Molina, M. A. Baños, J. Giménez, and S. Esplugas, "Degradation of chlorophenols by means of advanced oxidation processes: a general review," Applied Catalysis B: Environmental, vol. 47, no. 4, pp. 219–256, 2004, doi: 10.1016/j.apcatb.2003.09.010.
22 A. FUJISHIMA, X. ZHANG, and D. TRYK, "TiO2 photocatalysis and related surface phenomena," Surface Science Reports, vol. 63, no. 12, pp. 515–582, 2008, doi: 10.1016/j.surfrep.2008.10.001.
23 H. Zhang, X. Lv, Y. Li, Y. Wang, and J. Li, "P25-Graphene Composite as a High Performance Photocatalyst," ACS Nano, vol. 4, no. 1, pp. 380–386, 2010, doi: 10.1021/nn901221k.
24 J. Guo et al., "Sonochemical synthesis of TiO2 nanoparticles on graphene for use as photocatalyst," Ultrasonics Sonochemistry, vol. 18, no. 5, pp. 1082–1090, 2011, doi: 10.1016/j.ultsonch.2011.03.021.
25 H. Safardoust-Hojaghan and M. Salavati-Niasari, "Degradation of methylene blue as a pollutant with N-doped graphene quantum dot/titanium dioxide nanocomposite," Journal of Cleaner Production, vol. 148, pp. 31–36, 2017, doi: 10.1016/j.jclepro.2017.01.169.
26 H. de Lasa, Photocatalytic Reaction Engineering. Springer Science & Business Media, 2006.

27 A. M. Alotaibi et al., “Chemical Vapor Deposition of Photocatalytically Active Pure Brookite TiO2 Thin Films,” Chem. Mater., vol. 30, no. 4, pp. 1353–1361, 2018, doi: 10.1021/acs.chemmater.7b04944.

28 J. P. Klesko et al., “Selective Atomic Layer Deposition Mechanism for Titanium Dioxide Films with (EtCp)Ti(NMe2)3: Ozone versus Water,” Chem. Mater., vol. 30, no. 3, pp. 970–981, 2018, doi: 10.1021/acs.chemmater.7b04790.

29 A. Abed and A. AL-Mathloom, “Titanium Dioxide Thin Film Prepared By Sol-Gel Technique,” JCEPS, vol. 9, no. 1, pp. 241–258, 2019, doi: 10.32792/utq.jceps.09.01.25.

30 N. Padoin, L. Andrade, J. Ângelo, A. Mendes, R. de F. P. M. Moreira, and C. Soares, “Intensification of photocatalytic pollutant abatement in microchannel reactor using TiO2and TiO2-graphene,” AIChE J., vol. 62, no. 8, pp. 2794–2802, 2016, doi: 10.1002/aic.15262.

31 M. M. de Villiers, D. P. Otto, S. J. Strydom, and Y. M. Lvov, “Introduction to nanocoatings produced by layer-by-layer (LbL) self-assembly,” Advanced Drug Delivery Reviews, vol. 63, no. 9, pp. 701–715, 2011, doi: 10.1016/j.addr.2011.05.011.

32 Y. Liu, A. Wang, and R. Claus, “Molecular Self-Assembly of TiO2/Polymer Nanocomposite Films,” J. Phys. Chem. B, vol. 101, no. 8, pp. 1385–1388, 1997, doi: 10.1021/jp962591e.

33 H.-B. Yao, L.-H. Wu, C.-H. Cui, H.-Y. Fang, and S.-H. Yu, “Direct fabrication of photoconductive patterns on LBL assembled graphene oxide/PDDA/titania hybrid films by photothermal and photocatalytic reduction,” J. Mater. Chem., vol. 20, no. 25, p. 5190, 2010, doi: 10.1039/c0jm00094a.

34 K. K. Manga, Y. Zhou, Y. Yan, and K. P. Loh, “Multilayer Hybrid Films Consisting of Alternating Graphene and Titania Nanosheets with Ultrafast Electron Transfer and Photoconversion Properties,” Adv. Funct. Mater., vol. 19, no. 22, pp. 3638–3643, 2009, doi: 10.1002/adfm.200900891.

35 D. L. Cunha, A. Kuznetsov, C. A. Achete, A. E. da H. Machado, and M. Marques, “Immobilized TiO2 on glass spheres applied to heterogeneous photocatalysis: photoactivity, leaching and regeneration process,” vol. 6, p. e4464, 2018, doi: 10.7717/peerj.4464.

36 Y. Wang et al., “Layer-by-layer self-assembly photocatalytic nanocoating on cotton fabrics as easily recycled photocatalyst for degrading gas and liquid pollutants,” Cellulose, vol. 24, no. 10, pp. 4569–4580, 2017, doi: 10.1007/s10570-017-1445-0.

37 P. Li, B. Zhang, and T. Cui, “TiO2 and shrink induced tunable nano self-assembled graphene composites for label free biosensors,” Sensors and Actuators B: Chemical, vol. 216, pp. 337–342, 2015, doi: 10.1016/j.snb.2015.03.111.

38 O. CARP, “Photoinduced reactivity of titanium dioxide,” Progress in Solid State Chemistry, vol. 32, no. 1–2, pp. 33–177, 2004, doi: 10.1016/j.progsolidstchem.2004.08.001.

39 D. C. Hurum, A. G. Agrios, K. A. Gray, T. Rajh, and M. C. Thurnauer, “Explaining the Enhanced Photocatalytic Activity of Degussa P25 Mixed-Phase TiO2 Using

EPR," J. Phys. Chem. B, vol. 107, no. 19, pp. 4545–4549, 2003, doi: 10.1021/jp0273934.

40 M. Boström, V. Deniz, G. V. Franks, and B. W. Ninham, "Extended DLVO theory: Electrostatic and non-electrostatic forces in oxide suspensions," Advances in Colloid and Interface Science, vol. 123–126, pp. 5–15, 2006, doi: 10.1016/j.cis.2006.05.001.

41 K. Suttiponparnit, J. Jiang, M. Sahu, S. Suvachittanont, T. Charinpanitkul, and P. Biswas, "Role of Surface Area, Primary Particle Size, and Crystal Phase on Titanium Dioxide Nanoparticle Dispersion Properties," Nanoscale Res Lett, vol. 6, no. 1, 2010, doi: 10.1007/s11671-010-9772-1.

42 K. Halasz, G. Grozdits, and L. Csóka, "Functional nanostructured coatings via layer-by-layer self-assembly," pp. 249–281, 2015, doi: 10.1016/b978-0-85709-211-3.00010-8.

43 Y. Gao, M. Hu, and B. Mi, "Membrane surface modification with TiO2–graphene oxide for enhanced photocatalytic performance," Journal of Membrane Science, vol. 455, pp. 349–356, 2014, doi: 10.1016/j.memsci.2014.01.011.

44 G. Williams, B. Seger, and P. V. Kamat, "TiO2-Graphene Nanocomposites. UV-Assisted Photocatalytic Reduction of Graphene Oxide," ACS Nano, vol. 2, no. 7, pp. 1487–1491, 2008, doi: 10.1021/nn800251f.

45 N. Raghavan, S. Thangavel, and G. Venugopal, "Enhanced photocatalytic degradation of methylene blue by reduced graphene-oxide/titanium dioxide/zinc oxide ternary nanocomposites," Materials Science in Semiconductor Processing, vol. 30, pp. 321–329, 2015, doi: 10.1016/j.mssp.2014.09.019.

46 G. Ren et al., "Recent Advances of Photocatalytic Application in Water Treatment: A Review," Nanomaterials, vol. 11, no. 7, p. 1804, 2021, doi: 10.3390/nano11071804.

47 A. J. Cowan, J. Tang, W. Leng, J. R. Durrant, and D. R. Klug, "Water Splitting by Nanocrystalline TiO2 in a Complete Photoelectrochemical Cell Exhibits Efficiencies Limited by Charge Recombination," J. Phys. Chem. C, vol. 114, no. 9, pp. 4208–4214, 2010, doi: 10.1021/jp909993w.

48 X. Kang, S. Liu, Z. Dai, Y. He, X. Song, and Z. Tan, "Titanium Dioxide: From Engineering to Applications," Catalysts, vol. 9, no. 2, p. 191, 2019, doi: 10.3390/catal9020191.

49 M. Lin, H. Chen, Z. Zhang, and X. Wang, "Engineering interface structures for heterojunction photocatalysts," Phys. Chem. Chem. Phys., vol. 25, no. 6, pp. 4388–4407, 2023, doi: 10.1039/d2cp05281d.

50 C. Qiu et al., "Construction of the Rutile/Anatase Micro-Heterophase Junction Photocatalyst from Anatase by Liquid Nitrogen Quenching Method," ACS Appl. Energy Mater., vol. 4, no. 9, pp. 10172–10186, 2021, doi: 10.1021/acsaem.1c02066.

51 L. Spanhel, H. Weller, and A. Henglein, "Photochemistry of semiconductor colloids. 22. Electron ejection from illuminated cadmium sulfide into attached titanium and zinc oxide particles," J. Am. Chem. Soc., vol. 109, no. 22, pp. 6632–6635, 1987, doi: 10.1021/ja00256a012.

52 A. Khlyustova, N. Sirotkin, T. Kusova, A. Kraev, V. Titov, and A. Agafonov, “Doped TiO2: the effect of doping elements on photocatalytic activity,” Mater. Adv., vol. 1, no. 5, pp. 1193–1201, 2020, doi: 10.1039/d0ma00171f.

53 A. Cerdán-Pasarán, T. López-Luke, X. Mathew, and N. R. Mathews, “Effect of cobalt doping on the device properties of Sb2S3-sensitized TiO2 solar cells,” Solar Energy, vol. 183, pp. 697–703, 2019, doi: 10.1016/j.solener.2019.03.077.

54 S. Yadav and G. Jaiswar, “Review on Undoped/Doped TiO2Nanomaterial; Synthesis and Photocatalytic and Antimicrobial Activity,” Journal of the Chinese Chemical Society, vol. 64, no. 1, pp. 103–116, 2017, doi: 10.1002/jccs.201600735.

55 C. Siriwong, N. Wetchakun, B. Inceesungvorn, D. Channei, T. Samerjai, and S. Phanichphant, “Doped-metal oxide nanoparticles for use as photocatalysts,” Progress in Crystal Growth and Characterization of Materials, vol. 58, no. 2–3, pp. 145–163, 2012, doi: 10.1016/j.pcrysgrow.2012.02.004.

56 Y.-Y. Sun and S. Zhang, “Kinetics stabilized doping: computational optimization of carbon-doped anatase TiO2 for visible-light driven water splitting,” Phys. Chem. Chem. Phys., vol. 18, no. 4, pp. 2776–2783, 2016, doi: 10.1039/c5cp07109g.

57 R. Tang, Q. Jiang, and Y. Liu, “Preparation and Study on Photocatalytic Activity of N-doped TiO 2 Decorated N-doped graphene,” Procedia Engineering, vol. 205, pp. 573–580, 2017, doi: 10.1016/j.proeng.2017.10.423.

58 B. A. Bhanvase, T. P. Shende, and S. H. Sonawane, “A review on graphene–TiO2 and doped graphene–TiO2 nanocomposite photocatalyst for water and wastewater treatment,” Environmental Technology Reviews, vol. 6, no. 1, pp. 1–14, 2017, doi: 10.1080/21622515.2016.1264489.

59 Y. S. Sohn, Y. R. Smith, M. Misra, and V. (Ravi) Subramanian, “Electrochemically assisted photocatalytic degradation of methyl orange using anodized titanium dioxide nanotubes,” Applied Catalysis B: Environmental, vol. 84, no. 3–4, pp. 372–378, 2008, doi: 10.1016/j.apcatb.2008.04.021.

60 S. Ye, Y. Chen, X. Yao, and J. Zhang, “Simultaneous removal of organic pollutants and heavy metals in wastewater by photoelectrocatalysis: A review,” Chemosphere, vol. 273, p. 128503, 2021, doi: 10.1016/j.chemosphere.2020.128503.

61 D. Wang et al., “Advanced municipal wastewater treatment and simultaneous energy/resource recovery via photo(electro)catalysis,” Chinese Chemical Letters, vol. 34, no. 5, p. 107861, 2023, doi: 10.1016/j.cclet.2022.107861.

62 C. Liu, Y. Ding, W. Wu, and Y. Teng, “A simple and effective strategy to fast remove chromium (VI) and organic pollutant in photoelectrocatalytic process at low voltage,” Chemical Engineering Journal, vol. 306, pp. 22–30, 2016, doi: 10.1016/j.cej.2016.07.043.

63 T. H. Jeon, M. S. Koo, H. Kim, and W. Choi, “Dual-Functional Photocatalytic and Photoelectrocatalytic Systems for Energy- and Resource-Recovering Water Treatment,” ACS Catal., vol. 8, no. 12, pp. 11542–11563, 2018, doi: 10.1021/acscatal.8b03521.

64 X. Zhao, L. Guo, and J. Qu, “Photoelectrocatalytic oxidation of Cu-EDTA complex and electrodeposition recovery of Cu in a continuous tubular photoelectrochemical

reactor," Chemical Engineering Journal, vol. 239, pp. 53–59, 2014, doi: 10.1016/j.cej.2013.10.088.

65 M. M. Momeni, "Study of synergistic effect among photo-, electro-, and sonoprocesses in photocatalyst degradation of phenol on tungsten-loaded titania nanotubes composite electrode," Appl. Phys. A, vol. 119, no. 4, pp. 1413–1422, 2015, doi: 10.1007/s00339-015-9114-3.

66 X. Zhang et al., "Recent advances in photoelectrocatalytic advanced oxidation processes: From mechanism understanding to catalyst design and actual applications," Chemical Engineering Journal, vol. 455, p. 140801, 2023, doi: 10.1016/j.cej.2022.140801.

67 J. Yang, J. Dai, C. Chen, and J. Zhao, "Effects of hydroxyl radicals and oxygen species on the 4-chlorophenol degradation by photoelectrocatalytic reactions with TiO2-film electrodes," Journal of Photochemistry and Photobiology A: Chemistry, vol. 208, no. 1, pp. 66–77, 2009, doi: 10.1016/j.jphotochem.2009.08.007.

68 Q. Dang et al., "Recent progress of photoelectrocatalysis systems for wastewater treatment," Journal of Water Process Engineering, vol. 53, p. 103609, 2023, doi: 10.1016/j.jwpe.2023.103609.

69 A. Hayali, R. J. Reeves, and M. M. Alkaisi, "Wavelength Selective Solar Cells Using Triple Cation Perovskite," Nanomaterials, vol. 12, no. 19, p. 3299, 2022, doi: 10.3390/nano12193299.

70 X. Zhang, P. Zhang, W. Zhang, J. Chen, and F. Hu, "Preparation of UV Curable Optical Adhesive NOA81 Bionic Lotus Leaf Structure Films by Nanoimprint Technique and the Applications on Silicon Solar Cells," Coatings, vol. 13, no. 5, p. 867, 2023, doi: 10.3390/coatings13050867.

71 J. Zhang, Y. Li, T. Xie, Y. Cui, R. Mao, and X. Zhao, "Enhanced photoelectrocatalytic oxidation of hypophosphite and simultaneous recovery of metallic nickel via carbon aerogel cathode," Journal of Hazardous Materials, vol. 448, p. 130601, 2023, doi: 10.1016/j.jhazmat.2022.130601.

72 E. Tüzün and G. Atun, "Individual and Simultaneous Determination of Heavy Metal Ions Using Carbon Paste Electrode Modified with Titania Nanoparticles," Electrocatalysis, 2023, doi: 10.1007/s12678-023-00824-z.

73 S. Hanasoge, P. J. Hesketh, and A. Alexeev, "Microfluidic pumping using artificial magnetic cilia," Microsyst Nanoeng, vol. 4, no. 1, 2018, doi: 10.1038/s41378-018-0010-9.

74 S. Zhang, Z. Cui, Y. Wang, and J. M. J. den Toonder, "Metachronal actuation of microscopic magnetic artificial cilia generates strong microfluidic pumping," Lab Chip, vol. 20, no. 19, pp. 3569–3581, 2020, doi: 10.1039/d0lc00610f.

75 M. S, N. Karanth P, and S. M. Kulkarni, "Performance analysis of valveless micropump with disposable chamber actuated through Amplified Piezo Actuator (APA) for biomedical application," Mechatronics, vol. 67, p. 102347, 2020, doi: 10.1016/j.mechatronics.2020.102347.

76 R. R. Gidde, P. M. Pawar, and V. P. Dhamgaye, "Fully coupled modeling and design of a piezoelectric actuation based valveless micropump for drug delivery

application," Microsyst Technol, vol. 26, no. 2, pp. 633–645, 2020, doi: 10.1007/s00542-019-04535-8.

77 S. Mi, H. Pu, S. Xia, and W. Sun, "A Minimized Valveless Electromagnetic Micropump for Microfluidic Actuation on Organ Chips," Sensors and Actuators A: Physical, vol. 301, p. 111704, 2020, doi: 10.1016/j.sna.2019.111704.

78 A.-B. Wang and M.-C. Hsieh, "Unveiling the missing transport mechanism inside the valveless micropump," Lab Chip, vol. 12, no. 17, p. 3024, 2012, doi: 10.1039/c2lc40210f.

79 E. Stemme and G. Stemme, "A valveless diffuser/nozzle-based fluid pump," Sensors and Actuators A: Physical, vol. 39, no. 2, pp. 159–167, 1993, doi: 10.1016/0924-4247(93)80213-z.

80 K. Mohammadzadeh, E. M. Kolahdouz, E. Shirani, and M. B. Shafii, "Numerical study on the performance of Tesla type microvalve in a valveless micropump in the range of low frequencies," J Micro-Bio Robot, vol. 8, no. 3–4, pp. 145–159, 2013, doi: 10.1007/s12213-013-0069-1.

81 X. N. Jiang, Z. Y. Zhou, X. Y. Huang, Y. Li, Y. Yang, and C. Y. Liu, "Micronozzle/diffuser flow and its application in micro valveless pumps," Sensors and Actuators A: Physical, vol. 70, no. 1–2, pp. 81–87, 1998, doi: 10.1016/s0924-4247(98)00115-0.

82 C.-H. Cheng, "Performance Evaluation of the Valveless Micropump with Piezoelectric Actuator," pp. 101–115, 2014, doi: 10.1007/978-94-017-8832-8_8.

83 B. Parsi, L. Zhang, and V. Masek, "Vibration Analysis Of A Double Circular Pzt Actuator For A Valveless Micropump," 2018, doi: 10.25071/10315/35215.

84 A. Chandrasekaran and M. Packirisamy, "Geometrical tuning of microdiffuser/nozzle for valveless micropumps," J. Micromech. Microeng., vol. 21, no. 4, p. 045035, 2011, doi: 10.1088/0960-1317/21/4/045035.

85 K.-S. Yang, T.-F. Chao, I. Y. Chen, C.-C. Wang, and J.-C. Shyu, "A Comparative Study of Nozzle/Diffuser Micropumps with Novel Valves," Molecules, vol. 17, no. 2, pp. 2178–2187, 2012, doi: 10.3390/molecules17022178.

86 A. Purwidyantri and B. A. Prabowo, "Tesla Valve Microfluidics: The Rise of Forgotten Technology," doi: 10.20944/preprints202304.0104.v1.

87 A. R. Gamboa, C. J. Morris, and F. K. Forster, "Optimization of the Fixed-Geometry Valve for Increased Micropump Performance," 2003, doi: 10.1115/imece2003-55036.

88 A. Rogers and Y. Wang, "Does Tesla valve work for microscale active swimmers? – a computational study," doi: 10.1101/2022.03.31.486569.

89 S. Derakhshan, B. Beigzadeh, M. Rashidi, and H. Pourrahmani, "Performance Improvement and Two-Phase Flow Study of a Piezoelectric Micropump with Tesla Nozzle-Diffuser Microvalves," JAFM, vol. 12, no. 2, pp. 341–350, 2019, doi: 10.29252/jafm.12.02.27886.

90 C. H. Cheng and Y. P. Tseng, "Design and Fabrication of the Piezoelectrically Actuated Micropump with Implanted Check Valves," AMM, vol. 284–287, pp. 2032–2036, 2013, doi: 10.4028/www.scientific.net/amm.284-287.2032.

91 Q. Yan, Y. Yin, W. Sun, and J. Fu, “Advances in Valveless Piezoelectric Pumps,” Applied Sciences, vol. 11, no. 15, p. 7061, 2021, doi: 10.3390/app11157061.
92 Q. Cui, C. Liu, and X. F. Zha, “Simulation and optimization of a piezoelectric micropump for medical applications,” Int J Adv Manuf Technol, vol. 36, no. 5–6, pp. 516–524, 2008, doi: 10.1007/s00170-006-0867-x.
93 O. Sigmund and K. Maute, “Topology optimization approaches,” Struct Multidisc Optim, vol. 48, no. 6, pp. 1031–1055, 2013, doi: 10.1007/s00158-013-0978-6.
94 J. Alexandersen and C. S. Andreasen, “A Review of Topology Optimisation for Fluid-Based Problems,” Fluids, vol. 5, no. 1, p. 29, 2020, doi: 10.3390/fluids5010029.
95 S. Lin, L. Zhao, J. K. Guest, T. P. Weihs, and Z. Liu, “Topology Optimization of Fixed-Geometry Fluid Diodes,” vol. 137, no. 8, 2015, doi: 10.1115/1.4030297.
96 Y. Sato, K. Yaji, K. Izui, T. Yamada, and S. Nishiwaki, “Topology optimization of a no-moving-part valve incorporating Pareto frontier exploration,” Struct Multidisc Optim, vol. 56, no. 4, pp. 839–851, 2017, doi: 10.1007/s00158-017-1690-8.
97 Y. Deng, Z. Liu, P. Zhang, Y. Wu, and J. G. Korvink, “Optimization of no-moving part fluidic resistance microvalves with low reynolds number,” 2010, doi: 10.1109/memsys.2010.5442565.
98 R. R. Gidde, P. M. Pawar, B. P. Ronge, and V. P. Dhamgaye, “Design optimization of an electromagnetic actuation based valveless micropump for drug delivery application,” Microsyst Technol, vol. 25, no. 2, pp. 509–519, 2019, doi: 10.1007/s00542-018-3987-y.
99 M. Kohl, D. Dittmann, E. Quandt, and B. Winzek, “Thin film shape memory microvalves with adjustable operation temperature,” Sensors and Actuators A: Physical, vol. 83, no. 1–3, pp. 214–219, 2000, doi: 10.1016/s0924-4247(99)00386-6.
100 B. K. Paul and T. Terhaar, “Comparison of two passive microvalve designs for microlamination architectures,” J. Micromech. Microeng., vol. 10, no. 1, pp. 15–20, 2000, doi: 10.1088/0960-1317/10/1/303.
101 L.-J. Yang, T.-Y. Lin, and Y.-C. Ou, “A Thermopneumatic Valveless Micropump With PDMS-Based Nozzle/Diffuser Structure for Microfluidic System,” 2008, doi: 10.1115/mnht2008-52352.
102 A. Olsson, G. Stemme, and E. Stemme, “Simulation studies of diffuser and nozzle elements for valve-less micropumps,” doi: 10.1109/sensor.1997.635363.
103 M. P. Bendsøe, Topology Optimization. Berlin, Heidelberg: Springer Science & Business Media, 2004.
104 X. He, X. Zhang, S. Yang, J. Zhu, and J. Yan, “Flow characteristic of a valveless piezoelectric micropump applying Coanda effect,” 2014, doi: 10.1049/cp.2014.1157.
105 X. He, J. Zhu, X. Zhang, L. Xu, and S. Yang, “The analysis of internal transient flow and the performance of valveless piezoelectric micropumps with planar diffuser/nozzles elements,” Microsyst Technol, vol. 23, no. 1, pp. 23–37, 2017, doi: 10.1007/s00542-015-2695-0. Poole Jr, C. P. & Owens, F. J. *Introduction to nanotechnology*. (John Wiley & Sons, 2003).

106 E. John., Nature’s building blocks. Oxford: Oxford University Press, USA, 2011.

107 H. Ali, E. Khan, and I. Ilahi, “Environmental Chemistry and Ecotoxicology of Hazardous Heavy Metals: Environmental Persistence, Toxicity, and Bioaccumulation,” Journal of Chemistry, vol. 2019, pp. 1–14, 2019, doi: 10.1155/2019/6730305.

108 A. Alengebawy, S. T. Abdelkhalek, S. R. Qureshi, and M.-Q. Wang, “Heavy Metals and Pesticides Toxicity in Agricultural Soil and Plants: Ecological Risks and Human Health Implications,” Toxics, vol. 9, no. 3, p. 42, 2021, doi: 10.3390/toxics9030042.

109 J. Briffa, E. Sinagra, and R. Blundell, “Heavy metal pollution in the environment and their toxicological effects on humans,” Heliyon, vol. 6, no. 9, p. e04691, 2020, doi: 10.1016/j.heliyon.2020.e04691.

110 M. Jaishankar, T. Tseten, N. Anbalagan, B. B. Mathew, and K. N. Beeregowda, “Toxicity, mechanism and health effects of some heavy metals,” vol. 7, no. 2, pp. 60–72, 2014, doi: 10.2478/intox-2014-0009.

111 M. Balali-Mood, K. Naseri, Z. Tahergorabi, M. R. Khazdair, and M. Sadeghi, “Toxic Mechanisms of Five Heavy Metals: Mercury, Lead, Chromium, Cadmium, and Arsenic,” Front. Pharmacol., vol. 12, 2021, doi: 10.3389/fphar.2021.643972.

112 S. Mitra et al., “Impact of heavy metals on the environment and human health: Novel therapeutic insights to counter the toxicity,” Journal of King Saud University - Science, vol. 34, no. 3, p. 101865, 2022, doi: 10.1016/j.jksus.2022.101865.

113 W. H. Organization, Global Health Risks Mortality And Burden Of Disease Attributable To Selected Major Risks. World Health Organization, 2010.

114 J. Huff, R. M. Lunn, M. P. Waalkes, L. Tomatis, and P. F. Infante, “Cadmium-induced Cancers in Animals and in Humans,” International Journal of Occupational and Environmental Health, vol. 13, no. 2, pp. 202–212, 2007, doi: 10.1179/oeh.2007.13.2.202.

115 I. W. Group, IARC Handbooks of Cancer Prevention, Volume 1. 1997.

116 “National Primary Drinking Water Regulations | US EPA,” US EPA. Online . Available: https://www.epa.gov/ground-water-and-drinking-water/national-primary-drinking-water-regulations. Accessed: 13-May-2023 .

117 J. B. Willis, “Determination of Lead and Other Heavy Metals in Urine by Atomic Absorption Spectroscopy.,” Anal. Chem., vol. 34, no. 6, pp. 614–617, 1962, doi: 10.1021/ac60186a008.

118 D. G. Bua, G. Annuario, A. Albergamo, N. Cicero, and G. Dugo, “Heavy metals in aromatic spices by inductively coupled plasma-mass spectrometry,” Food Additives & Contaminants: Part B, vol. 9, no. 3, pp. 210–216, 2016, doi: 10.1080/19393210.2016.1175516.

119 L. A. Hutton, G. D. O’Neil, T. L. Read, Z. J. Ayres, M. E. Newton, and J. V. Macpherson, “Electrochemical X-ray Fluorescence Spectroscopy for Trace Heavy Metal Analysis: Enhancing X-ray Fluorescence Detection Capabilities by Four Orders of Magnitude,” Anal. Chem., vol. 86, no. 9, pp. 4566–4572, 2014, doi: 10.1021/ac500608d.

120 A. J. Borrill, N. E. Reily, and J. V. Macpherson, “Addressing the practicalities of anodic stripping voltammetry for heavy metal detection: a tutorial review,” Analyst, vol. 144, no. 23, pp. 6834–6849, 2019, doi: 10.1039/c9an01437c.

121 S. Li et al., “Electrochemical microfluidics techniques for heavy metal ion detection,” Analyst, vol. 143, no. 18, pp. 4230–4246, 2018, doi: 10.1039/c8an01067f.

122 J. G. Walters, S. Ahmed, I. M. Terrero Rodríguez, and G. D. O’Neil, “Trace Analysis of Heavy Metals (Cd, Pb, Hg) Using Native and Modified 3D Printed Graphene/Poly(Lactic Acid) Composite Electrodes,” Electroanalysis, vol. 32, no. 4, pp. 859–866, 2020, doi: 10.1002/elan.201900658.

123 G. Aragay and A. Merkoçi, “Nanomaterials application in electrochemical detection of heavy metals,” Electrochimica Acta, vol. 84, pp. 49–61, 2012, doi: 10.1016/j.electacta.2012.04.044.

124 Y. Xia, J. Li, G. Zhu, and Y. Yi, “Innovative strategy based on novel Ti3C2Tx MXenes nanoribbons/carbon nanotubes hybrids for anodic stripping voltammetry sensing of mercury ion,” Sensors and Actuators B: Chemical, vol. 355, p. 131247, 2022, doi: 10.1016/j.snb.2021.131247.

125 E. A. McGaw and G. M. Swain, “A comparison of boron-doped diamond thin-film and Hg-coated glassy carbon electrodes for anodic stripping voltammetric determination of heavy metal ions in aqueous media,” Analytica Chimica Acta, vol. 575, no. 2, pp. 180–189, 2006, doi: 10.1016/j.aca.2006.05.094.

126 W. Jung, A. Jang, P. L. Bishop, and C. H. Ahn, “A polymer lab chip sensor with microfabricated planar silver electrode for continuous and on-site heavy metal measurement,” Sensors and Actuators B: Chemical, vol. 155, no. 1, pp. 145–153, 2011, doi: 10.1016/j.snb.2010.11.039.

127 A. Giacomino et al., “Anodic stripping voltammetry with gold electrodes as an alternative method for the routine determination of mercury in fish. Comparison with spectroscopic approaches,” Food Chemistry, vol. 221, pp. 737–745, 2017, doi: 10.1016/j.foodchem.2016.11.111.

128 W. E. Van der Linden and J. W. Dieker, “Glassy carbon as electrode material in electro- analytical chemistry,” Analytica Chimica Acta, vol. 119, no. 1, pp. 1–24, 1980, doi: 10.1016/s0003-2670(00)00025-8.

129 X. Dai, G. G. Wildgoose, C. Salter, A. Crossley, and R. G. Compton, “Electroanalysis Using Macro-, Micro-, and Nanochemical Architectures on Electrode Surfaces. Bulk Surface Modification of Glassy Carbon Microspheres with Gold Nanoparticles and Their Electrical Wiring Using Carbon Nanotubes,” Anal. Chem., vol. 78, no. 17, pp. 6102–6108, 2006, doi: 10.1021/ac060582o.

130 A. Kulpa-Koterwa, T. Ossowski, and P. Niedziałkowski, “Functionalized Fe3O4 Nanoparticles as Glassy Carbon Electrode Modifiers for Heavy Metal Ions Detection—A Mini Review,” Materials, vol. 14, no. 24, p. 7725, 2021, doi: 10.3390/ma14247725.

131 R. P. Deo and J. Wang, “Electrochemical detection of carbohydrates at carbon-nanotube modified glassy-carbon electrodes,” Electrochemistry Communications, vol. 6, no. 3, pp. 284–287, 2004, doi: 10.1016/j.elecom.2004.01.003.

132 Y. Liu, X. Dong, and P. Chen, “ChemInform Abstract: Biological and Chemical Sensors Based on Graphene Materials,” ChemInform, vol. 43, no. 24, p. no-no, 2012, doi: 10.1002/chin.201224276.

133 S. C. Vasconcelos et al., “An improved drop casting electrochemical strategy for furosemide quantification in natural waters exploiting chemically reduced graphene oxide on glassy carbon electrodes,” Anal Bioanal Chem, vol. 412, no. 26, pp. 7123–7130, 2020, doi: 10.1007/s00216-020-02845-9.

134 L. Chen, Y. Tang, K. Wang, C. Liu, and S. Luo, “Direct electrodeposition of reduced graphene oxide on glassy carbon electrode and its electrochemical application,” Electrochemistry Communications, vol. 13, no. 2, pp. 133–137, 2011, doi: 10.1016/j.elecom.2010.11.033.

135 R. Shen, W. Zhang, Y. Yuan, G. He, and H. Chen, “Electrochemical detection of bisphenol A at graphene/melamine nanoparticle-modified glassy carbon electrode,” J Appl Electrochem, vol. 45, no. 4, pp. 343–352, 2015, doi: 10.1007/s10800-015-0792-5.

136 P. Jothimuthu, R. A. Wilson, J. Herren, E. N. Haynes, W. R. Heineman, and I. Papautsky, “Lab-on-a-chip sensor for detection of highly electronegative heavy metals by anodic stripping voltammetry,” Biomed Microdevices, vol. 13, no. 4, pp. 695–703, 2011, doi: 10.1007/s10544-011-9539-1.

137 Z. Zou et al., “Environmentally friendly disposable sensors with microfabricated on-chip planar bismuth electrode for in situ heavy metal ions measurement,” Sensors and Actuators B: Chemical, vol. 134, no. 1, pp. 18–24, 2008, doi: 10.1016/j.snb.2008.04.005.

138 Y. Hong et al., “3D Printed Microfluidic Device with Microporous Mn2O3-Modified Screen Printed Electrode for Real-Time Determination of Heavy Metal Ions,” ACS Appl. Mater. Interfaces, vol. 8, no. 48, pp. 32940–32947, 2016, doi: 10.1021/acsami.6b10464.

139 L.-L. Shen, G.-R. Zhang, W. Li, M. Biesalski, and B. J. M. Etzold, “Modifier-Free Microfluidic Electrochemical Sensor for Heavy-Metal Detection,” ACS Omega, vol. 2, no. 8, pp. 4593–4603, 2017, doi: 10.1021/acsomega.7b00611.

140 A. Lace and J. Cleary, “A Review of Microfluidic Detection Strategies for Heavy Metals in Water,” Chemosensors, vol. 9, no. 4, p. 60, 2021, doi: 10.3390/chemosensors9040060.

141 P. Zhou, T. Zhang, T. W. Simon, and T. Cui, “Simulation and Experiments on a Valveless Micropump With Fluidic Diodes Based on Topology Optimization,” J. Microelectromech. Syst., vol. 31, no. 2, pp. 292–297, 2022, doi: 10.1109/jmems.2021.3133469.

142 P. Zhou and T. Cui, “Enhanced photocatalytic efficiency by layer-by- layer self-assembly of graphene and titanium dioxide on shrink thermoplastic film,” Microsyst Technol, vol. 26, no. 12, pp. 3793–3798, 2020, doi: 10.1007/s00542-020-04865-y.

143 P. Zhou, T. Zhang, T. Simon, and T. Cui, “A Fluidic Diode and Its Application to a Valveless Micropump,” 2021, doi: 10.1109/mems51782.2021.9375273.

144 V. Rehacek, I. Hotovy, M. Vojs, T. Kups, and L. Spiess, “Nafion-coated bismuth film electrodes on pyrolyzed photoresist/alumina supports for analysis of trace heavy metals,” Electrochimica Acta, vol. 63, pp. 192–196, 2012, doi: 10.1016/j.electacta.2011.12.075.

145 X. Xuan and J. Y. Park, “A miniaturized and flexible cadmium and lead ion detection sensor based on micro-patterned reduced graphene oxide/carbon nanotube/bismuth composite electrodes,” Sensors and Actuators B: Chemical, vol. 255, pp. 1220–1227, 2018, doi: 10.1016/j.snb.2017.08.046.

146 K. C. Armstrong, C. E. Tatum, R. N. Dansby-Sparks, J. Q. Chambers, and Z.-L. Xue, “Individual and simultaneous determination of lead, cadmium, and zinc by anodic stripping voltammetry at a bismuth bulk electrode,” Talanta, vol. 82, no. 2, pp. 675–680, 2010, doi: 10.1016/j.talanta.2010.05.031.

147 A. A. Kava, C. Beardsley, J. Hofstetter, and C. S. Henry, “Disposable glassy carbon stencil printed electrodes for trace detection of cadmium and lead,” Analytica Chimica Acta, vol. 1103, pp. 58–66, 2020, doi: 10.1016/j.aca.2019.12.047.

148 T. Z. Redhwan, Y. Ali, M. M. R. Howlader, and Y. M. Haddara, “Electrochemical Sensing of Lead in Drinking Water Using Copper Foil Bonded with Polymer,” Sensors, vol. 23, no. 3, p. 1424, 2023, doi: 10.3390/s23031424.

149 D. Quang Khieu, N. Thanh Dinh, T. Xuan Mau, and H. D. Mai, “Synthesis and Application of Novel Hybrid Nanomaterials in Catalysis, Adsorption, and Electrochemistry,” Advances in Materials Science and Engineering, vol. 2019, pp. 1–1, 2019, doi: 10.1155/2019/6182374.

150 A. Manivannan, R. Kawasaki, D. A. Tryk, and A. Fujishima, “Interaction of Pb and Cd during anodic stripping voltammetric analysis at boron-doped diamond electrodes,” Electrochimica Acta, vol. 49, no. 20, pp. 3313–3318, 2004, doi: 10.1016/j.electacta.2004.03.004.

151 J. M. Gutiérrez, L. Moreno-Barón, F. Céspedes, R. Muñoz, and M. del Valle, “Resolution of Heavy Metal Mixtures from Highly Overlapped ASV Voltammograms Employing a Wavelet Neural Network,” Electroanalysis, vol. 21, no. 3–5, pp. 445–451, 2009, doi: 10.1002/elan.200804419.

152 J. Kudr et al., “Simultaneous Automatic Electrochemical Detection of Zinc, Cadmium, Copper and Lead Ions in Environmental Samples Using a Thin-Film Mercury Electrode and an Artificial Neural Network,” Sensors, vol. 15, no. 1, pp. 592–610, 2014, doi: 10.3390/s150100592.

Appendix A: List of Publications

- **P. Zhou**, Y. Xu, T. Simon, and T. Cui, "Pyrolytic Glassy Carbon and Graphene Composite Electrode-Based Valveless Micropump Microfluidic Sensor for Heavy Metal Detection," (Under review).
- **P. Zhou**, Y. Xu, and T. Cui, "A Novel Photoelectrocatalytic Water Purification Configuration for Simultaneous Removal of Organics and Heavy Metal Ions in Polluted Water," (Under review).
- **P. Zhou**, T. Zhang, Y. Xu, T. Simon, and T. Cui, "Microfluidic Electrochemical Sensor for Heavy Metal Detection Using Pyrolytic Carbon Electrodes and Valveless Micropump," International Conference on Manipulation, Automation and Robotics at Small Scales (MARSS). IEEE, 2022, doi: 10.1109/marss55884.2022.9870496.
- **P. Zhou**, T. Zhang, T. W. Simon, and T. Cui, "Simulation and Experiments on a Valveless Micropump with Fluidic Diodes Based on Topology Optimization," *Journal of Microelectromechanical Systems*, vol. 31, no. 2, pp. 292–297, 2022, doi: 10.1109/jmems.2021.3133469.
- **P. Zhou**, T. Zhang, T. Simon, and T. Cui, "A Fluidic Diode and Its Application to a Valveless Micropump," 2021 IEEE 34th International Conference on Micro Electro Mechanical Systems (MEMS), 2021, doi: 10.1109/mems51782.2021.9375273.
- **P. Zhou** and T. Cui, "Enhanced photocatalytic efficiency by layer-by- layer self-assembly of graphene and titanium dioxide on shrink thermoplastic film," *Microsystem Technologies*, vol. 26, no. 12, pp. 3793–3798, 2020, doi: 10.1007/s00542-020-04865-y.

- J. Kim, T. Zhang, **P. Zhou**, Q. Guan, Y. Xu, J. Sartori, L. Linderman, V. Mandic, & T. Cui "Polymer tunneling vibration sensors using hot embossing technique," *Sensors and Actuators A: Physical*, vol. 344, p. 113705, 2022, doi: 10.1016/j.sna.2022.113705.
- T. Zhang, **P. Zhou**, T. Simon, and T. Cui, "Vibrating a sessile droplet to enhance mass transfer for high-performance electrochemical sensors," *Sensors and Actuators B: Chemical*, vol. 362, p. 131788, 2022, doi: 10.1016/j.snb.2022.131788.
- T. Zhang, **P. Zhou**, T. Simon, and T. Cui, "Vibrating an air bubble to enhance mass transfer for an ultra-sensitive electrochemical sensor," *Sensors and Actuators B: Chemical*, vol. 354, p. 131218, 2022, doi: 10.1016/j.snb.2021.131218.
- T. Zhang, **P. Zhou**, T. Simon, and T. Cui, "A Circular Vibrating Electrode with Enhanced Mass Transfer for High-Performance Electrochemical Sensors," 2021 IEEE 34th International Conference on Micro Electro Mechanical Systems (MEMS), 2021, doi: 10.1109/mems51782.2021.9375360.
- W. He, R. Liu, **P. Zhou**, Q. Liu, and T. Cui, "Flexible micro-sensors with self-assembled graphene on a polyolefin substrate for dopamine detection," *Biosensors and Bioelectronics*, vol. 167, p. 112473, 2020, doi: 10.1016/j.bios.2020.112473.
- W. He, R. Liu, **P. Zhou**, Q. Liu, and T. Cui. "Flexible polyolefin-based dopamine sensor with high selectivity," 24th International Conference on Miniaturized Systems for Chemistry and Life Sciences, MicroTAS 2020. Chemical and Biological Microsystems Society, 2020.
- T. Zhang, **P. Zhou,** T. Simon, and T. Cui, "Effect of membrane electrode vibration on mass transfer for electrochemical micro sensors," 24th International Conference on

Miniaturized Systems for Chemistry and Life Sciences, MicroTAS 2020. Chemical and Biological Microsystems Society, 2020.